COST-EFFECTIVE PROCESSING OF IMMISCIBLE POLYMER BLENDS INTO VALUE-ADDED FIBER-BASED PRODUCTS

A Dissertation
Presented to
The Academic Faculty

by

Jing Shi

In Partial Fulfillment
of the Requirements for the Degree
Doctor of Philosophy in the
School of Materials Science and Engineering

Georgia Institute of Technology
August 2019

COST-EFFECTIVE PROCESSING OF IMMISCIBLE POLYMER BLENDS INTO VALUE-ADDED FIBER-BASED PRODUCTS

Approved by:

Dr. Donggang Yao, Advisor
School of Materials Science and Engineering
Georgia Institute of Technology

Dr. Yulin Deng
School of Chemical and Biomolecular Engineering
Georgia Institute of Technology

Dr. Karl Jacob
School of Materials Science and Engineering
Georgia Institute of Technology

Dr. Meisha Shofner
School of Materials Science and Engineering
Georgia Institute of Technology

Dr. Youjiang Wang
School of Materials Science and Engineering
Georgia Institute of Technology

Date Approved: 07/02/2019

ACKNOWLEDGEMENTS

First of all, I would like to express my great appreciation to my PhD advisor, Prof. Donggang Yao. Without his advice and encouragement, I would not have this valuable opportunity to pursue a PhD study. Dr. Yao is very wise, intelligent and hard-working, setting a good example of life-learning. I appreciate him for spending lots of time teaching me knowledge and life philosophy. I am also very grateful for his patience and tolerance, without which I would not be able to complete this PhD study.

I would also like to thank Prof. Yulin Deng, Prof. Karl Jacob, Prof. Meisha Shofner, and Prof. Youjiang Wang for their guidance in my research. Their suggestions are valuable for my thesis work. I am very grateful for their time and for their willingness to serve on the committee.

I want to express sincere thanks to my labmates, including Dr. Xudong Fang, Dr. Yifeng Hong, Dr. Tom Wyatt, Adam Maffe and Junhe Chen for their help. I also want to thank my friends who supported me through the hardship. Among them, Dr. Emily Fitzharris, Dr. Matthew Orr and Cameron Irvin provided great help in my research and I am grateful to them.

At last, my special thanks should be given to my family members, especially my mother, my father, my younger sister and my great-grandmother. I am grateful for having their selfless love and company.

TABLE OF CONTENTS

LIST OF TABLES

LIST OF FIGURES

LIST OF SYMBOLS AND ABBREVIATIONS

ΔG_M	Gibbs' free energy of mixing
T	Absolute temperature
ŋ*	Viscosity of the mixture
$ŋ_d$	Viscosity of dispersed phase
$ŋ_m$	Viscosity of the matrix
Γ	Interfacial tension
$\dot{\gamma}$	Shear rate
P	Droplet/matrix viscosity ratio
Ca	Capillary number
η_0	Zero-shear viscosity
R	Dispersed phase size
τ	Stress
q	Interface tensor
T	Cauchy stress tensor
V	Volume in deformed state
I	Identity tensor
Ψ	Total interface
n	Unit normal vector to a local interface
Q	Interfacial area per unit volume
L	Velocity gradient
v	Velocity
x	Position vector in the deformed configuration

$\mathbf{x}'$	Position vector in undeformed configuration
ŋ	Viscosity
$\mathbf{A}$	Area tensor
d$\mathbf{a}'$	Infinitesimally small area vector
d$\mathbf{a}$	Deformed area vector
$\mathscr{A}$	A fourth-order tensor
J	Determinant of **F**
$\mathbf{C}$	Right Cauchy-Green strain tensor
$\mathbf{B}$	Left Cauchy-Green strain tensor/ Finger strain tensor
$\mathbf{V}_0$	Volume before deformation
Ψ_0	Initial interface
$\mathbf{M}$	Characteristic tensor of an ellipsoid
$\dot{W}$	Stress power density
W	Mechanical energy accumulated per unit volume
U	Interfacial energy per unit volume in undeformed state
ϕ	Interfacial orientation degree
$\dot{\varepsilon}_0$	Constant stretch rate
ξ	Characteristic relaxation time
$\hat{l}$	Unit length
$\tilde{t}$	Reduced time
γ	Shear strain
g	Surface area of ellipsoid
$\mathbf{B}_e$	Memorized strain
$\mathbf{B}_d$	Dissipated strain

k_i	Eigenvalues
$\mathbf{b}^i$	Eigenvectors

SUMMARY

The current practice for recycling of mixed plastics relies on complex and time-consuming procedures for materials separation or on the use of expensive compatibilizers for improving mechanical properties. A simple method for direct reuse of waste plastics without the pre-separation procedure or the compatibilizer will be beneficial for efficient and cost-effective recycling. This emerging need provides a motivation to study how to process immiscible polymer blends into value-added fiber-based products without using compatibilizers, which, on the other hand, are also helpful for the development of new polymer blend products.

Because of the existence of an implicit interface between immiscible polymers, the prediction of morphological evolution of immiscible blends during processing is difficult. In this work, constitutive equations for complex interfaces in affine deformation are formulated based on the Finger strain tensor. In chapter 2, three equivalent solutions to the Cauchy stress tensor are derived by differentiating the interfacial energy with respect to the Finger strain tensor for affine deformation. A variable is defined to represent the interfacial orientation degree based on the Finger strain tensor, which makes it possible to show the evolution of interfacial orientation in different deformation fields straightforwardly.

The solution developed in chapter 2 assumes affine deformation and is not suitable for viscoelastic polymer blends with relaxation effects. To address this issue, the memorized strain $\mathbf{B}_e$ is distinguished from the total strain. The interfacial orientation degree for interfaces with relaxation effects is now described with $\mathbf{B}_e$, which can be obtained via an energy balance approach. The evolution of interfacial orientation degree in

different deformation fields with relaxation effects considered are calculated. The modeling results of interfacial orientation degree at different temperatures are compared with the stress relaxation results of PP/PS blends and give consistent predications for the change of relaxation rate with the experimental results.

Based on the results of constitutive modeling and characterization, a processing methodology employing nearly co-continuous structure is proposed and demonstrated with two case studies. In the first case study, PP/PS blend is used for fiber preparation. The "nearly co-continuous structure" is generated with a simple melt blending process. Key points in this methodology also include using a small jet stretch almost equal to zero and separate hot drawing at a suitable temperature. The obtained fiber with our methodology has a tensile strength of more than 300 MPa, which is much higher than that prepared with the traditional melt spinning method.

The second case study aims to explore developing fiber-based products with novel properties from immiscible polymers. Fiber prepared from co-continuous PCL/OBC blends shows a supercontraction ability upon heating. The shrinkage ratio is as high as 8 times. During heating, there is a shrinking stress generated, which is measured with DMA. The supercontraction fiber has a tensile strength of around 80 MPa. Cyclic tensile testing indicates the fiber can be reused.

In summary, in this thesis study, we adopt a "nearly co-continuous structure" and employ such a morphology for materials processing and products realization when immiscible polymer blends are encountered. This nearly co-continuous structure is considered significant from both engineering and economics perspectives. The thesis starts

with constitutive modeling of the dynamics of complex interfaces, leading to equations for the Cauchy stress tensor and the evolution of interfacial orientation in both affine deformation and situations where relaxing effects need to be considered. With the help of constitutive modeling and characterization, a methodology has been designed for producing valuable fiber-based products from immiscible polymer blends. Two case studies are used to demonstrate the methodology. Fiber prepared from the PP/PS blend shows improved mechanical properties compared with the fiber obtained via traditional melt spinning. In addition to improved mechanical properties, efforts have also been made to process polymer blend products with novel properties. Particularly, PCL/OBC blend is used as a model system to produce reusable supercontraction fiber which possesses a supercontraction ability upon heating. The overall methodology developed in this thesis work is formulated on the basis of the interfacial dynamics during blends processing where a compatibilizer is absent. Therefore, it may provide a potential route for direct recycling of waste plastics without the use of compatibilizers.

1. INTRODUCTION

1.1 Polymer Blends

After World War II, large-scale production of plastics occurred, and plastics became one of the most popular man-made materials. In the past several decades, the production of plastics has shown continuous growth from 0.35 million tons in 1950 to ~335 million tons in 2016 [1]. Among them, polyolefins, polyvinyl chloride (PVC), polystyrene (PS), and polyethylene terephthalate (PET) are the most popular resin types, accounting for around 85% of the total plastic market. The applications include but are not limited to packaging, building and construction, automotive, electrical and electronic industry, agriculture, etc. With the growth of the economy, the speed of producing new polymers by developing new monomers was not able to fulfill the market demand. Beginning in the 1960s, polymer blending technology began to be used, in which two or more polymers are blended together to create a new material that has different properties. Compared with polymer synthesis, polymer blending can combine several properties in one product with a faster formulation and commercialization process and is a more cost-effective method for developing new products [2]. One successful example of polymer blending is the development of high impact polystyrene (HIPS), a styrene-based material with high impact resistance endowed by the rubber phase [3]. Currently, polymer blend products are widely used in various fields like healthcare, aerospace, consumer electronics and automotive industry. According to the BCC market research, the polymer blend market reached 26.3 billion pounds in 2016 and will continue to grow in the future [4].

From a thermodynamic point of view, polymer blends may be miscible or immiscible. The miscibility of two polymers under constant temperature and constant pressure may be evaluated using the Gibbs free energy, defined by Eq. 1 [2]:

$$\Delta G_M = \Delta H_M - T\Delta S_M \quad (1)$$

In this equation, ΔG_M is the change in the Gibbs free energy; ΔH_M is the enthalpy change, ΔS_M is the entropy change and T is the absolute temperature. If ΔG_M is positive, then these two polymers are considered to be immiscible; otherwise, they are miscible. When two polymers are blended, the value of ΔS_M is small because of their high molecular weight, and therefore, the value for the term $T\Delta S_M$ is small. In order for ΔG_M to be negative, ΔH_M must be a negative number or a small positive number. In other words, the blending of two polymers need to be exothermic or mildly endothermic, meaning there exists a favorable interactions (e.g. hydrogen bonding, dipole-dipole interaction, charge transfer complexation) between these two polymers. Since these interactions are not common, most polymer blends are immiscible and will generate phase-separation. Therefore, polymer blends can have different morphologies including droplet-matrix, matrix-fiber, lamellar, co-continuous phase morphology or combinations of several elementary phase morphologies [5]. With different concentration ratio, chemical interaction, molecular weight and processing conditions, etc., polymer blends will possess different morphologies and, therefore, different properties.

1.2 Recycling of Co-mingled Polymers

As already introduced, the use of plastics has increased dramatically. Unfortunately, the wide use of plastics has caused serious environmental problems, which brought about the urgent need of polymer recycling. Polymer waste usually contains multiple types of polymers. Since most polymers are immiscible and have poor interfacial adhesion, direct processing of mixed polymers will very often lead to products with poor mechanical properties. Therefore, one popular method of dealing with such co-mingled plastic waste is to separate them into pure polymer before processing them into value-added products. However, the identification and separation process is costly, has low efficiency, and brings extra requirement on the processing facilities. In addition, with the recent wide use of polymer blend products, there are more and more inseparable plastic wastes. Therefore, handling multi-component plastic waste without identification and separation steps seems to be a better choice for value-added recycling [6]. However, this is not easy to achieve because of the poor mechanical properties brought by the immiscibility of polymers.

The direct processing of polymer mixtures into value-added products remains a challenge for both the industry and the academic community. There are already some research work on the recycling of co-mingled polymer mixture. In 1999, Liu et al. [7] explored the recycling of four different plastics from dismantled Volvo cars: poly(acrylonitrile-butadiene-styrene) (ABS), ABS-polycarbonate (ABS/PC), poly(methyl methacrylate) (PMMA), polyamide (PA). They found that blending ABS and PC/ABS with small amount of impact modifier MBS added made a product with better impact properties than the individual components. The blending of 10% of PMMA into the ABS/ (ABS/PC)/MBS blend did not weaken the mechanical properties because PMMA is miscible with the styrene-acrylonitrile and PC. However, when PA is added into the blend,

the property was deteriorated because PA is an immiscible component. Even adding compatibilizer did not help the blend product have better mechanical properties. De Melo et al. studied how the mechanical properties and morphology of a polypropylene/high-impact polystyrene (PP/HIPS) blend would be influenced by the addition of 2-7% styrene-b-ethylene-co-butylene-b-styrene triblock copolymer (SEBS) [8]. They found that 5% SEBS was able to promote the overall performance of the blend most. Halimatudahliana et al. [9] studied the morphological properties of PS/PP blends with 20/80, 50/50, 80/20 (wt%) using different compatibilizers. Among the four compatibilizers, SEBS worked the best, resulting in a finer degree of dispersion of particles and improving the interfacial adhesion. Equiza et al. used a binary compatibilizer of SEBS/EPR (ethylene-propylene-rubber) or SBR (styrene-butadiene-rubber)/EPR for recycling PE/PP/PS/HIPS blends [10]. They found that the combination of SEBS/EPR was better than SBR/EPR because it possessed a greater chemical structure similarity with the recycled materials investigated. With SEBS/EPR as a binary compatibilizer, the impact resistance of the blends was improved and showed the potential of being reused.

Although compatibilizers have been used to improve the mechanical properties of immiscible blends, they have their own limitations either in validity, availability or economic feasibility. First, there is no “one-size-fits-all” compatibilizer on the market. When the co-mingled plastic waste contains too many types of polymers or has unclear compositions, it will be difficult to find the appropriate compatibilizers. Also, the use of compatibilizers can be expensive even though only a small amount of compatibilizers is used [11]. In addition, using compatibilizers makes the processing more difficult because compatibilizers, generally small molecules, have lower viscosity and are thermally

unstable. Therefore, other methods are needed to improve the mechanical properties of immiscible polymers so that recycling co-mingled waste plastics without separation becomes more approachable both technically and economically. Realizing this, researchers have been investigating methods of simple processing of recycled commingled polymer mixtures without the use of compatibilizers. Elmaghor et al. studied both the influence of high energy irradiation on the morphology and the mechanical properties of the ternary blends of high density polyethylene (HDPE), poly(vinyl chloride) (PVC), and PS [12]. The irradiation was applied after the polymer blends was extruded using a single-screw extruder. While making the morphology of the material more uniform and finer, the high energy irradiation also greatly improved the impact strength of the blend and moderately improved the tensile strength. Suarez et al. also found that the method of gamma-irradiation at proper doses helped improve the mechanical properties of polyethylene blends [13]. Gupta et al. did a study on the recycling of poly (phenylene-ether) (PPE)-based thermoplastic elastomer [14]. In this study, a quaternary blend of styrene–ethylene–butylene–styrene (SEBS)/ethylene vinyl acetate (EVA)/PPE-PS (polystyrene) showed an improved mechanical properties after recycling. This was an important finding because usually the mechanical properties are weakened by recycling. In their case, there was crosslinking formation in the EVA phase and the morphology of dispersed crosslinked EVA phase in co-continuous structure of SEBS and PPE-PS was helpful for improving mechanical properties. Bertin et al. investigated the processing of post-consumer plastic wastes of LDPE/PP blends [15]. They found that extrusion treatment may become a potential method for recycling polyolefin mixture. Especially, the shearing and mixing sections in twin-screw extruder endowed LDPE/PP blends better tensile strength properties

and more homogeneity than the ones treated with single-screw extrusion. Bartlett et al. showed the important influence of processing method and condition on the mechanical properties, inspiring that choosing suitable processing method can be a potential approach of valid value-added recycling of polymer blends [16]. The author used two processes to fabricate the blends, injection molding and compression molding. Depending on the process conditions, the blend exhibited very different mechanical property responses.

1.3 Fiber Spinning

With the development of polymer industry and spinning technology, people have begun to produce synthetic fiber in a cheap and efficient way. Compared with natural fibers, synthetic fiber has advantages like durability, large-scale production and tailored properties. Therefore, over the past decades, synthetic fiber production has become a large industry and used for a variety of commodity products such as clothes, carpets, etc. Nowadays, there are several main methods to make fiber: wet spinning, dry spinning, gel spinning, melt spinning, melt blowing (and solution blowing), electrospinning and centrifugal spinning. In wet spinning, the polymer is dissolved into a solvent and then the polymer solution is spun through a spinneret into a coagulation bath so that the fiber can be obtained because of precipitation. In dry spinning, the polymer solution will go into air instead of a non-solvent after being extruded through the spinneret. The solvent will evaporate quickly and a solid fiber is obtained. Gel spinning is used to obtain high strength fiber. After being extruded from the spinneret, the polymer solution forms a gel which will then go through a series of steps like extraction of solvent and hot drawing and finally form fiber with good mechanical properties. As gel spinning generally involves the use of a large amount of solvent, it is expensive and troublesome. Compared with solution spinning

methods (either dry or wet), melt spinning is a more cost-effective method because it does not use solvents and can operate at higher production speed. The polymer pellets are dried, melted in the extruder and then mixed and filtered to form a homogenized melt which is squeezed out from the spinneret and picked up with a spool [17]. A typical melt spinning setup is shown in Figure 1-1. Melt spinning is a simple process with high production speed and low investment cost. Besides, no solvent is used and the environmental pollution is decreased greatly. The properties of the product from melt spinning can be manipulated in a tailor-made manner. Therefore, melt spinning is widely used in the industry for processing fibers like polyester, nylon, polypropylene, etc. A widely used method for making nano /micro fiber or non-woven products is the melt blowing and solution blowing. In melt blowing, micro and nanofibers are fabricated by extruding a polymer melt through small nozzles surrounded by high speed blowing gas. Melt blowing is efficient and economical and therefore is widely used for commercial production of non-woven fiber products. Solution blowing is kind of similar with melt blowing, but it uses polymer solution instead of polymer melt [18]. Electrospinning is also a method that is used for produce nano or micro-fiber and nonwoven mat. In electrospinning, the polymer solution is charged by an electric field and a jet is created. When this polymer jet travels in air, the solvent evaporates away and the resulting fiber is collected on a metal screen [19]. Centrifugal spinning can also produce nanofibers. In centrifugal spinning, the liquid jet is created by a rotating spinning head. After undergoing a stretching process, the jet will finally fall on the collector and form nanofibers. A schematic introduction of centrifugal spinning is given in Figure 1-2.

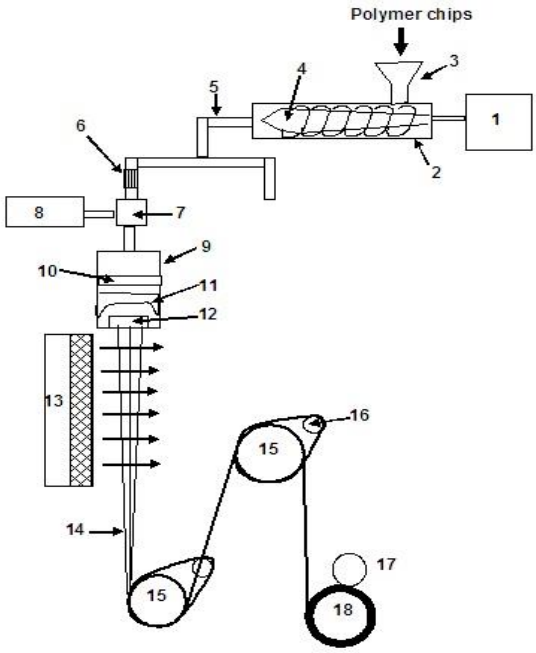

Figure 1-1 Schematic of melt spinning [20].

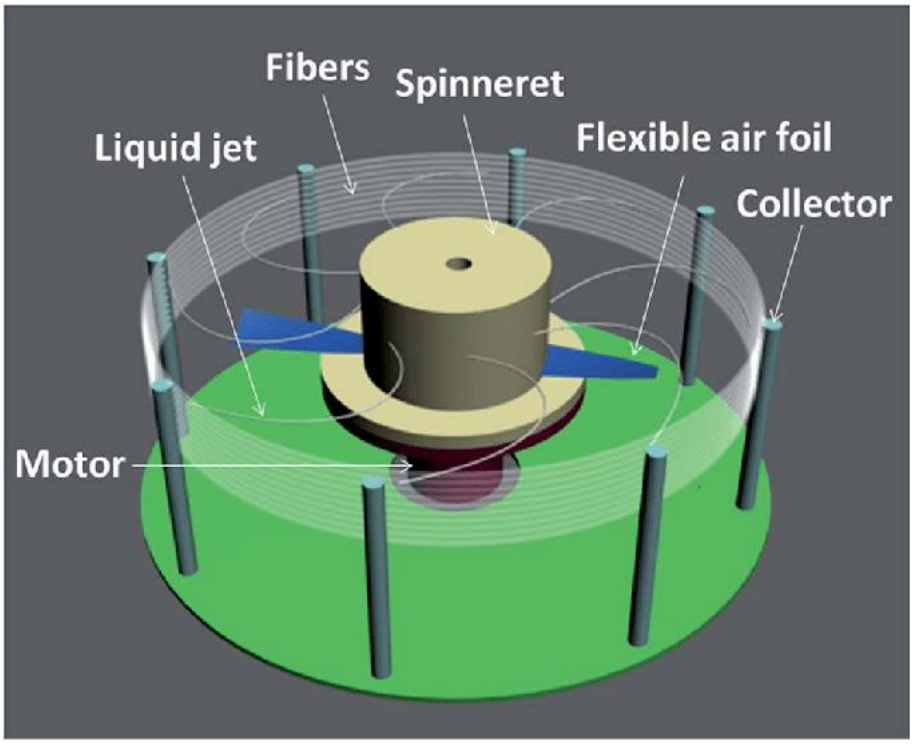

Figure 1-2 Schematic of a basic bench-top centrifugal spinning setup (reused with permission from the publisher of Li, 2017) [21].

1.4 Modeling of Morphology Evolution and Rheological Behavior of Polymer Blends

Most polymer blends are immiscible and the evolution of blend morphology or the microstructure in an immiscible polymer blend is a complex process which is influenced by their interfacial tension, viscosity ratio, stress field and composition, etc. Tailoring and predicting the properties of immiscible blends brings up the need for understanding the morphology/microstructure evolution of immiscible liquid-liquid blends. When processing polymer blends, we need to know about the rheological properties in the flow field, which is influenced by the processing method. The morphology is impacted by the processing conditions and it will in turn influence the rheological properties. This close coupling of flow and structure makes it difficult to predict the morphology evolution and model the rheological behavior. In this section, a brief literature review about the morphology/microstructure evolution and rheological behavior is provided.

1.4.1 Droplet Models

One of the earliest study on the phase morphology is Taylor's theory [22, 23], which is based on Einstein's analysis of the viscosity of a mixture of two liquids-matrix phase and spheres phase [24]. Assuming the droplets are small and nearly spherical, Taylor obtained the following expression of the viscosity of a fluid containing drops of second fluid,

$$\eta^* = \eta_m[1 + 2.5\varphi(\frac{\eta_d + \frac{2}{5}\eta_m}{\eta_d + \eta_m})] \quad (2)$$

In Eq. 2, η^* is the viscosity of the mixture, φ is the volume fraction of the drop phase, η_d is the viscosity of drops, η_m is the viscosity of the matrix fluid. When calculating the drop sizes, Taylor thought that there was a balance between the shear force of the matrix fluid and the surface tension. The size of the drops in a shear field can be expressed as

$$R = \frac{2\Gamma(\eta_d + \eta_m)}{\dot{\gamma}\eta_m(\frac{19}{4}\eta_d + 4\eta_m)} \tag{3}$$

in which R is the drop diameter, Γ is the interfacial tension, $\dot{\gamma}$ is the shear rate.

Taylor [23] also studied the flow-drop deformation in dilute emulsions and deduced the following relation,

$$\frac{l-b}{l+b} = \frac{R\dot{\gamma}\eta_m}{\Gamma}[\frac{19\eta_d + 16\eta_m}{16\eta_d + 16\eta_m}] \tag{4}$$

l and b are respectively the length and width of the deformed drops. According to the experimental results, this equation is valid only when the drop deformation is small and the shear rate is low.

Different work have been done to extend Taylor's theory to more complex situations. For example, Cox [25] studied the shape of a fluid drop in different types of flow and obtained an expression for the deformation of droplets,

$$\frac{l-b}{l+b} = \frac{Ca}{2}[\frac{(19p+16)/(16p+16)}{[(19pCa/40)^2 + 1]^{1/2}}] \tag{5}$$

Two dimensionless parameters, capillary number Ca and droplet/matrix viscosity ratio p, are defined as following,

$$Ca = \frac{R\dot{r}\eta_m}{\Gamma} \tag{6}$$

$$p = \frac{\eta_d}{\eta_m} \tag{7}$$

Considering that Taylor's theory is only applicable to first-order deformation, Chaffey [26] extended the theory of drop deformation to second order and the deformation parameter was able to predict more refined drop behavior than the first-order theory. Acrivos [27] developed a constitutive equation for dilute emulsions. The deformation of a small droplet is treated in a way which takes account more fully the time-dependent effects of the flow and expands to a higher-order deformation. It will reduce to the relation previously proposed by Chaffey when time-dependent effects become small. They obtained two sets of equations, one of which relates the stress to the rate of strain and the local anisotropy and the other one describes the change of the anisotropy with time and the rate of strain. The general equations are complex but for steady shearing flow, they can be reduced and yield the following equations,

$$\eta = \eta_0 \left[1 + \left(\frac{5p+2}{2p+2}\right)\varphi\right] \tag{8}$$

$$\tau_{11} - \tau_{22} = \frac{{\eta_0}^2 \dot{\gamma}^2 R}{40\Gamma}\left(\frac{19p+16}{p+1}\right)^2 \varphi \tag{9}$$

$$\tau_{22} - \tau_{33} = -\frac{{\eta_0}^2 \dot{\gamma}^2 R\varphi}{280\Gamma}\left(\frac{(19p+16)(29p^2+61p+50)}{(p+1)^3}\right)^2 \tag{10}$$

This set of equations show the deformability of droplets caused by the normal stress effects of an emulsion of two Newtonian liquids in steady shear flow, which comes from the opposing effect of interfacial tension on the droplet deformation.

Since polymers are viscoelastic materials, the above theories cannot be applied to polymer blends directly and studies which considers the elastic effect are needed. Tavgac [28] studied how the fluid elasticity would influence the droplets deformation in uniform shear and extensional flow fields. This study showed that the deformation of Newtonian and viscoelastic droplets were different in Couette flow and the viscosity ratio would change the effect of fluid elasticity on the droplet deformation. Fröhlich and Sack studied the dilute emulsion of elastic droplets in a Newtonian liquid in a time-dependent flow and obtained the following rheological equation [29],

$$\left(1 + b_1 \frac{d}{dt}\right)\boldsymbol{\tau} = 2\eta(1 + b_2 \frac{d}{dt})\mathbf{d} \tag{11}$$

with

$$\begin{aligned} \eta &= \eta_0(1 + \frac{5}{2}\varphi) \\ b_1 &= (3\eta_0/2G)(1 + \frac{5}{3}\varphi) \\ b_2 &= (3\eta_0/2G)(1 - \frac{5}{2}\varphi) \end{aligned} \tag{12}$$

where G is the modulus of elastic particles.

Based on Taylor's study, Wu [30] analyzed the formation of dispersed phase for polymer blends. Two nylon 66 resins and one poly(ethylene terephthalate) were used as the matrix phase, and fourteen ethylene-propylene rubbers were used as the dispersed phase. Different from Taylor's work, the dispersed and matrix phases in Wu's work are both viscoelastic and the strain field is a complex combination of nonuniform, transient shear and elongational fields. Wu obtained an empirical equation for predicting the dispersed phase sizes,

$$R = \frac{4\Gamma}{\dot{\gamma}\eta_m}\left(\frac{\eta_d}{\eta_m}\right)^{0.84}, when\ \eta_d > \eta_m$$
$$R = \frac{4\Gamma}{\dot{\gamma}\eta_m}\left(\frac{\eta_d}{\eta_m}\right)^{-0.84}, when\ \eta_d < \eta_m \quad (13)$$

From Eq. 13, it can be seen that dispersed droplet sizes show minimum value when the droplet viscosity is equal to the matrix viscosity, forming a V-shaped curve in the droplet diameter-viscosity ratio plot. The above equations also show that dispersed phase sizes decrease with increasing shear rate, which is inconsistent with some reports in which shear stress variation of two or three times did not affect the droplet sizes that much [31].

Since the above theories deal with single droplets, they work for dilute dispersions but are not applicable to concentrated mixtures. Compared with dilute systems, concentrated mixtures are difficult to analyze. Choi and Schowalter's work [32] is an example of the research on rheological properties of nondilute suspensions. A cell model

is used to account for the influence of neighboring drops. The complications of droplets interactions can be simplified by one or another of several types of cell models, and thus the computational difficulties can be reduced. Compared with dilute systems, the droplets in a moderately concentrated suspension deform more rapidly under the stress and retract more slowly in response to the interfacial tension. Palierne [33] also considered the effects of finite volume fraction.

Breakup of droplets is a phenomenon worthy of attention during liquids mixing. Research involving both experimental observations and theoretical predictions has been performed to study the breakup of droplets. Taylor [23] observed that a low speed under steady extensional flow would make the droplet break up while in steady shear flow field, the droplet did not break up unless the speed was high. Therefore, the type of flow field has large effect on the breakup. Taylor defined the apparent deformation *D* as

$$D = \frac{l - b}{l + b} \tag{14}$$

A dimensionless group E was also defined, namely,

$$E = Ca[\frac{(19p + 16)}{(16p + 16)}] \tag{15}$$

in which Ca is the capillary number and p is the viscosity ratio of droplet phase to matrix phase. Taylor showed that theoretically, the apparent deformation *D* and the dimensionless group *E* both equal 0.5 at breakup. He then demonstrated experimentally that droplet broke up when $D = E = 0.5 \sim 0.6$ when the value of p was in the range of 0.1 to 1.0. Based on the

experimental results and theoretical calculations, Taylor proposed the critical condition for breakup of Newtonian droplets suspended in a Newtonian medium,

$$(Ca)_c = f(p) \tag{16}$$

in which $(Ca)_c$ means the critical value of Ca. A U-shaped contour was obtained by Karam and Bellinger [34] in which when Ca is large or falls above and inside the U-shaped curve the droplet is unstable and will deform and break, while when Ca falls outside the contour it is stable. According to Karam and Bellinger, in uniform shear flow, droplet will break up when viscosity ratio is between 0.005 and 3.0. Breakup will not happen when the viscosity ratio is too high or too low. At too high viscosity ratio, the viscous force cannot overcome the interfacial force. At too low viscosity ratio, the drop will be highly deformed without breakup. Taylor's relation is instructional from the practical point of view because it predicts the critical shear rate required to break up a droplet of a certain size at a suspending medium viscosity and an interfacial tension for a wide range of viscosity ratio.

Different from Taylor's viewpoint, Torza et al. [35] thinks that the droplet breakup depends more on the rate of increase in shear rate than on the viscosity ratio. They also observed an interesting phenomenon that the droplet will be deformed highly into a long threadlike form, then become varicose, and eventually break up into a series of smaller drops. Huneault et al. [36] used a parameter called critical capillary number, Ca_{cr}, to lead to an equilibrium shape or to disintegration into smaller droplets. A reduced capillary number, $Ca^* = Ca/Ca_{cr}$, ratio of the capillary number to the critical capillary number, is defined. The value of Ca^* will determine if the droplets will deform or break:

When Ca^*<0.1, droplets do not deform.

When 0.1< Ca^* <1 droplets deform, but do not break.

When 1< Ca^* <4 droplets deform then disintegrate into smaller droplets.

When Ca^*>4, droplets deform into stable filaments.

For Newtonian systems under shear flow field, the critical capillary number depends on the droplet/matrix viscosity ratio p. If p = 1, then Ca_{cr} equals 1. Ca_{cr} increases when p increases and becomes infinite when p > 3.8. Therefore, in the case of p > 3.8, the breakup of droplets in shear flow will not happen. In stronger flow fields or in elongational flow, the value of Ca_{cr} is lower and less dependent on the viscosity ratio. De Bruijin [37] proposed an empirical equation for calculating the value in shearing flow field:

$$\log(Ca_{cr}) = -0.506 - 0.0994 log\lambda + 0.124(log\lambda)^2 - 0.115/(log\lambda - 0.611) \quad (17)$$

Although the capillary number of viscoelastic systems depends on the elasticity ratio, De Bruijin did not incorporate the elastic effects into his model.

When at least one of the two phases is viscoelastic, the droplet breakup range will be different. For such case, Flumerfelt [38] proposed the following dimensionless groups,

$$(Ca)_c = f(p, \overline{\mathrm{H}_1}\dot{\gamma_c})$$
$$(Ca)_c = f(p, \mathrm{H}_1\dot{\gamma_c}) \quad (18)$$

The two equations in Eq. 18 are respectively for the case of viscoelastic droplets suspending in a Newtonian medium and the case of Newtonian droplets suspended in a viscoelastic medium. $\overline{\mathrm{H}_1}$ and H_1 are respectively the relaxation times of the droplet phase and the suspending medium, which can be determined from using available rheological data for evaluating the material constants in the rheological model. When both phases are viscoelastic, another dimensionless parameter is needed.

The above studies, however, did not consider coalescence. For concentrated polymer blends processing, there will be more coalescence and the final sizes of dispersed particle sizes are decided by a balance of stretching, breaking up and coalescence [39]. Besides, the flow fields in the processing will be more complex and generate high shear and elongational flows. Rheological tools are in great need for better understanding for the evolution of morphology of blends during flow so that we can know more about the process-morphology-property relationship for the purpose of designed processing.

1.4.2 Interface Tensor Theories

The situation of lacking good description for morphology and rheology of highly concentrated suspension changed when Doi and Ohta [40] proposed the interface tensor theory, in which they treated the system of a mixture of two immiscible fluids having the same viscosity and density and mixed with the volume ratio of about 1:1. Instead of considering the droplets, they focused on the complex interface which is well distributed

in the bulk. The interface is considered as a third phase and contributes to the Cauchy stress tensor by $\mathbf{T}_{\text{interface}}$,

$$\mathbf{T}_{\text{interface}} = -\Gamma\mathbf{q} \tag{19}$$

in which Γ is the interfacial tension and **q** is the interfacial conformation tensor. As a microstructural variable, **q** is used to characterize the orientation/anisotropy of the interfaces, defined as

$$\mathbf{q} = \frac{1}{V}\int_{\Psi}\left(\mathbf{n}\otimes\mathbf{n} - \frac{1}{3}\mathbf{I}\right)da, \tag{20}$$

where Ψ is the total interface, **n** is a unit normal vector to a local interface, **I** is the identity tensor and a is the interfacial area.

In addition to **q**, another variable Q, the interfacial area per unit volume, is also needed for characterizing the interface,

$$Q = \int d\mathbf{n} f(\mathbf{n}) \tag{21}$$

where the interface density function f(**n**) denotes the area of interfaces normal to **n** per unit volume.

The flow field, expressed with the macroscopic velocity gradient **L** = ə**v**/ə**x** enlarges and orients the interface and the interfacial tension depresses these effects. They treated the two effects separately so that,

$$\dot{\mathbf{q}} = \dot{\mathbf{q}}_{\text{flow}} + \dot{\mathbf{q}}_{\text{relax}}$$
$$\dot{Q} = \dot{Q}_{\text{flow}} + \dot{Q}_{\text{relax}} \tag{22}$$

The total stress tensor is composed from three contributions: the viscous contribution, the interfacial stress, and the isotropic pressure term

$$\mathbf{T} = \eta\mathbf{D} - \Gamma\mathbf{q} - p\mathbf{I} \tag{23}$$

where $\mathbf{D} = \mathbf{L} + \mathbf{L}^{\mathrm{T}}$ and p is the isochoric pressure.

The calculation for $\dot{\mathbf{q}}$ and $\dot{Q}$ is complex because a fourth-order tensor appears. For the case of affine deformation in a homogeneous flow field, Doi and Ohta were able to derive the following evolution equation by reducing the fourth-order tensor to second-order tensor with a quadratic closure,

$$\dot{\mathbf{q}} = -\mathbf{q}\cdot\mathbf{L} - \mathbf{L}^{\mathrm{T}}\cdot\mathbf{q} + \frac{\mathbf{2}}{\mathbf{3}}(\mathbf{q}:\mathbf{L}^{\mathrm{T}})\mathbf{I} - \frac{Q}{\mathbf{3}}(\mathbf{L}+\mathbf{L}^{\mathrm{T}}) + \frac{1}{\mathrm{Q}}(\mathbf{q}:\mathbf{L}^{\mathrm{T}})\mathbf{q}$$
$$\dot{Q} = -\mathbf{L}^{\mathrm{T}}:\mathbf{q} \tag{24}$$

To include the relaxation effects caused by interfacial tension, they adopted the simplest relaxation equation and one relaxation time each was used for area and anisotropy. The time-evolution equation for the interface shape and size in flow were obtained,

$$\dot{\mathbf{q}} = -\mathbf{q}\cdot\mathbf{L} - \mathbf{L}^{\mathrm{T}}\cdot\mathbf{q} + \frac{\mathbf{2}}{\mathbf{3}}(\mathbf{q}:\mathbf{L}^{\mathrm{T}})\mathbf{I} - \frac{Q}{\mathbf{3}}(\mathbf{L}+\mathbf{L}^{\mathrm{T}}) + \frac{1}{Q}(\mathbf{q}:\mathbf{L}^{\mathrm{T}})\mathbf{q} - mQ\mathbf{q}$$

$$\dot{Q} = -\mathbf{L}^{\mathrm{T}}:\mathbf{q} - \lambda\mu Q^2 \tag{25}$$

where $m = (c_1+c_2)\Gamma/\eta_0$, $\mu = c_1/(c_1+c_2)$, c_1 and c_2 are positive numbers which may depend on the volume fraction. The above two equations plus the stress equation give the rheological constitutive equation for this system with complex interfaces. This theory predicts a scaling property that the shear stress and the first normal stress difference are proportional to the shear rate.

Takahashi et al. [41] verified experimentally that these scaling relations were true for mixtures of immiscible Newtonian fluids with the same viscosity and different compositions. They observed that both the shear stress and the first normal stress difference were almost proportional to the shear rate. However, the prediction by Doi and Ohta's constitutive equation turned out to be different from the observed time dependence of the transient stress and the author thought that this inconsistency was caused by the inaccuracy of the phenomenological relaxation equation in the Doi and Ohta theory. Takahashi et al. [42] also studied the viscoelastic properties of binary blends of immiscible polymers with almost the same viscosity under steady and transient shear flows. They found that the scaling relations proposed by Doi and Ohta held for blends of polymers of equal viscosity with different composition ratios. Vinckier et al. [43] investigated the case when the Doi and Ohta model was used with blends of polymers with different viscosity ratios and found that the relations would be obeyed only when the viscosity ratio less than a value of 4 and when the shear rate less than a critical value.

Since the Doi-Ohta theory has its limitations, more recent modeling work on deformation of complex interfaces have extended this theory to include additional effects. For example, Lee and Park [44] proposed a new model based on Doi and Ohta' work and the resulting model is applicable to polymer blends with different viscosities. They introduced a viscosity ratio term and refined the relaxation mechanisms involved during flow. The new prediction applied to dynamic oscillatory flow proved to be valid for immiscible polymer blends for the whole frequency range and all compositions. Ei Afif et al. [45] investigated the case when diffusion needed to be considered and derived nonlinear formulations which included the contributions of the diffusion fluxes and the isotropic and anisotropic deformations of the interface. Gu and Grmela [46] developed the governing equations of the Doi-Ohta model with active advection. Results of the extended model were compared with experimental data and the original Doi-Ohta model from the following two folds: (i) the morphology of the interface, which are expressed in the interface tensor **q** and the unit surface area of the interface Q, and (ii) the rheological behavior. It was found that the extended model agreed more with the observed behavior. Considering the computational complexity and the inaccuracy introduced by transforming the fourth-order tensor to second-order tensor in the Doi-Ohta model, Wetzel and Tucker [47] used a variable similar with the interface tensor called the area tensor for describing the morphology of immiscible mixtures. When estimating higher-order microstructural statistics, they generated a closure approximation based on exact area tensor relations for ellipsoidal shapes and provided a highly accurate evolutions of area tensor. The area tensor is different from the interface tensor by an isotropic part, as expressed by,

$$\boldsymbol{A} = \frac{1}{V}\int_{\Psi} \mathbf{n}\otimes\mathbf{n}da, \tag{26}$$

where the integral is taken over the entire interfacial surface Ψ within the averaging volume V.

Based on the chain rule, the evolution equation for the area tensor can be written as

$$\dot{\boldsymbol{A}}\boldsymbol{A} = \frac{1}{V}\int_{\Psi} \dot{\mathbf{n}}\mathbf{n}da + \frac{1}{V}\int_{\Psi} \mathbf{n}\dot{\mathbf{n}}da + \frac{1}{V}\int_{\Psi} \mathbf{n}\mathbf{n}\dot{a} \tag{27}$$

Combining Eq. 27 with Chella and Ottino's expression [48] of the normal vector of a differential area in passive mixing and the magnitude of the differential area change, a simplified evolution equation for the area tensor can be obtained

$$\dot{\boldsymbol{A}}_{ij} = -L_{ki}A_{kj} - A_{ik}L_{kj} + L_{kl}\mathscr{A}_{klij} \tag{28}$$

where **L** is the velocity gradient tensor, $L_{ij} = \partial v_i/\partial x_j$ and $\mathscr{A} = \frac{1}{V}\int_{\Psi} \mathbf{n}\otimes\mathbf{n}\otimes\mathbf{n}\otimes\mathbf{n}da$ is a fourth-order tensor. The fourth-order tensor cannot be calculated explicitly and needs to be approximated in terms of the second-order tensor. If expressing Doi's method of the quadratic closure using the normalized tensors $\boldsymbol{A}$, the approximation will be

$$\mathscr{A}_{klij} = A_{ij}A_{kl} \tag{29}$$

Different from this method, Wetzel and Tucker approached the fourth-order tensor with a closure approximation based on exact area tensor relations for ellipsoidal shapes,

referred to as RE, or rational ellipsoidal, closure and obtained highly accurate evolutions of the area tensor.

In a nutshell, Doi-Ohta's theory is an important step for understanding the flow and the structure coupling although it has its own limitations. By treating the mixture as two components with a complex interface that is well distributed in the bulk, Doi and Ohta established a new path for approaching the dynamic physics of concentrated emulsions. Instead of considering various discrete drops, their theory treats the interface as a third phase, which contains rich information that help correlate the structure and the rheology. With the various work on extending or enriching the Doi-Ohta theory and experimentally verifying it, the understanding on the dynamic rheology and morphology on polymer blends mixing/processing has been greatly enriched.

1.5 Fiber Made from Multi-Component Polymers

Fiber spinning, as a processing method which has different characteristics from other processing methods, has the potential to endow improved properties and more applications to polymer blends. On the other hand, fiber from polymer blends may have new properties compared with fiber from pure polymers. Therefore, combining fiber spinning technology and immiscible polymer blends to produce polymer blend fiber is an interesting topic.

Many researches have been done on the morphology and properties on immiscible polymer blends. For immiscible polymer blends, the phase morphology is influenced by flow and processing conditions, component ratio, viscosity ratio, interfacial tension, etc. Different phase morphology will bring different properties [49]. There are two common morphologies widely studied: co-continuous structure and dispersed phase-matrix

structure. In many cases, fiber from immiscible polymer blends holds to these two morphologies. In the dispersed phase-matrix structure, the dispersed phase may exist as forms of sphere, laminar or fibril.

David et al. studied the morphology of blends containing 85% polyethylene and 15% styrene-isoprene-styrene triblock copolymers, in which different morphologies (spheres, elongated droplets, fibrils and extended co-continuous phases) were produced under different extrusion conditions [49]. Different studies have been done on the matrix-fibril type morphology. Factors like the mixing method, interfacial tension, elasticity, shear stress and viscosity will all influence the deformation of droplets into fibrils. Tsebrenko et al. made blend from polyoxymethylene (POM) and a copolymer of ethylene and vinyl acetate (CEVAc), and found that it was the viscosity ratio of POM and the matrix polymer that determined if the POM phase was able to form fibril in the blend. Besides, they also showed the morphology of the blend was also influenced by the extrusion shear stress and there was an optimum shear stress for the formation of ultrathin fibril-matrix morphology [50]. Fiber spinning turned out to be a more effective method for producing the fibril-matrix morphology because of the drawing process. Varma [51] showed that the sphere phase of PET in the nylon6/ PET blends was turned first into rod-like shape and then further into fibrils in the melt spinning of this blend. A potential benefit of the matrix-fibril morphology is that it may improve mechanical properties. In the aforementioned study of nylon6/PET blends, despite the blend is immiscible, the mechanical properties of the blend fiber was improved because the fibril played a role of reinforcement and promoted the crystallization of nylon 6. In addition, research has also been conducted to investigate the

use of the fibril-matrix morphology for preparation of micro or nano fibers after extraction of the matrix phase [52].

Another morphology which is also of great interest to researchers is the co-continuous structure. In co-continuous structure, also referred to as interpenetrating network, both of the two phases are continuously connected throughout the blend. Previous researchers have explored the processing and rheological conditions for generating co-continuous structure in immiscible blends [53] and demonstrated blends with co-continuous structure show improved mechanical properties than those with one-phase-being-dispersed structure [54]. The phase morphology control in preparing co-continuous blend has been done by different researchers and different models were proposed to predict the phase inversion point, around which co-continuous morphologies are most likely to form [55].

Although there are numerous studies on the morphology and properties of immiscible polymer blends with co-continuous structure, there are not much research work on processing immiscible co-continuous polymer blends into fiber. Tang et al. prepared cellulose acetate/polyurethane fiber with co-continuous structure via electrospinning and studied fiber structures, mechanical properties and thermal properties [56]. However, their process involves the use of organic solvent and is not so applicable for large-scale production. Making fiber from immiscible polymer blends with co-continuous structure using the simpler and more environmental-friendly melt spinning process would be an interesting subject. Questions like how the co-continuous structure will deform need to be answered to understand the process-structure-property relationship and improve mechanical properties.

Besides phase morphologies, the existing research on fiber from immiscible blends also studied the rheological properties and structure development. Although the two polymers are immiscible and have poor interfacial adhesion, the interaction between them still influences the rheological properties and structure development. Liang et al. prepared a series of PP/nylon 6 blends of composition 75/25, 50/50, 25/75 [57]. They used SEM to observe the morphology and check the phase size growth. They also measured the rheological properties and checked the structure development during the melt spinning of fibers. The crystalline orientation of both PP and nylon 6 increased with the drawdown ratio and the orientation of the PP phase was not influenced by the existence of nylon 6. Different from this observation on the PP crystalline orientation, in another study on the melt-spun PE/PS fiber, the crystalline orientation of the PE phase was significantly reduced by the coexisting PS, which was considered to be caused by the greater temperature dependence of the viscosity of the PS [58].

In addition to the melt spinning of pre-mixed polymer blends, there is another method for making fiber from multi-component polymers: bicomponent spinning. In bicomponent spinning, the two polymers are not pre-mixed but coextruded into the spin pack from two melt streams. An example of the spinning process of bicomponent spinning is shown in Figure 1-3. Determined by the spin pack, the final fiber may have different cross-sectional geometry, including but not limited to core-sheath structure, side-by-side structure and island in the sea structure [59]. In the single component spinning of multi-polymers, the control of phase morphology is often challenging because incompatibility between the polymers results in phase separation. Bicomponent spinning offers an alternative way of preparing blend fibers with controlled morphology, improved processing and synergistic

properties. However, bicomponent spinning is technically more complex than single component spinning and may have higher requirements on the choice of polymers. For example, two materials with large viscosity difference will rearrange themselves during the extrusion and the morphology may not be the desired one. Bicomponent spinning also needs a complex spin pack, which may increase the cost. As in the case of preparing fiber with sea-island structure, a complex spin pack which can stuff many droplets into each fiber cross-section will be needed.

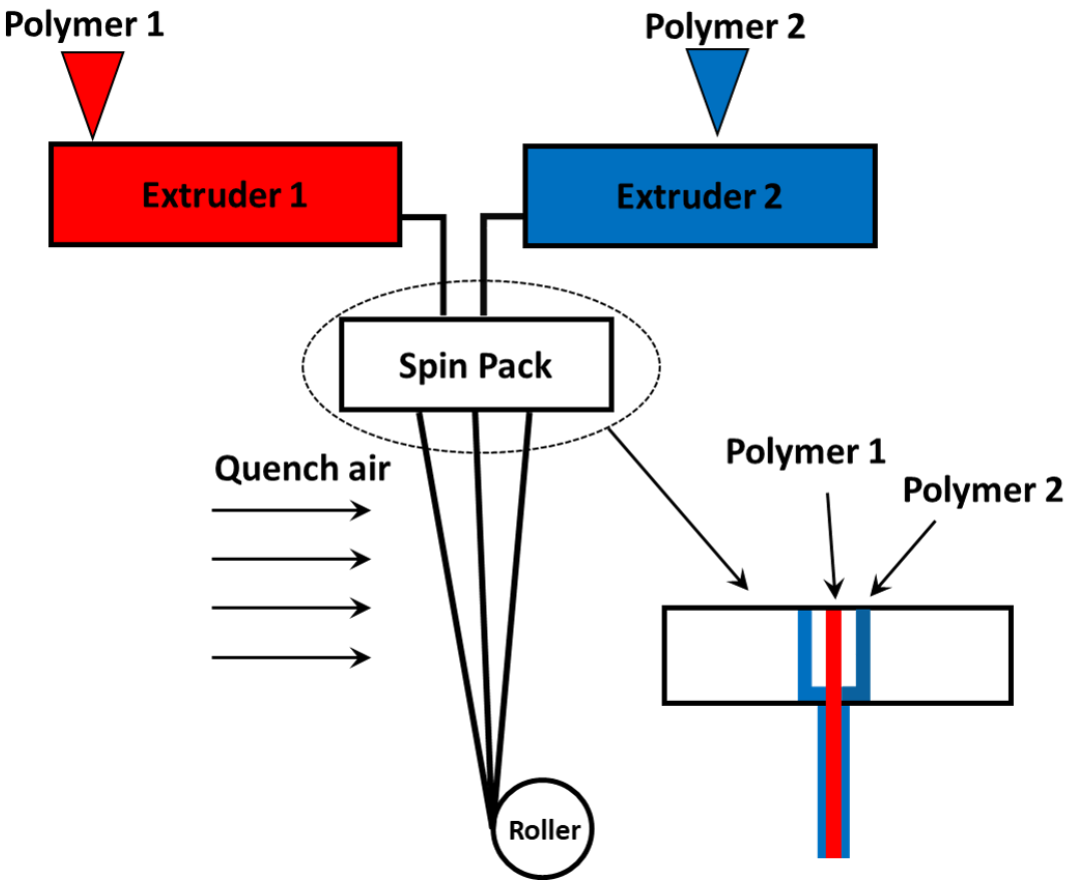

Figure 1-3 Schematic of bicomponent spinning.

1.6 Challenges and Motivations

A simple, efficient and cost-effective method of processing immiscible polymer blends is greatly needed, which may be used in the direct recycling of waste plastics and new polymer blends products development. Currently, many studies used compatibilizers to improve the mechanical properties, which has many limitations including high cost, low availability and processing difficulties. In this thesis work, we have studied the evolution of morphologies during polymer blends processing and focused on how to obtain desired morphologies and properties via specific process design. Among various morphologies, co-continuous structure is worth special attention because it can help weaken the undesired effects of the poor interfacial adhesion in immiscible polymers and improve the mechanical properties [60]. Co-continuous structure in immiscible blends can be generated under appropriate processing and rheological conditions [53]. Therefore, preparing polymer blends with co-continuous phase structures is a potential method for achieving good mechanical properties. Although the phase morphology control in preparing co-continuous blend has been done by different researchers, how to make strong fiber from co-continuous blends is an issue that needs to be studied.

The objective of this thesis work is to design a methodology for processing immiscible polymer blends into mechanically usable fiber-based products without the use of compatibilizers, which may be used in recycling multi-component polymer waste when combined with some additional efforts. In addition, by choosing a suitable combination of materials, novel properties may be added, opening up new blend products innovation. We will employ “a nearly co-continuous morphology” for materials processing and products realization of immiscible polymer blends. This nearly co-continuous structure is considered significant from both engineering and economics perspectives by creating a

cost-effective and yet capable process for achieving desired properties and performances of products, especially fiber-based products. Increasing amount of work on predicting the morphological evolution have been done for instructing the polymer processing. However, because of the presence of an implicit interface and the strong coupling between the morphology and rheology, the morphological prediction of phase structure evolution during polymer processing is complex and challenging. In this work, constitutive modeling of complex interfaces based on a path-independent interfacial energy function will be performed to help the process design. The interfacial orientation degree with the interfacial relaxation effects considered can be expressed via the Finger strain tensor. Based on constitutive modeling and characterization results, a methodology of producing fiber from immiscible blends has been designed. To demonstrate this new paradigm of polymer processing, two case studies, in which immiscible polymer blends are made into fibers with value-added properties, will be performed. The first case study prepares blend from polypropylene (PP) and polystyrene (PS) and can produce blend fiber with good mechanical properties despite the immiscibility of PP and PS. The second case study makes blend fiber from polycaprolactone (PCL) and ethylene-octene block copolymer (OBC), which shows super-contraction capability upon heating. In a nutshell, using constitutive modeling and analysis to facilitate the process design, we will explore how the process affects the structure and properties on micro and molecular levels and provide potential approaches for direct recycling of co-mingled plastics without the use of pre-separation procedure or compatibilizers.

2. CONSTITUTIVE MODELING OF COMPLEX INTERFACES IN AFFINE DEFORMATION

2.1 Introduction

As introduced in Chapter 1, Doi and Ohta [40] proposed a theory in which they approached the problem of morphology and rheology of a roughly 50:50 co-continuous blend with two immiscible Newtonian fluids by studying the complex interface between the two phases. Interfacial conformation tensor **q**, which contains information on the orientation/anisotropy of the mixture, together with Q, the interfacial area per unit volume, characterize the interface and evaluate the morphological change of the two phase mixture. The variable **q** and Q are defined by

$$\mathbf{q} = \frac{1}{V}\int_{\Psi} \left(\mathbf{n}\otimes\mathbf{n} - \frac{1}{3}\mathbf{I}\right) da, \tag{30}$$

$$Q = \int d\mathbf{n} f(\mathbf{n}) \tag{31}$$

They also proposed the idea of calculating the interfacial contribution to the stress tensor from the interfacial conformation tensor, which is adopted by later researchers. Specifically, the stress tensor is related by **q** according to

$$\mathbf{T}_{\text{interface}} = -\Gamma\mathbf{q} \tag{32}$$

The calculation of the time evolution is complex because of a fourth-order tensor, which is generated via the following equation:

$$\frac{\partial}{\partial t}\overline{n_\alpha n_\beta} = \int d\mathbf{n}\overline{n_\alpha n_\beta}\mathbf{n} \times \frac{\partial}{\partial \mathbf{n}} \cdot [\mathbf{n} \times (\boldsymbol{L}^{\boldsymbol{T}} \cdot \mathbf{n})f] - \overline{n_\alpha n_\beta n_\mu n_\nu} L_{\mu\upsilon} \tag{33}$$

Doi and Ohta used a decoupling approximation to reduce the fourth-order tensor to second-order tensors, that is,

$$\overline{n_\alpha n_\beta n_\mu n_\nu} L_{\mu\upsilon} = \frac{1}{Q}\overline{n_\alpha n_\beta} \cdot \overline{n_\mu n_\nu} L_{\mu\upsilon} \tag{34}$$

With the above equation, the evolution equations for $\mathbf{q}$ and Q can be obtained,

$$\dot{\mathbf{q}} = -\mathbf{q} \cdot \mathbf{L} - \mathbf{L}^{\mathrm{T}} \cdot \mathbf{q} + \frac{\mathbf{2}}{\mathbf{3}}(\mathbf{q}{:}\,\mathbf{L}^{\mathrm{T}})\mathbf{I} - \frac{Q}{\mathbf{3}}(\mathbf{L} + \mathbf{L}^{\mathrm{T}}) + \frac{1}{Q}(\mathbf{q}{:}\,\mathbf{L}^{\mathrm{T}})\mathbf{q} \tag{35}$$

$$\dot{Q} = -\mathbf{L}^{\mathrm{T}}{:}\,\mathbf{q} \tag{36}$$

To estimate the accuracy of the decoupling approximation, they compared the results obtained from the above equations with the rigorously calculated ones for the cases of conformal shear deformation and uniaxial elongation.

The decoupling approximation used in Doi and Ohta's theory introduced error. Wetzel and Tucker proposed another closure method called RE (rational ellipsoidal) and demonstrated better accuracy for affine deformation.

Both the methods of Doi-Ohta and Wetzel-Tucker need to deal with the complex fourth-order tensor and a method with less computational cost is needed. Yao [61] presented a different formulation for this problem via a path-independent interfacial energy function. A nearly closed-form solution for the Cauchy stress tensor was obtained via

differentiating the interfacial energy function against the right Cauchy-Green strain tensor. Three types of equations for describing the Cauchy stress tensor were derived:

$$\mathbf{T} = \frac{2}{J}\mathbf{F}\cdot\frac{\partial U}{\partial \mathbf{C}}\cdot\mathbf{F}^{\mathbf{T}} = \frac{2}{J}\mathbf{F}\cdot\frac{\partial\left((\Gamma J/V_0)\int_{\Psi_0}\sqrt{\mathbf{C}^{-1}:(\mathbf{n}'\otimes\mathbf{n}')}da'\right)}{\partial \mathbf{C}}\cdot\mathbf{F}^{\mathbf{T}} \tag{37}$$

$$\mathbf{T} = \frac{\Gamma}{V_0}\int_{\Psi_0}\left[\mathbf{I} - \frac{\mathbf{F}^{-\mathbf{T}}\cdot(\mathbf{n}'\otimes\mathbf{n}')\cdot\mathbf{F}^{\mathbf{T}}}{\sqrt{\mathbf{C}^{-1}:(\mathbf{n}'\otimes\mathbf{n}')}}\right]da' \tag{38}$$

$$\mathbf{T} = \frac{\Gamma}{V}\int_{\Psi}\left[\mathbf{I} - \mathbf{n}\otimes\mathbf{n}\right]da \tag{39}$$

where ψ_0 denotes the initial interface and V_0 is the volume of the material before deformation. It can be proved that these three types of equations are equivalent. However, type 3 is not easy to use because it is difficult to calculate the **nn** tensor, which represents the deformed state. In comparison, type 1 model using the Lagrangian description is more accessible because in most cases the initial morphology, which is described by $\Delta\boldsymbol{a}'$ and $\mathbf{n}'\mathbf{n}'$, is known. The process of derivation involves only elementary algebraic and matrix operations. Compared with the Doi-Ohta theory, this method removes the mathematical complexity of dealing with the fourth-order tensor and shows improved fitting to the exact solutions.

In this chapter, constitutive equations for complex interfaces and blends will be formulated based on the left Cauchy-Green strain tensor, i.e. the Finger strain tensor. Compared with the right Cauchy-Green strain tensor, the Finger strain tensor is more convenient and maneuverable and closely related with the orientation degree of the

interface/blends. Making use of the Finger tensor, which arises naturally in both equilibrium thermodynamics and classical mechanics, we can approach the problem of interface morphology and deformation from the perspective of nonlinear viscoelasticity.

2.2 Preliminaries

When a certain deformation is applied on a continuum medium, a point with a position vector $\mathbf{x}'$ in the undeformed state is displaced into point with a position vector $\mathbf{x}$. Two methods of description are used to describe the kinematics and dynamics of a material point since two position vectors are involved. In the Lagrangian description, a physical quantity of a material point is used according to the original position vector $\mathbf{x}'$ and the time t. In the Eulerian description, the current position vector $\mathbf{x}$ in the deformed state is used. The deformation gradient $\mathbf{F}$, a second order tensor, is defined by

$$\mathbf{F} = \frac{\partial \mathbf{x}}{\partial \mathbf{x}'} \tag{40}$$

As an invertible tensor, the determinant or Jacobian of $\mathbf{F}$ equals

$$J = det\mathbf{F} \neq 0 \tag{41}$$

From Eq. 40, we can obtain the following differential

$$d\mathbf{x} = \mathbf{F} \cdot d\mathbf{x}' \tag{42}$$

This equation describes that a differential segment $d\mathbf{x}'$ in the original configuration is mapped into a deformed segment d**x** in the deformed configuration. Considering the lengths of the two segments, we can write

$$\begin{aligned} d\mathbf{x} \cdot d\mathbf{x} &= (\mathbf{F} \cdot d\mathbf{x}') \cdot (\mathbf{F} \cdot d\mathbf{x}') = d\mathbf{x}' \cdot (\mathbf{F}^{\boldsymbol{T}} \cdot \mathbf{F}) \cdot d\mathbf{x}' \\ &= (\mathbf{F}^{\boldsymbol{T}} \cdot \mathbf{F}) : (d\mathbf{x}' \otimes d\mathbf{x}') \end{aligned} \tag{43}$$

$\mathbf{F}^{\boldsymbol{T}} \cdot \mathbf{F}$, denoted as **C**, is the right Cauchy-Green tensor, which is related to the stretch of the line segments.

Similarly, we can map a differential area $d\mathbf{a}' = d\mathbf{x}' \times d\mathbf{x}'$ in the original configuration into an area in the deformed configuration $d\mathbf{a} = d\mathbf{x} \times d\mathbf{x}$. $d\mathbf{a}'$ has a unit normal $\mathbf{n}'$ and an area da', and d**a** has a new unit normal **n** and a new area da. The corresponding variables in the original configuration and in the deformed configuration can be transformed using the following relations:

$$\begin{aligned} d\mathbf{a} = d\mathbf{x} \times d\mathbf{x} &= (\mathbf{F} \cdot d\mathbf{x}') \times (\mathbf{F} \cdot d\mathbf{x}') = (\det\mathbf{F})\mathbf{F}^{-\boldsymbol{T}}(d\mathbf{x}' \times d\mathbf{x}') \\ &= (\det\mathbf{F})\mathbf{F}^{-\boldsymbol{T}} \cdot d\mathbf{a}' \end{aligned} \tag{44}$$

$$\frac{da}{da'} = J\left|\mathbf{F}^{-\boldsymbol{T}} \cdot \mathbf{n}'\right| = \frac{J}{\left|\mathbf{F}^{\boldsymbol{T}} \cdot \mathbf{n}\right|} \tag{45}$$

$$\mathbf{n} = \frac{\mathbf{F}^{-\boldsymbol{T}} \cdot \mathbf{n}'}{\left|\mathbf{F}^{-\boldsymbol{T}} \cdot \mathbf{n}'\right|} \tag{46}$$

Taking a dot product of $d\mathbf{a}' \cdot d\mathbf{a}'$, we can get

$$d\mathbf{a}' \cdot d\mathbf{a}' = [(\det\mathbf{F})^{-1}\mathbf{F}^{T} \cdot d\mathbf{a}] \cdot [(\det\mathbf{F})^{-1}\mathbf{F}^{T} \cdot d\mathbf{a}]$$
$$= (\det\mathbf{F})^{-2} d\mathbf{a} \cdot (\mathbf{F} \cdot \mathbf{F}^{T}) \cdot d\mathbf{a} \tag{47}$$

in which the tensor $\mathbf{F} \cdot \mathbf{F}^{T}$ is referred to as the left Cauchy-Green tensor or the Finger tensor, denoted as **B**. The Finger tensor is inherently connected with the shape and size change of the material point in the deformed state and therefore, is more useful in continuum mechanics than the right Cauchy-Green tensor **C**. The Finger tensor can directly represent the material orientation and state stretch in the deformed state, which can be proved by considering the ellipsoidal approximation of the Finger tensor. That's one reason why we will formulate constitutive equations for complex interfaces and blends as a function of the Finger tensor in this chapter.

2.3 Stress Tensor Derivation for Affine Deformation

Here we will assume the deformation is affine deformation and not consider the relaxation for now. Since the interfacial energy is proportional to the interfacial area, we can express the interfacial energy for a small area Δa (before deformation $\Delta a'$**)** as the following:

$$U = \Gamma \Delta a = \Gamma \Delta a' \mathrm{J} |\mathbf{F}^{-T} \cdot \mathbf{n}'| \tag{48}$$

In this work, we adopted a concept called ellipsoidal equivalency proposed by Yao [62]. The initial area of the interface is assumed to be equal to the surface area of the unit sphere. After deformation, the complex interface can be represented by the surface of an ellipsoid, whose characteristic tensor **M** is equal to the Finger strain tensor **B**. This equivalency is

valid for co-continuous polymer blends because the complex interface is three-dimensionally randomly co-continuous; in other words, the complex interface and the surface of a spherical structure are both distributed isotropically. Besides, it is also applicable for the blend with a droplet-matrix structure as the shape of the droplet is sphere before the deformation and ellipsoid after the deformation and therefore, the interface is the surface area of the elliptical droplet. The ellipsoidal equivalency greatly increases the computational convenience as it allows the evolution of the area and the stress tensor for complex interfaces during conformal deformation to be written as single functions of the Finger tensor and reduces the problem to finding the evolution equation of the Finger tensor during deformation.

The interfacial energy function as defined in Eq. 48 can be written as the following,

$$U = \Gamma \Delta a = \Gamma \Delta a' J \sqrt{(\mathbf{F}^{-\boldsymbol{T}} \cdot \mathbf{n}') \cdot (\mathbf{F}^{-\boldsymbol{T}} \cdot \mathbf{n}')} = \Gamma \Delta a' J \sqrt{(\mathbf{F}^{-\mathbf{1}} \cdot \mathbf{F}^{-\boldsymbol{T}}) : (\mathbf{n}' \otimes \mathbf{n}')} \quad (49)$$

With reference to the undeformed state, the stress power can be written as

$$\dot{W} = J\mathbf{T} : \mathbf{L} \quad (50)$$

For the Finger tensor **B** in affine deformation, the following equation holds true

$$\dot{\mathbf{B}} = \mathbf{L} \cdot \mathbf{B} + \mathbf{B} \cdot \mathbf{L}^{\boldsymbol{T}} \quad (51)$$

Since $\mathbf{T} : \mathbf{L} = (\mathbf{T} \cdot \mathbf{B}^{-\mathbf{1}}) : (\mathbf{B} \cdot \mathbf{L})$ and **T** and **B** are coaxial for isotropic materials, Eq. 50 can be rearranged into

$$\dot{W} = J\left(\mathbf{T}\cdot\mathbf{B}^{-1}\right):(\mathbf{B}\cdot\mathbf{L}) = \frac{J}{2}\left(\mathbf{T}\cdot\mathbf{B}^{-1}\right):(\mathbf{L}\cdot\mathbf{B}) + \frac{J}{2}\left(\mathbf{T}\cdot\mathbf{B}^{-1}\right):(\mathbf{B}\cdot\mathbf{L}^{T}) = \frac{J}{2}\mathbf{T}\cdot\mathbf{B}^{-1}:\dot{\mathbf{B}} \tag{52}$$

The interface is isotropically distributed and the phase size is considered infinitesimally small compared with the size scale of the deformation. Therefore, the stress tensor can be written as:

$$\mathbf{T} = \frac{2}{J}\frac{\partial W}{\partial \mathbf{B}}\cdot\mathbf{B} = \frac{2}{J}\frac{\partial U}{\partial \mathbf{B}}\cdot\mathbf{B}$$
$$\frac{\partial U}{\partial \mathbf{B}} = \frac{\partial(\Gamma\Delta a' J\sqrt{\left(\mathbf{F}^{-1}\cdot\mathbf{F}^{-T}\right):(\mathbf{n}'\otimes\mathbf{n}')})}{\partial \mathbf{B}} \tag{53}$$

Integrating above equation will lead to the stress tensor for a continuous interface, as shown below:

$$\mathbf{T} = \frac{2}{J}\frac{\partial U}{\partial \mathbf{B}}\cdot\mathbf{B} = \frac{2}{J}\frac{\partial\left(\left(\frac{\Gamma J}{V_0}\right)\int_{\psi_0}\sqrt{(\mathbf{F}^{-1}\cdot\mathbf{F}^{-T}):(\mathbf{n}'\otimes\mathbf{n}')}\,da'\right)}{\partial \mathbf{B}}\cdot\mathbf{B} \tag{54}$$

Since the integration is over a continuous interface which is isotropically distributed, so Eq. 54 can be rewritten as:

$$\mathbf{T} = \frac{2}{J}\frac{\partial U}{\partial \mathbf{B}} \cdot \mathbf{B} = \frac{2}{J}\frac{\partial \left((\frac{\Gamma J}{V_0}) \int_{\Psi_0} \sqrt{(\mathbf{F^{-T}} \cdot \mathbf{F^{-1}}) : (\mathbf{n'} \otimes \mathbf{n'})}\, da' \right)}{\partial \mathbf{B}} \cdot \mathbf{B}$$
$$= \frac{2}{J}\frac{\partial \left((\frac{\Gamma J}{V_0}) \int_{\psi_0} \sqrt{\mathbf{B}^{-1} : (\mathbf{n'} \otimes \mathbf{n'})}\, da' \right)}{\partial \mathbf{B}} \cdot \mathbf{B} \tag{55}$$

$\int_{\psi_0} \frac{\partial U}{\partial \mathbf{B}}$ can be further rearranged:

$$\int_{\psi_0} \frac{\partial U}{\partial \mathbf{B}} = \frac{\partial \left(\left(\frac{\Gamma J}{V_0} \right) \int_{\psi_0} \sqrt{\mathbf{B}^{-1} : (\mathbf{n'} \otimes \mathbf{n'})}\, da' \right)}{\partial \mathbf{B}}$$
$$= \frac{\Gamma}{2V_0 \sqrt{J^2 \mathbf{B}^{-1} : (\mathbf{n'} \otimes \mathbf{n'})}} \frac{\partial \left(\int_{\psi_0} J^2 \mathbf{B}^{-1} : (\mathbf{n'} \otimes \mathbf{n'})\, da' \right)}{\partial \mathbf{B}}$$
$$= \frac{\Gamma}{2V_0 \sqrt{J^2 \mathbf{B}^{-1} : (\mathbf{n'} \otimes \mathbf{n'})}} \left\{ \frac{\partial \int_{\psi_0} (\det(\mathbf{B})\, \mathbf{B}^{-1} : (\mathbf{n'} \otimes \mathbf{n'})) da'}{\partial \mathbf{B}} \right.$$
$$\left. + J^2 \frac{\partial \left(\int_{\psi_0} \mathbf{B}^{-1} : (\mathbf{n'} \otimes \mathbf{n'})\, da' \right)}{\partial \mathbf{B}} \right\} \tag{56}$$
$$= \frac{\Gamma \sqrt{\det(\mathbf{B})}}{2V_0} \int_{\psi_0} \left\{ \sqrt{\mathbf{B}^{-1} : (\mathbf{n'} \otimes \mathbf{n'})} \mathbf{B}^{-1} \right.$$
$$\left. - \frac{\mathbf{B}^{-1} \cdot (\mathbf{n'} \otimes \mathbf{n'}) \cdot \mathbf{B}^{-1}}{\sqrt{\mathbf{B}^{-1} : (\mathbf{n'} \otimes \mathbf{n'})}} \right\} da'$$

Substitution of above equation into Eq. 55 gives

$$\mathbf{T} = \frac{\Gamma}{V_0} \int_{\psi_0} \left\{ \sqrt{\mathbf{B}^{-1} : (\mathbf{n'} \otimes \mathbf{n'})} \mathbf{B}^{-1} - \frac{\mathbf{B}^{-1} \cdot (\mathbf{n'} \otimes \mathbf{n'}) \cdot \mathbf{B}^{-1}}{\sqrt{\mathbf{B}^{-1} : (\mathbf{n'} \otimes \mathbf{n'})}} \right\} da' \tag{57}$$

Combining above equation with $= \frac{2}{J}\frac{\partial U}{\partial \mathbf{B}} \cdot \mathbf{B}$, we can get the following equation

$$\begin{aligned}\mathbf{T} = \frac{2}{J}\frac{\partial U}{\partial \mathbf{B}} \cdot \mathbf{B} &= \frac{2}{J}\frac{\partial\left(\left(\frac{\Gamma J}{V_0}\right)\int_{\psi_0}\sqrt{\mathbf{B}^{-1}:(\mathbf{n}'\otimes\mathbf{n}')}\,da'\right)}{\partial \mathbf{B}} \cdot \mathbf{B} \\ &= \frac{\Gamma}{JV_0}\int_{\psi_0}\left\{\sqrt{\det(\mathbf{B})}\sqrt{\mathbf{B}^{-1}:(\mathbf{n}'\otimes\mathbf{n}')}\right. \\ &\left. - \sqrt{\det(\mathbf{B})}\frac{\mathbf{B}^{-1}\cdot(\mathbf{n}'\otimes\mathbf{n}')}{\sqrt{\mathbf{B}^{-1}:(\mathbf{n}'\otimes\mathbf{n}')}}\right\}da' \\ &= \frac{\Gamma}{JV_0}(a\mathbf{I} - \int_{\psi_0}\sqrt{\det(\mathbf{B})}\frac{\mathbf{B}^{-1}\cdot(\mathbf{n}'\otimes\mathbf{n}')}{\sqrt{\mathbf{B}^{-1}:(\mathbf{n}'\otimes\mathbf{n}')}}da')\end{aligned} \tag{58}$$

From Eq. 46, we can get

$$\mathbf{n}' = \frac{\mathbf{F}^{\boldsymbol{T}}\cdot\mathbf{n}}{|\mathbf{F}^{\boldsymbol{T}}\cdot\mathbf{n}|} \tag{59}$$

Substituting Eq. 45 and Eq. 59 into Eq. 58 and rearranging, we can obtain

$$\mathbf{T} = \frac{\Gamma}{V}\int_{\psi}[\mathbf{I} - \mathbf{n}\otimes\mathbf{n}]da, \tag{60}$$

which is the same equation with the one obtained via the derivation involving the right Cauchy-Green strain tensor **C**.

In summary, three types of equations of expressing the Cauchy stress tensor as a function of the Finger strain tensor have been derived:

Type 1 (Potential energy theory)

$$\mathbf{T} = \frac{2}{J}\frac{\partial U}{\partial \mathbf{B}} \cdot \mathbf{B} = \frac{2}{J}\frac{\partial \left((\frac{\Gamma J}{V_0}) \int_{\psi_0} \sqrt{(\mathbf{F^{-1}} \cdot \mathbf{F^{-T}}) : (\mathbf{n'} \otimes \mathbf{n'})}\, da' \right)}{\partial \mathbf{B}} \cdot \mathbf{B} \tag{61}$$

Type 2 (Cauchy stress tensor in terms of Langrangian parameters)

$$\mathbf{T} = \frac{\Gamma}{V_0}\int_{\psi_0} \left\{ \sqrt{\mathbf{B}^{-1} : (\mathbf{n'} \otimes \mathbf{n'})}\,\mathbf{B}^{-1} - \frac{\mathbf{B}^{-1} \cdot (\mathbf{n'} \otimes \mathbf{n'}) \cdot \mathbf{B}^{-1}}{\sqrt{\mathbf{B}^{-1} : (\mathbf{n'} \otimes \mathbf{n'})}} \right\} da' \tag{62}$$

Type 3 (Cauchy stress tensor in terms of Eulerian parameters)

$$\mathbf{T} = \frac{\Gamma}{V}\int_{\psi} [\mathbf{I} - \mathbf{n} \otimes \mathbf{n}]\, da \tag{63}$$

These three types of equations are equivalent. However, usually one is given information of the morphology at the initial state (represented by $\Delta\, a'$ and $\mathbf{n}'\mathbf{n}'$), and therefore Type 1 equation in such case will be more convenient for solving the Cauchy stress tensor. Type 1 is suitable especially when the type of deformation is given because $\frac{\partial U}{\partial \mathbf{B}}$ can be directly computed based on the unique form of the Finger strain tensor. Type 3 model is difficult to use because of the complexity in calculating the **nn** tensor.

Since the Finger strain tensor is always symmetric, it can be expressed with a spectral representation using its normalized eigenvectors, b^i, and the corresponding eigenvalues, k_i,

$$\mathbf{B} = \sum_i k_i \boldsymbol{b}^i \otimes \boldsymbol{b}^i \tag{64}$$

With $n_1 = sin\theta cos\varphi, n_2 = sin\theta sin\varphi, n_3 = cos\theta$, we can get

$$U = \frac{\Gamma J}{V_0}\int_{\psi_0}\sqrt{\mathbf{B}^{-1}:(\mathbf{n}'\otimes\mathbf{n}')}\,da' = \frac{\Gamma J}{V_0}\int_{\psi_0}\sqrt{k_1^{-1}n_1'^2 + k_2^{-1}n_2'^2 + k_3^{-1}n_3'^2}\,da'$$

$$= \frac{\Gamma J}{V_0}\int_{\psi_0}\sqrt{(k_1^{-1}-k_3^{-1})n_1'^2 + (k_2^{-1}-k_3^{-1})n_2'^2 + k_3^{-1}}\,da'$$

$$= \frac{A_0\Gamma}{4\pi V_0}\int_{\psi_0}\sqrt{k_1k_2k_3}\sqrt{(k_1^{-1}-k_3^{-1})n_1'^2 + (k_2^{-1}-k_3^{-1})n_2'^2 + k_3^{-1}}\,da' \tag{65}$$

$$= \frac{A_0\Gamma}{4\pi V_0}\int_{\psi_0}\sqrt{k_2k_3n_1'^2 + k_1k_3n_2'^2 + k_1k_2n_3'^2}\,da'$$

$$= \frac{A_0\Gamma}{4\pi V_0}\int_0^{\pi} -(d\cos\theta)\int_0^{2\pi}\sqrt{k_2k_3cos^2\varphi sin^2\theta + k_1k_3sin^2\varphi sin^2\theta + k_1k_2cos^2\theta}\,d\varphi$$

$$\mathbf{T} = \frac{2}{J}\frac{\partial U}{\partial \mathbf{B}}\cdot\mathbf{B} = \frac{2}{J}\cdot\left(\sum_{i=1}^{3}\frac{\partial U}{\partial k_i}\boldsymbol{b}^i\otimes\boldsymbol{b}^i\right)\cdot\mathbf{B}$$
$$= \frac{A_0\Gamma}{2\pi V_0 J}\cdot\left(\sum_{i=1}^{3}\frac{\partial g(k_1,k_2,k_3)}{\partial k_i}\boldsymbol{b}^i\otimes\boldsymbol{b}^i\right)\cdot\mathbf{B} \tag{66}$$

$g(k_1,k_2,k_3) = \int_{\psi_0}\sqrt{k_2k_3n_1'^2 + k_1k_3n_2'^2 + k_1k_2n_3'^2}\,da'$ is essentially the surface area of an ellipsoid with principle radii of $\sqrt{k_1}, \sqrt{k_2}, \sqrt{k_3}$. When closed-form solutions for ellipsoid surface area cannot be obtained using elementary functions, Yao [61] proposed to use the method of an approximation obtained by Xu et al [63].

$$g(k_1,k_2,k_3) \approx 4\pi\left(\frac{(k_1k_2)^{\varsigma/2} + (k_1k_3)^{\varsigma/2} + (k_2k_3)^{\varsigma/2}}{3}\right)^{1/\varsigma} \tag{67}$$

when $\varsigma = 1.6075$, the error is less than 1.061%. An approximation to the Cauchy stress tensor can be obtained by substituting above equation into Eq. 66.

$$\mathbf{T} = \frac{A_0\Gamma}{3V_0 J}\left(\frac{(k_1k_2)^{\varsigma/2} + (k_1k_3)^{\varsigma/2} + (k_2k_3)^{\varsigma/2}}{3}\right)^{1/\varsigma-1} \sum_{i=1}^{3}\sum_{j=1}^{3}(1 - \delta_{ij})(k_ik_j)^{\varsigma/2}\, \boldsymbol{b}^i \otimes \boldsymbol{b}^i \tag{68}$$

2.4 Model Testing

As already shown, the morphology development and rheological properties of polymer blends with complex interface during deformation can be treated via the kinematics of the Finger strain tensor. Besides, the Cauchy stress tensor can be written as a tensor derivative of the interfacial energy and expressed as a function of the Finger strain tensor. Here the accuracy of this theory will be tested using simple shear and uniaxial extension.

2.4.1 Uniaxial Elongation

The deformation gradient tensor of uniaxial elongation is

$$\mathbf{F} = \begin{pmatrix} \lambda & 0 & 0 \\ 0 & \lambda^{-1/2} & 0 \\ 0 & 0 & \lambda^{-1/2} \end{pmatrix} \tag{69}$$

in which λ is the stretch ratio. The Jacobian J for this tensor is equal to 1. The Finger strain tensor and its inverse are

$$\mathbf{B} = \begin{pmatrix} \lambda^2 & 0 & 0 \\ 0 & \lambda^{-1} & 0 \\ 0 & 0 & \lambda^{-1} \end{pmatrix} \; and \; \mathbf{B}^{-1} = \begin{pmatrix} \lambda^{-2} & 0 & 0 \\ 0 & \lambda & 0 \\ 0 & 0 & \lambda \end{pmatrix} \tag{70}$$

$$U = \frac{\Gamma J}{V_0}\int_{\psi_0}\sqrt{\mathbf{B}^{-1}:(\mathbf{n}'\otimes\mathbf{n}')}\,da' = \frac{\Gamma}{V_0}\int_{\psi_0}\sqrt{\lambda^{-2}n_1'^2+\lambda n_2'^2+\lambda n_3'^2}\,da'$$

$$= \frac{\Gamma}{V_0}\int_{\psi_0}\sqrt{\lambda+n_1'^2(\lambda^{-2}-\lambda)}\,da'$$

$$= \frac{A_0\Gamma}{4\pi V_0}\int_0^{\pi} -(d\cos\theta)\int_0^{2\pi}\sqrt{\lambda+cos^2\theta(\lambda^{-2}-\lambda)}\,d\varphi \qquad (71)$$

$$= \frac{A_0\Gamma}{\lambda V_0}\int_0^1\sqrt{\lambda^3-(\lambda^3-1)x^2}\,dx$$

$$= \frac{A_0\Gamma}{2V_0}\left[\frac{1}{\lambda}+\frac{\lambda^2 tan^{-1}(\sqrt{\lambda^3-1})}{\sqrt{\lambda^3-1}}\right]$$

We can get an analytical solution to **T** from Eq. 66, from which a first normal stress difference can be yielded,

$$T_{11}-T_{22} = \frac{A_0\Gamma}{4V_0}\left[\frac{(\lambda^5-4\lambda^2)tan^{-1}(\sqrt{\lambda^3-1})}{(\lambda^3-1)^{3/2}}+\frac{\lambda^2+2\lambda^{-1}}{\lambda^3-1}\right] \qquad (72)$$

An approximate solution using the ellipsoid surface area approximation can be obtained using Eq. 68

$$T_{11}-T_{22} = \frac{A_0\Gamma}{3V_0}\left(\frac{2\lambda^{\frac{\varsigma}{2}}+\lambda^{-\varsigma}}{3}\right)^{\frac{1-\varsigma}{\varsigma}}(\lambda^{\frac{\varsigma}{2}}-\lambda^{-\varsigma}) \qquad (73)$$

Here a solution obtained using the Doi-Ohta model is also given for comparison [40]:

$$T_{11} - T_{22} = \frac{A_0 \Gamma}{V_0} \frac{(\sqrt{\lambda} - \sqrt{\lambda^{-5}})}{\sqrt{3(2 + \lambda^{-3})}} \tag{74}$$

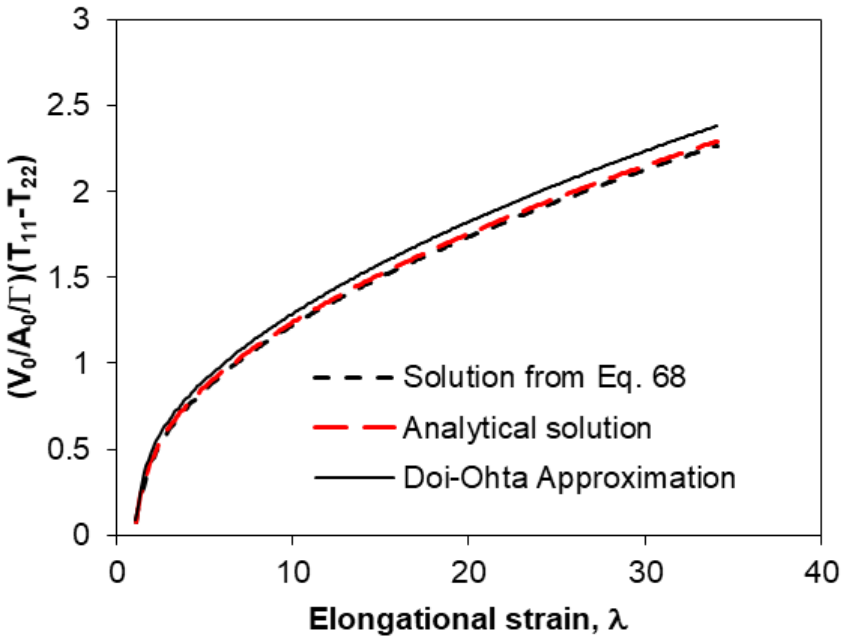

Figure 2-1 First normal stress difference as a function of elongational strain from three solutions for uniaxial elongation

Figure 2-1 shows the first normal stress difference plotted against uniaxial elongational strain for the above three solutions. The solution obtained by the ellipsoid surface area approximation is a better fit to the analytical solution than the Doi-Ohta model.

2.4.2 Simple Shear

As a further exercise, we test the theory using simple shear of an isotropic media with a deformation gradient tensor of

$$\mathbf{F} = \begin{pmatrix} 1 & \gamma & 0 \\ 0 & 1 & 0 \\ 0 & 0 & 1 \end{pmatrix} \tag{75}$$

in which γ is the shear strain. The Jacobian for this deformation tensor is equal to 1. The Finger strain tensor and its inverse are

$$\mathbf{B} = \begin{pmatrix} \gamma^2 + 1 & \gamma & 0 \\ \gamma & 1 & 0 \\ 0 & 0 & 1 \end{pmatrix} \; and \; \mathbf{B}^{-1} = \begin{pmatrix} 1 & -\gamma & 0 \\ -\gamma & \gamma^2 + 1 & 0 \\ 0 & 0 & 1 \end{pmatrix} \tag{76}$$

The eigenvalues of the Finger strain tensor are

$$k_1 = \frac{1}{2}\left(\gamma^2 - \gamma\sqrt{\gamma^2 + 4} + 2\right), k_2 = \frac{1}{2}\left(\gamma^2 + \gamma\sqrt{\gamma^2 + 4} + 2\right), k_3 = 1 \tag{77}$$

The corresponding eigenvectors are

$$b^1 = \frac{2}{\sqrt{2\gamma^2 - 2\gamma\sqrt{4 + \gamma^2} + 8}} \begin{pmatrix} \frac{1}{2}\left(\gamma - \sqrt{4 + \gamma^2}\right) \\ 1 \\ 0 \end{pmatrix}$$

$$b^2 = \frac{2}{\sqrt{2\gamma^2 + 2\gamma\sqrt{4 + \gamma^2} + 8}} \begin{pmatrix} \frac{1}{2}\left(\gamma + \sqrt{4 + \gamma^2}\right) \\ 1 \\ 0 \end{pmatrix} \tag{78}$$

$$b^3 = \begin{pmatrix} 0 \\ 0 \\ 1 \end{pmatrix}$$

By substituting above equations into the approximate equation for T, we can get the principle shear stress, which is plotted as a function of shear strain in Figure 2-2. The solution from the Doi-Ohta model is

$$T_{12} = \frac{A_0 \Gamma \gamma}{3V_0}\left(1 + \frac{\gamma^2}{3}\right)^{-1/2} \tag{79}$$

The exact integral from Eq. 22b can be written as:

$$T_{12} = \frac{A_0 \Gamma}{4\pi V_0}\int_0^{\pi}\int_0^{2\pi} \frac{\gamma sin\theta cos^2\theta - sin^2\theta cos\theta cos\varphi}{\sqrt{(1+\gamma^2 cos^2\theta) - (\gamma sin2\theta)cos\varphi}} d\varphi d\theta \tag{80}$$

from which the analytical asymtotes can be obtained:

$$T_{12} = \frac{A_0 \Gamma}{V_0}\begin{cases} \frac{4}{15}\gamma, \text{for } \gamma \ll 1 \\ 0.5, \quad \text{for } \gamma \gg 1 \end{cases} \tag{81}$$

For comparison, the Doi-Ohta solution and the analytical solution are both plotted in Figure 2-2 and we can see that the solution from the equation obtained with ellipsoid surface area approximation matches the analytical solution better than the Doi-Ohta model.

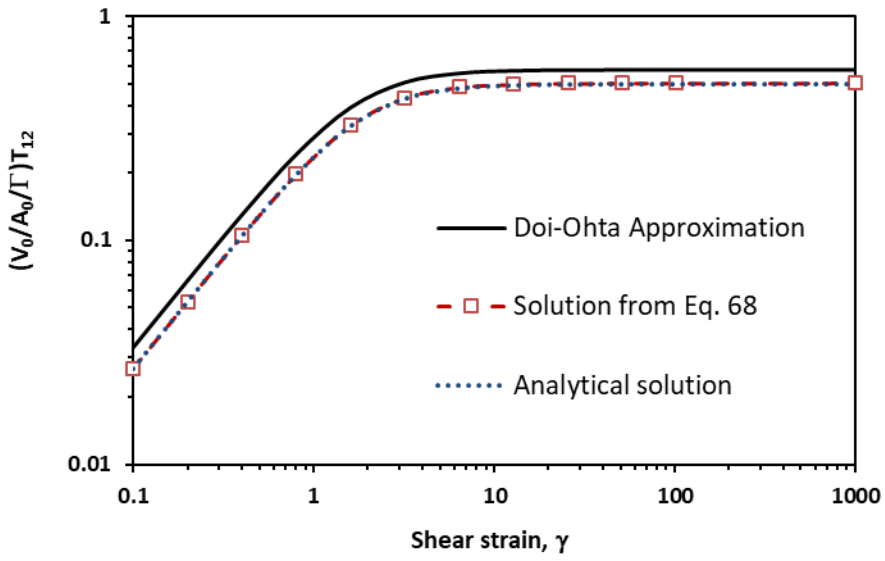

Figure 2-2 Shear stress as a function of shear strain from three solutions for simple shear

The prediction results of the obtained nearly closed-form solution for the uniaxial elongation model and the simple shear model indicate a good fitting to the exact solutions. Therefore, the relation between the Cauchy stress tensor and the interfacial conformation can be obtained by differentiating the interfacial energy with respect to the finger tensor, which provides another approach for analyzing the dynamics of complex interfaces.

2.5 Interfacial Orientation in Affine Deformation

2.5.1 Characterization of Interfacial Orientation via Interface Dynamics Based on the Finger Strain Tensor

In polymer processing, interfacial orientation is a parameter that is worthy of attention. When the polymer blend is being stretched, the interface will be oriented, which will make the polymer phases thinner and easier to break up during later-stage processing.

Therefore, the interfacial orientation is not helpful and even brings harm. From the result of Fu [64], the large interfacial orientation from the strong force field of injection molding caused layered structure and decreased the mechanical properties. It is already known that co-continuous morphology is important for overcoming the disadvantage of immiscibility and improving the mechanical properties of immiscible polymer blends. Therefore, we want to keep the co-continuous morphology in the final product as much as possible. Since a large interfacial orientation will make it difficult to retain the co-continuous morphology, knowledge about how to predict the interfacial orientation of the blends during different deformation processes will be helpful for the processing of polymer blends. Existing interface theories like the Doi-Ohta model and the Wetzel-Tucker method are not ideal for this purpose because of their computational complexity brought by the fourth-order tensor. In our study, it is shown that the interface dynamics can be approached via the Finger strain tensor which greatly simplified the calculation by avoiding the involvement of a fourth-order tensor. As already introduced, the complex interface in the deformed state can be represented by the surface of an ellipsoid with the Finger strain tensor as the characteristic tensor. Therefore, the problem of calculating interfacial orientation can be approached via the Finger strain tensor. Here a variable ϕ is defined to quantitatively represent the interfacial orientation degree:

$$\phi = B_{11} + B_{22} + B_{33} - 3 \tag{82}$$

in which B_{11}, B_{22}, B_{33} are the diagonal terms of the Finger strain tensor. With the variable ϕ, it is convenient to quantize and compare the interfacial orientation degree in various deformation fields. When relaxation is not considered and it is assumed to be affine

deformation or conformal deformation, the change of interfacial orientation degree with the strain in different deformation fields can be obtained based on the Finger strain tensor.

2.5.2 Quantification of Interfacial Orientation with the Self-Defined Variable ϕ

2.5.2.1 Uniaxial Elongation

Uniaxial elongation is a deformation that is common in many processes. Here we will check how the interfacial orientation degree ϕ changes with time during a uniaxial elongation. The velocity gradient of uniaxial elongation is

$$\mathbf{L}(t) = \begin{pmatrix} \dot{\varepsilon}_0 & 0 & 0 \\ 0 & -\frac{1}{2}\dot{\varepsilon}_0 & 0 \\ 0 & 0 & -\frac{1}{2}\dot{\varepsilon}_0 \end{pmatrix} \tag{83}$$

in which $\dot{\varepsilon}_0$ is a constant stretch rate. Therefore, the resultant deformation gradient tensor and Finger strain tensor are respectively

$$\mathbf{F}(t) = \begin{pmatrix} e^{\dot{\varepsilon}_0 t} & 0 & 0 \\ 0 & e^{-\frac{1}{2}\dot{\varepsilon}_0 t} & 0 \\ 0 & 0 & e^{-\frac{1}{2}\dot{\varepsilon}_0 t} \end{pmatrix} \text{ and } \mathbf{B}(t) = \begin{pmatrix} e^{2\dot{\varepsilon}_0 t} & 0 & 0 \\ 0 & e^{-\dot{\varepsilon}_0 t} & 0 \\ 0 & 0 & e^{-\dot{\varepsilon}_0 t} \end{pmatrix} \tag{84}$$

A characteristic relaxation time, ξ, is defined according to the mechanics of the ellipsoidal relaxation process

$$\xi = \frac{\eta \hat{l}}{\sigma} = \frac{3\eta}{A_0 \Gamma} \tag{85}$$

in which the unit length $\hat{l}$ can be considered as the representative dimension of the ellipsoid with **B** as the characteristic tensor.

Reduced time $\tilde{t} = \frac{t}{\xi}$ is used to normalize the time scale. The interfacial orientation degree ϕ can be expressed with

$$\phi = e^{2\dot{\varepsilon}_0 t} + 2e^{-\dot{\varepsilon}_0 t} - 3 = e^{2\dot{\varepsilon}_0 \xi \tilde{t}} + 2e^{-\dot{\varepsilon}_0 \xi \tilde{t}} - 3 \tag{86}$$

The interfacial orientation degree with reduced time relationship under different stretch rate in uniaxial elongational flow is plotted in Figure 2-3. It can be seen that the interfacial orientation degree ϕ increases with time and when $\dot{\varepsilon}_0$ increases, the value of ϕ and the rate of increase of ϕ both increase.

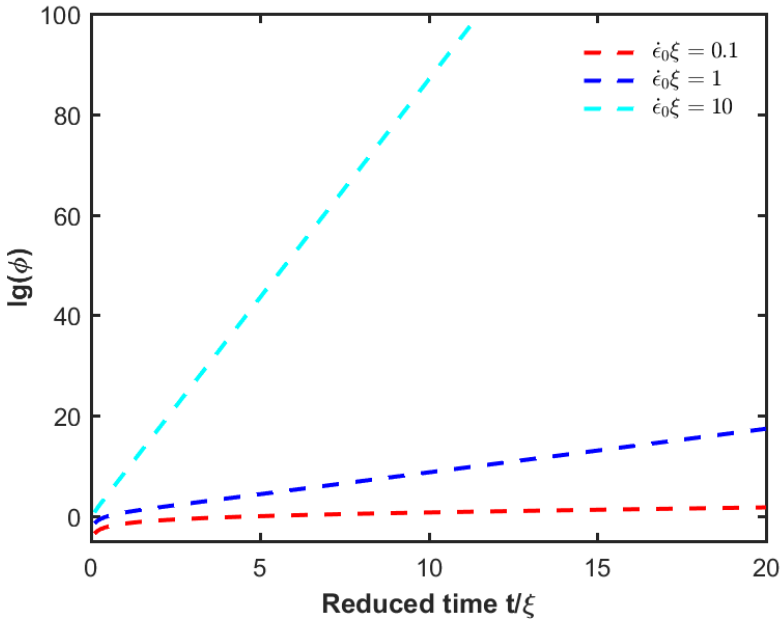

Figure 2-3 Interfacial orientation degree as a function of reduced time for uniaxial elongational flow. A base-10 logarithmic scale is used for the Y axis.

2.5.2.2 Biaxial Extension

The change of interfacial orientation degree ϕ during a biaxial extension is calculated here. The velocity gradient of biaxial extension is

$$\mathbf{L}(t) = \begin{pmatrix} \dot{\varepsilon}_0 & 0 & 0 \\ 0 & \dot{\varepsilon}_0 & 0 \\ 0 & 0 & -2\dot{\varepsilon}_0 \end{pmatrix} \tag{87}$$

The deformation tensor and the Finger strain tensor are calculated accordingly to be

$$\mathbf{F}(t) = \begin{pmatrix} e^{\dot{\varepsilon}_0 t} & 0 & 0 \\ 0 & e^{\dot{\varepsilon}_0 t} & 0 \\ 0 & 0 & e^{-2\dot{\varepsilon}_0 t} \end{pmatrix} \text{ and } \mathbf{B}(t) = \begin{pmatrix} e^{2\dot{\varepsilon}_0 t} & 0 & 0 \\ 0 & e^{2\dot{\varepsilon}_0 t} & 0 \\ 0 & 0 & e^{-4\dot{\varepsilon}_0 t} \end{pmatrix} \tag{88}$$

The interfacial orientation degree ϕ is

$$\phi = 2e^{2\dot{\varepsilon}_0 t} + e^{-4\dot{\varepsilon}_0 t} - 3 = 2e^{2\dot{\varepsilon}_0 \xi \tilde{t}} + e^{-4\dot{\varepsilon}_0 \xi \tilde{t}} - 3 \tag{89}$$

whose change with reduced time is shown in Figure 2-4. It can be seen that ϕ has a larger value and increases faster when the stretch rate increases.

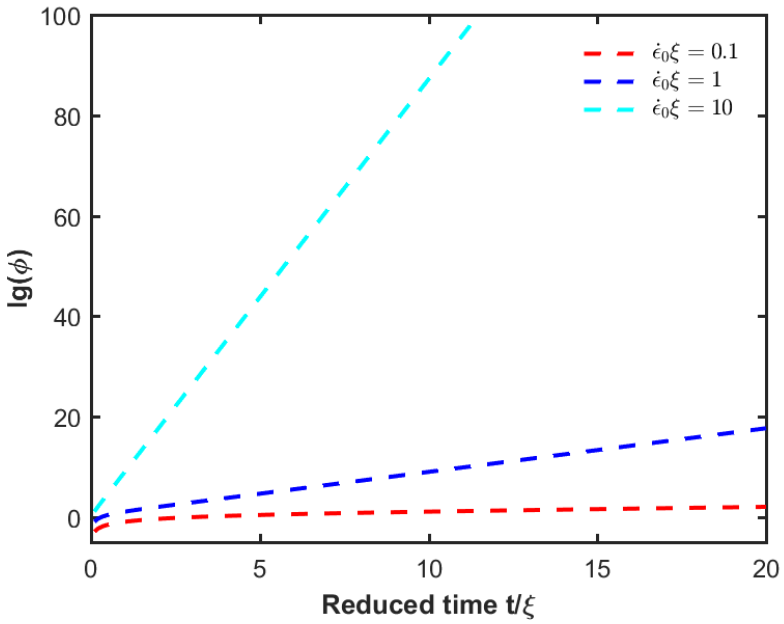

Figure 2-4 Interfacial orientation degree as a function of reduced time for biaxial extensional flow. A base-10 logarithmic scale is used for the Y axis.

2.5.2.3 Planar Elongational Flow

Similarly, we can calculate the interfacial orientation degree ϕ for the planar elongational flow. The velocity gradient, deformation tensor and the Finger strain tensor for planar elongational flow are shown below.

$$\mathbf{L}(t) = \begin{pmatrix} \dot{\varepsilon}_0 & 0 & 0 \\ 0 & 0 & 0 \\ 0 & 0 & -\dot{\varepsilon}_0 \end{pmatrix} \tag{90}$$

$$\mathbf{F}(t) = \begin{pmatrix} e^{\dot{\varepsilon}_0 t} & 0 & 0 \\ 0 & 1 & 0 \\ 0 & 0 & e^{-\dot{\varepsilon}_0 t} \end{pmatrix}, \quad \mathbf{B}(t) = \begin{pmatrix} e^{2\dot{\varepsilon}_0 t} & 0 & 0 \\ 0 & 1 & 0 \\ 0 & 0 & e^{-2\dot{\varepsilon}_0 t} \end{pmatrix} \tag{91}$$

The interfacial orientation degree ϕ is

$$\phi = e^{2\dot{\varepsilon}_0 t} + e^{-2\dot{\varepsilon}_0 t} - 2 = e^{2\dot{\varepsilon}_0 \xi \tilde{t}} + e^{-2\dot{\varepsilon}_0 \xi \tilde{t}} - 2 \tag{92}$$

The change of ϕ with reduced time in planar elongational flow is shown in Figure 2-5, which shows a similar trend with the biaxial extensional field.

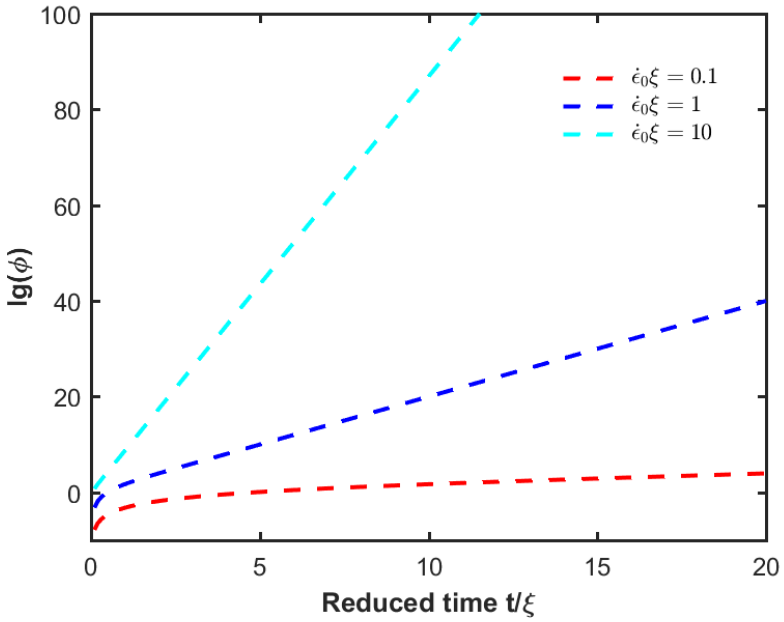

Figure 2-5 Interfacial orientation degree as a function of reduced time for planar elongational flow. A base-10 logarithmic scale is used for the Y axis.

2.5.2.4 Simple Shear

Finally, we calculate the interfacial orientation degree ϕ for simple shear. The velocity gradient, deformation tensor and the Finger strain tensor for simple shear are shown below.

$$\mathbf{L}(t) = \begin{pmatrix} 0 & \gamma & 0 \\ 0 & 0 & 0 \\ 0 & 0 & 0 \end{pmatrix} \tag{93}$$

$$\mathbf{F}(t) = \begin{pmatrix} 1 & \gamma & 0 \\ 0 & 1 & 0 \\ 0 & 0 & 1 \end{pmatrix}, \qquad \mathbf{B}(t) = \begin{pmatrix} \gamma^2 + 1 & r & 0 \\ r & 1 & 0 \\ 0 & 0 & 1 \end{pmatrix} \tag{94}$$

The interfacial orientation degree ϕ is

$$\phi = \gamma^2 = \gamma^2 \tilde{\xi}^2 \tilde{t}^2 \tag{95}$$

Figure 2-6 shows the change of ϕ with reduced time in different shear rate. In a deformation field of simple shear, the increase of interfacial orientation degree is much slower than it is in uniaxial elongations and biaxial extensions. Therefore, when processing polymer blends that need to have small interfacial orientation degree, one might consider decreasing the time that the blend spent in elongational deformation fields.

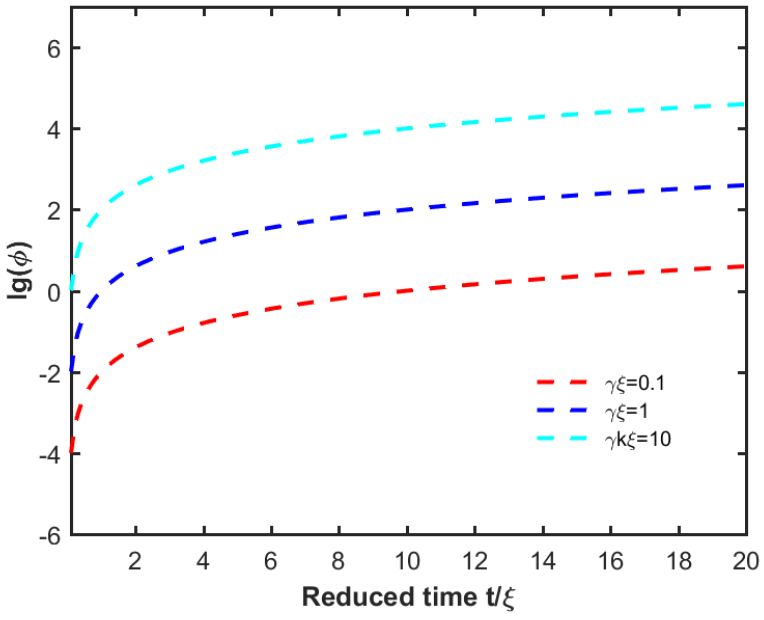

Figure 2-6 Interfacial orientation degree as a function of reduced time for simple shear flow. A base-10 logarithmic scale is used for the Y axis.

2.6 Conclusions

The presence of an implicit interface makes it complex to analyze the dynamics and rheology of blends. In this chapter, three equivalent solutions to the Cauchy stress tensor are derived based on the Finger strain tensor. The extra stress tensor is directly proportional to the interface tensor, which describes the dynamics of complex interfaces. By exploring the analytical nature of the tensor derivative of the interfacial energy, our theory provides a convenient method for treating the dynamics of complex interfaces by hyperelastic finite deformation. Similar with the method of deriving the stress tensor based on the right Cauchy-Green strain tensor, this method is realized by elementary algebraic and matrix operations and avoids the complex calculation introduced by the involvement of a fourth-order tensor. In addition, the use of the Finger strain tensor brings advantages that the right Cauchy-Green strain tensor does not do. The Finger strain tensor is more maneuverable and the large knowledge base developed in nonlinear viscoelasticity can be used for assisting with the interface problem and rheology. The use of the Finger strain tensor also provides an easy method of studying the interface dynamics using the ellipsoidal surface approximation. For some complex interfaces, the material parameters in the constitutive model are difficult to be written as elementary functions. The ellipsoidal surface approximation can help resolve the tensor derivative $\partial g/\partial \mathbf{B}$ into elementary functions. Two case studies are used to show that the theory derived based on the Finger strain tensor with an approximate ellipsoid area surface gives a better fitting to the analytical solution than the solution from the Doi-Ohta model. Moreover, with the Finger tensor approach and the ellipsoidal equivalency, we can represent the interfacial orientation degree with an

expression of the Finger strain tensor and calculate their values in different deformation fields, which might be helpful for polymer blends processing.

3. INVESTIGATION OF THE INTERFACIAL ORIENTATION OF IMMISCIBLE POLYMER BLENDS

3.1 Introduction

The discussion in Chapter 2 does not consider the relaxation of interfaces, which is not suitable for realistic polymer processing because the interfaces in viscoelastic polymer blends are subject to interfacial relaxation. In this chapter, interfacial orientation with the consideration of the relaxation effects will be calculated and compared with the results without relaxation.

As already introduced in Chapter 2, the interfacial orientation degree can be expressed via the Finger strain tensor **B**. To deal with the relaxation effects, the total **B** can be split into two parts [62]: $\mathbf{B}_e$ and $\mathbf{B}_d$. One part is kept ($\mathbf{B}_e$) and the other is dissipated ($\mathbf{B}_d$). We need to use the kept/memorized strain $\mathbf{B}_e$ instead of **B** for representing the actual interfacial orientation. Therefore, the interfacial orientation degree for interfaces with relaxation effects can be described as

$$\phi = \mathrm{B}_{e11} + \mathrm{B}_{e22} + \mathrm{B}_{e33} - 3 \tag{96}$$

To calculate the interfacial orientation degree, we need to obtain $\mathbf{B}_e$, for which an energy balance method introduced by Yao [62] will be used. From the properties of Finger strain tensor, we can get

$$\dot{\mathbf{B}}_e = \mathbf{B}_e \cdot (\mathbf{L} + \mathbf{L}_d)^T + (\mathbf{L} + \mathbf{L}_d) \cdot \mathbf{B}_e \tag{97}$$

in which $\mathbf{L}_d$ is the velocity gradient corresponding to the dissipated energy. From Eq. 97. we can get the following expressions,

$$\dot{\mathbf{B}}_e - \mathbf{B}_e \cdot \mathbf{L} - \mathbf{L} \cdot \mathbf{B}_e - \mathbf{B}_e \cdot \mathbf{L}_d - \mathbf{L}_d \cdot \mathbf{B}_e = 0 \tag{98}$$

$$\overset{\nabla}{\mathbf{B}}_e - \mathbf{B}_e \cdot \mathbf{L}_d^T - \mathbf{L}_d \cdot \mathbf{B}_e = 0 \tag{99}$$

The rates of decrease of stored elastic energy $-\dot{W}_e$ and heat generation $\dot{Q}$ are considered equivalent,

$$-\dot{W}_e = \dot{Q}$$

$$\dot{W} = \frac{J}{2}(\mathbf{T} \cdot \mathbf{B}^{-1}) : \dot{\mathbf{B}} \tag{100}$$

$$\dot{Q} = \eta(\mathbf{L}_d + \mathbf{L}_d{}^T) : \mathbf{L}_d$$

Combining the above three equations, we can get

$$-\frac{J}{2}(\mathbf{T} \cdot \mathbf{B}_e^{-1}) : \dot{\mathbf{B}}_e = J\left[\eta\left(\mathbf{L}_d + \mathbf{L}_d{}^T\right) + \nu(\mathrm{tr}\mathbf{L}_d)\mathbf{I}\right] : \mathbf{L}_d$$

$$-[\mathbf{T} - \frac{1}{3}(\mathbf{trT})\mathbf{I}] : \mathbf{L}_d = 2\eta\mathbf{L}_d \cdot \mathbf{L}_d \tag{101}$$

from which we can get

$$\mathbf{L}_d = -\frac{\mathbf{T} - \frac{1}{3}(\mathrm{tr}\mathbf{T})\mathbf{I}}{2\eta} \tag{102}$$

From Eq. 66, we can get

$$\mathbf{T} = \frac{A_0 \Gamma}{2\pi J} \frac{\partial g_e}{\partial \mathbf{B}_e} \cdot \mathbf{B}_e \tag{103}$$

in which g_e is the surface area of the ellipsoid with a characteristic tensor of $\mathbf{B}_e$.

Combining Eq. 102 and 103, we get

$$\mathbf{L}_d = \frac{A_0 g_e \Gamma}{12\pi J\eta}\mathbf{I} - \frac{A_0 \Gamma}{4\pi J\eta} \frac{\partial g_e}{\partial \mathbf{B}_e} \cdot \mathbf{B}_e \tag{104}$$

Substituting the above equation into Eq. 99, we get an equation for $\mathbf{B}_e$

$$\overset{\nabla}{\mathbf{B}}_e - \frac{A_0 g_e \Gamma}{6\pi J\eta}\mathbf{B}_e + \frac{A_0 \Gamma}{2\pi J\eta} \frac{\partial g_e}{\partial \mathbf{B}_e} \cdot \mathbf{B}_e \cdot \mathbf{B}_e = 0 \tag{105}$$

With this evolution equation for B_e, we can calculate the interfacial orientation degree with relaxation effects in different deformation fields, which will be demonstrated in the following sections.

3.2 Calculation of Interfacial Orientation Degree with Relaxation Effects Considered

3.2.1 Interfacial Orientation Degree in Uniaxial Elongation Deformation Field

In Chapter 2, the interfacial orientation degree in affine deformation without relaxation effects has been calculated. Here we will calculate the interfacial orientation degree with relaxation effects considered. The retained strain tensor can be expressed as

$$\mathbf{B}_e = \begin{pmatrix} {\lambda_e}^2 & 0 & 0 \\ 0 & {\lambda_e}^{-1} & 0 \\ 0 & 0 & {\lambda_e}^{-1} \end{pmatrix} \tag{106}$$

in which λ_e is used to differentiate from the initial stretch ratio.

$$\dot{\mathbf{B}}_e = \begin{pmatrix} 2\lambda_e\dot{\lambda_e} & 0 & 0 \\ 0 & -{\lambda_e}^{-2}\dot{\lambda_e} & 0 \\ 0 & 0 & -{\lambda_e}^{-2}\dot{\lambda_e} \end{pmatrix} \tag{107}$$

$$\frac{\partial g_e}{\partial \mathbf{B}_e} \cdot \mathbf{B}_e = \frac{2\pi}{3}\left(\frac{g_e}{4\pi}\right)^{1-\varsigma} \sum_{i=1}^{3}\sum_{j=1}^{3}(1-\delta_{ij})(k_i k_j)^{\varsigma/2}\mathbf{b}^i \otimes \mathbf{b}^i \tag{108}$$

$$k_i = \lambda_i^2$$

Substituting the above equations into Eq. 105, we can get

$$\dot{\lambda_e} - \dot{\varepsilon}_0\lambda_e - \frac{A_0 g_e \Gamma}{12\pi\eta}\lambda_e + \frac{A_0\Gamma}{3\eta}\left(\frac{g_e}{4\pi}\right)^{1-\varsigma}{\lambda_e}^{\frac{\varsigma}{2}+1} = 0 \tag{109}$$

The same method is used for obtaining the surface area,

$$g(\lambda_1,\lambda_2,\lambda_3) \approx 4\pi\left(\frac{(\lambda_1\lambda_2)^\varsigma + (\lambda_1\lambda_3)^\varsigma + (\lambda_2\lambda_3)^\varsigma}{3}\right)^{1/\varsigma} \tag{110}$$

Therefore, we can get the approximate surface area as

$$g_e \approx 4\pi(\frac{2{\lambda_e}^{\varsigma/2} + {\lambda_e}^{-\varsigma}}{3})^{1/\varsigma} \tag{111}$$

Substituting the above equation into Eq. 109, we can get the evolution equation of λ_e

$$\frac{d\lambda_e}{dt} = \dot{\varepsilon}_0\lambda_e - \frac{2A_0\Gamma}{3\eta}\left(\frac{2\lambda_e^{\frac{\varsigma}{2}} + \lambda_e^{-\varsigma}}{3}\right)^{\frac{1}{\varsigma}} + \frac{A_0\Gamma}{3\eta}\left(\frac{2\lambda_e^{\frac{\varsigma}{2}} + \lambda_e^{-\varsigma}}{3}\right)^{\frac{1-\varsigma}{\varsigma}}\left(\lambda_e^{\frac{\varsigma}{2}-1} + \lambda_e^{-\varsigma-1}\right) \tag{112}$$

Then we can get the evolution equation of λ_e with the reduced time $\tilde{t}$

$$\frac{d\lambda_e}{d\tilde{t}} = \xi\dot{\epsilon}\lambda_e - 2\left(\frac{2\lambda_e^{\frac{\varsigma}{2}} + \lambda_e^{-\varsigma}}{3}\right)^{\frac{1}{\varsigma}} + \left(\frac{2\lambda_e^{\frac{\varsigma}{2}} + \lambda_e^{-\varsigma}}{3}\right)^{\frac{1-\varsigma}{\varsigma}}\left(\lambda_e^{\frac{\varsigma}{2}-1} + \lambda_e^{-\varsigma-1}\right) \tag{113}$$

The interfacial orientation degree with relaxation effects considered can be written by

$$\phi = \mathrm{B}_{e11} + \mathrm{B}_{e22} + \mathrm{B}_{e33} - 3 = {\lambda_e}^2 + 2{\lambda_e}^{-1} - 3 \tag{114}$$

Since ϕ can be expressed with λ_e, we can know the change of ϕ with reduced time from Eq. 113, which is shown in Figure 3-1. It shows that the interfacial orientation degree of viscoelastic polymer blends with relaxation effects under uniaxial elongation field has the same trend for different $\dot{\varepsilon}_0$. At the beginning, the interfacial orientation degree increases with time, and then will stabilize at a time scale of orders of ξ.

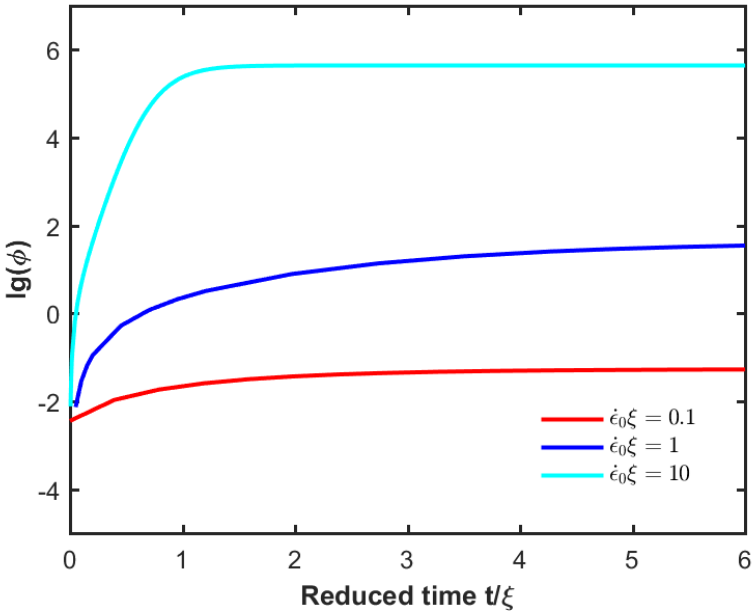

Figure 3-1 Interfacial orientation degree as a function of reduced time for uniaxial elongational flow with relaxation effects considered. A base-10 logarithmic scale is used for the Y axis.

3.2.2 Interfacial Orientation Degree in Biaxial Extension Deformation Field

With relaxation effects considered, the change of interfacial orientation degree ϕ during a biaxial extension is calculated here. The memorized Finger strain tensor are

$$\mathbf{B}_e = \begin{pmatrix} {\lambda_e}^2 & 0 & 0 \\ 0 & {\lambda_e}^2 & 0 \\ 0 & 0 & {\lambda_e}^{-4} \end{pmatrix} \tag{115}$$

$$\dot{\mathbf{B}}_e = \begin{pmatrix} 2\lambda_e\dot{\lambda_e} & 0 & 0 \\ 0 & 2\lambda_e\dot{\lambda_e} & 0 \\ 0 & 0 & -4{\lambda_e}^{-5}\dot{\lambda_e} \end{pmatrix} \tag{116}$$

The surface area is approximately

$$g_e \approx 4\pi\left(\frac{{\lambda_e}^{2\varsigma} + 2{\lambda_e}^{-\varsigma}}{3}\right)^{1/\varsigma} \tag{117}$$

$$\frac{\partial g_e}{\partial \mathbf{B}_e} \cdot \mathbf{B}_e = \frac{2\pi}{3}\left(\frac{g_e}{4\pi}\right)^{1-\varsigma} \begin{pmatrix} {\lambda_e}^{2\varsigma+2} + {\lambda_e}^{-\varsigma+2} & 0 & 0 \\ 0 & {\lambda_e}^{2\varsigma+2} + {\lambda_e}^{-\varsigma+2} & 0 \\ 0 & 0 & 2{\lambda_e}^{-\varsigma-4} \end{pmatrix} \tag{118}$$

Combining above equations with Eq. 105, we can get the evolution equation of λ_e with time

$$\frac{d\lambda_e}{dt} = \dot{\epsilon}\lambda_e + \frac{A_0\Gamma}{18\eta}\left(\frac{\lambda_e^{2\varsigma} + 2\lambda_e^{-\varsigma}}{3}\right)^{\frac{1-\varsigma}{\varsigma}}\left(\lambda_e^{-\varsigma+1} + \lambda_e^{2\varsigma+1}\right) \tag{119}$$

After normalizing the time with characteristic relaxation time, we can obtain

$$\frac{d\lambda_e}{d\tilde{t}} = \xi\dot{\epsilon}\lambda_e + \frac{1}{6}\left(\frac{\lambda_e^{2\varsigma} + 2\lambda_e^{-\varsigma}}{3}\right)^{\frac{1-\varsigma}{\varsigma}}\left(\lambda_e^{-\varsigma+1} + \lambda_e^{2\varsigma+1}\right) \tag{120}$$

The interfacial orientation degree with relaxation effects considered can be expressed as

$$\phi = \mathrm{B}_{e11} + \mathrm{B}_{e22} + \mathrm{B}_{e33} - 3 = 2{\lambda_e}^2 + {\lambda_e}^{-4} - 3 \tag{121}$$

With Eq. 120 and 121, we can know the change of ϕ with reduced time for viscoelastic polymer blends subjected to biaxial extension deformation field, which is shown in Figure 3-2.

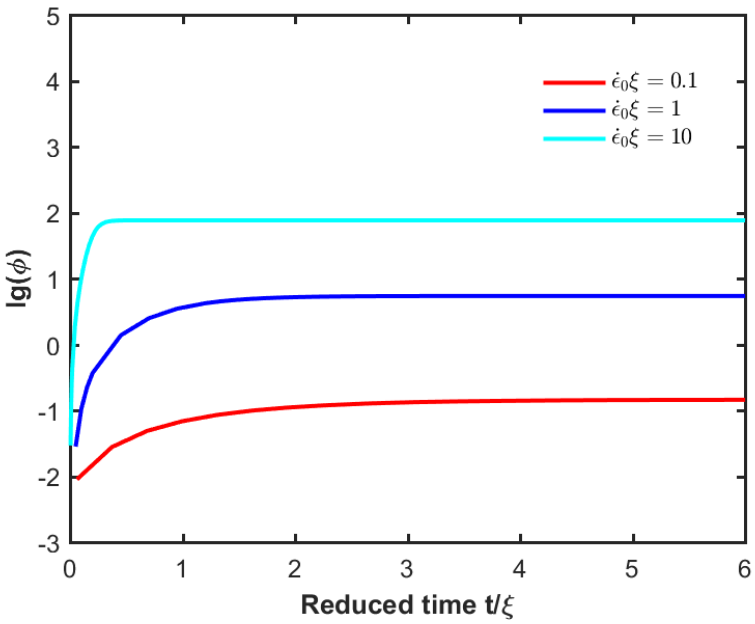

Figure 3-2 Interfacial orientation degree as a function of reduced time for biaxial extensional flow with relaxation effects considered. A base-10 logarithmic scale is used for the Y axis.

Similar with the interfacial orientation degree of polymer blends in uniaxial elongation field, the interfacial orientation degree in biaxial extension field also increases with time at first and then stabilizes at a time scale of orders of ξ. However, the interfacial orientation degree in biaxial extension field is smaller and stabilizes earlier than that in uniaxial elongation field.

3.2.3 Interfacial Orientation Degree in Planar Elongation Deformation Field

Similarly, we can calculate the interfacial orientation degree ϕ with relaxation effects for the planar elongational flow. The actual Finger strain tensor for planar elongational flow are shown below.

$$\mathbf{B}_e = \begin{pmatrix} {\lambda_e}^2 & 0 & 0 \\ 0 & 1 & 0 \\ 0 & 0 & {\lambda_e}^{-2} \end{pmatrix} \tag{122}$$

$$\dot{\mathbf{B}}_e = \begin{pmatrix} 2\lambda_e\dot{\lambda_e} & 0 & 0 \\ 0 & 0 & 0 \\ 0 & 0 & -2{\lambda_e}^{-3}\dot{\lambda_e} \end{pmatrix} \tag{123}$$

The surface area is approximately

$$g_e \approx 4\pi\left(\frac{{\lambda_e}^{\varsigma} + 1 + {\lambda_e}^{-\varsigma}}{3}\right)^{1/\varsigma} \tag{124}$$

$$\frac{\partial g_e}{\partial \mathbf{B}_e} \cdot \mathbf{B}_e = \frac{2\pi}{3}\left(\frac{g_e}{4\pi}\right)^{1-\varsigma} \begin{pmatrix} {\lambda_e}^{\varsigma+2} + {\lambda_e}^2 & 0 & 0 \\ 0 & {\lambda_e}^{\varsigma} + {\lambda_e}^{-\varsigma} & 0 \\ 0 & 0 & {\lambda_e}^{-\varsigma-2} + {\lambda_e}^{-2} \end{pmatrix} \tag{125}$$

Substituting above equations into Eq. 105, we can get the evolution equation of λ_e with time

$$\frac{d\lambda_e}{dt} = \dot{\epsilon}\lambda_e + \frac{A_0\Gamma}{3\eta}\left(\frac{\lambda_e^{\varsigma} + \lambda_e^{-\varsigma} + 1}{3}\right)^{\frac{1-\varsigma}{\varsigma}}\left(\frac{1}{3}\lambda_e^{-\varsigma+1} - \frac{1}{6}\lambda_e - \frac{1}{6}\lambda_e^{\varsigma+1}\right) \tag{126}$$

The evolution equation of λ_e with the reduced time is

$$\frac{d\lambda_e}{d\tilde{t}} = \xi\dot{\epsilon}\lambda_e + \left(\frac{\lambda_e^{\varsigma} + \lambda_e^{-\varsigma} + 1}{3}\right)^{\frac{1-\varsigma}{\varsigma}}\left(\frac{1}{3}\lambda_e^{-\varsigma+1} - \frac{1}{6}\lambda_e - \frac{1}{6}\lambda_e^{\varsigma+1}\right) \tag{127}$$

The interfacial orientation degree with relaxation effects considered can be expressed with

$$\phi = B_{e11} + B_{e22} + B_{e33} - 3 = {\lambda_e}^2 + {\lambda_e}^{-2} - 2 \quad (128)$$

From Eq. 127 and 128, we can obtain the change of ϕ with reduced time for viscoelastic polymer blends subjected to planar elongational flow, as shown in Figure 3-3. It can be seen that the interfacial orientation degree of polymer blends in planar elongational flow has the similar trend of first increasing with time at first and then stabilizing at a time scale of orders of ξ.

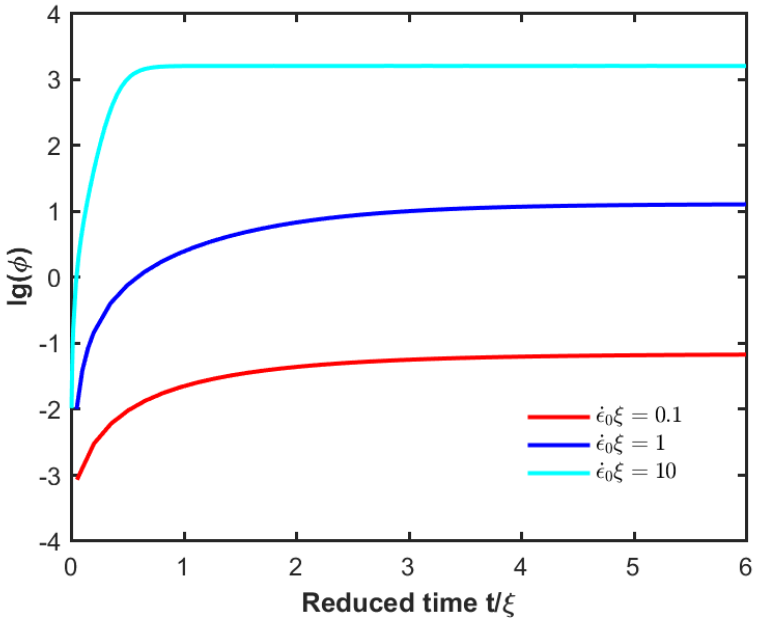

Figure 3-3 Interfacial orientation degree as a function of reduced time for planar elongational flow with relaxation effects considered. A base-10 logarithmic scale is used for the Y axis.

3.2.4 Interfacial Orientation Degree in Simple Shear Deformation Field

With a simple shear with shear strain γ applied to the viscoelastic media, the total strain applied to the blend is

$$\mathbf{B}(t) = \begin{pmatrix} \gamma^2 t^2 + 1 & \gamma t & 0 \\ \gamma t & 1 & 0 \\ 0 & 0 & 1 \end{pmatrix} \tag{129}$$

To express the memorized strain, we introduce a temporary variable l_e, which refers to the part of (γt) that is kept. The memorized strain can be written as

$$\mathbf{B}_e = \begin{pmatrix} 1 + {l_e}^2 & l_e & 0 \\ l_e & 1 & 0 \\ 0 & 0 & 1 \end{pmatrix} \tag{130}$$

The strain rate is

$$\dot{\mathbf{B}}_e = \begin{pmatrix} 2 l_e \dot{l_e} & \dot{l_e} & 0 \\ \dot{l_e} & 0 & 0 \\ 0 & 0 & 0 \end{pmatrix} \tag{131}$$

The three eigenvalues of the memorized strain tensor $\lambda_1^2,\ \lambda_2^2,\ \lambda_3^2$ are respectively

$$\lambda_1^2 = \frac{1}{2}(l_e^2 - l_e\sqrt{l_e^2 + 4} + 2)$$

$$\lambda_2^2 = \frac{1}{2}(l_e^2 + l_e\sqrt{l_e^2 + 4} + 2) \tag{132}$$

$$\lambda_3^2 = 1$$

The three eigenvectors of the memorized strain tensor $\mathbf{v}_1, \mathbf{v}_2, \mathbf{v}_3$ are respectively

$$\mathbf{v}_1 = \frac{2}{\sqrt{2l_e^2 - 2l_e\sqrt{l_e^2+4}+8}}\begin{pmatrix}\frac{l_e-\sqrt{l_e^2+4}}{2}\\1\\0\end{pmatrix}$$

$$\mathbf{v}_2 = \frac{2}{\sqrt{2l_e^2 + 2l_e\sqrt{l_e^2+4}+8}}\begin{pmatrix}\frac{l_e+\sqrt{l_e^2+4}}{2}\\1\\0\end{pmatrix} \tag{133}$$

$$\mathbf{v}_3 = \begin{pmatrix}0\\0\\1\end{pmatrix}$$

The surface area is approximately

$$g_e(\lambda_1,\lambda_2,\lambda_3) \approx 4\pi\left(\frac{(\lambda_1\lambda_2)^\varsigma + (\lambda_1\lambda_3)^\varsigma + (\lambda_2\lambda_3)^\varsigma}{3}\right)^{1/\varsigma} \tag{134}$$

$$\frac{\partial g_e}{\partial \mathbf{B}_e} = \sum_{i=1}^{3}\frac{1}{2\lambda_i}\frac{\partial g_e}{\partial \lambda_i}\mathbf{b}^i\otimes\mathbf{b}^i = 4\pi\sum_{i=1}^{3}\frac{1}{2\lambda_i}\frac{\partial\left(\frac{(\lambda_1\lambda_2)^\varsigma + (\lambda_1\lambda_3)^\varsigma + (\lambda_2\lambda_3)^\varsigma}{3}\right)^{\frac{1}{\varsigma}}}{\partial\lambda_i}\mathbf{b}^i\otimes\mathbf{b}^i$$

$$= \frac{2\pi}{3}(E)^{\frac{1}{\varsigma}-1}\begin{pmatrix}A & B & 0\\B & C & 0\\0 & 0 & D\end{pmatrix} \tag{135}$$

in which A, B, C, D, E are respectively

$$A = \frac{2(1+\left(\frac{1}{2}\left(l_e^2 - l_e\sqrt{l_e^2+4}+2\right)\right)^{\frac{\varsigma}{2}})}{l_e^2 - l_e\sqrt{l_e^2+4}+4} + \frac{2(1+\left(\frac{1}{2}\left(l_e^2 + l_e\sqrt{l_e^2+4}+2\right)\right)^{\frac{\varsigma}{2}})}{l_e^2 + l_e\sqrt{l_e^2+4}+4}$$

$$B = \frac{2(1+\left(\frac{1}{2}\left(l_e^2 - l_e\sqrt{l_e^2+4}+2\right)\right)^{\frac{\varsigma}{2}})(l_e - \sqrt{l_e^2+4})}{(l_e^2 - l_e\sqrt{l_e^2+4}+4)(l_e^2 - l_e\sqrt{l_e^2+4}+2)}$$

$$+ \frac{2(1+\left(\frac{1}{2}\left(l_e^2 + l_e\sqrt{l_e^2+4}+2\right)\right)^{\frac{\varsigma}{2}})(l_e + \sqrt{l_e^2+4})}{(l_e^2 + l_e\sqrt{l_e^2+4}+4)(l_e^2 + l_e\sqrt{l_e^2+4}+2)}$$

$$C = \frac{4(1+\left(\frac{1}{2}\left(l_e^2 - l_e\sqrt{l_e^2+4}+2\right)\right)^{\frac{\varsigma}{2}})}{(l_e^2 - l_e\sqrt{l_e^2+4}+4)(l_e^2 - l_e\sqrt{l_e^2+4}+2)} \tag{136}$$

$$+ \frac{4(1+\left(\frac{1}{2}\left(l_e^2 + l_e\sqrt{l_e^2+4}+2\right)\right)^{\frac{\varsigma}{2}})}{(l_e^2 + l_e\sqrt{l_e^2+4}+4)(l_e^2 + l_e\sqrt{l_e^2+4}+2)}$$

$$D = \left(\frac{1}{2}\left(l_e^2 - l_e\sqrt{l_e^2+4}+2\right)\right)^{\frac{\varsigma}{2}} + \left(\frac{1}{2}\left(l_e^2 + l_e\sqrt{l_e^2+4}+2\right)\right)^{\frac{\varsigma}{2}}$$

$$E = \frac{1+\left(\frac{1}{2}\left(l_e^2 - l_e\sqrt{l_e^2+4}+2\right)\right)^{\frac{\varsigma}{2}} + \left(\frac{1}{2}\left(l_e^2 + l_e\sqrt{l_e^2+4}+2\right)\right)^{\frac{\varsigma}{2}}}{3}$$

Substituting the above equations into Eq. 105, we can get the evolution equation of

$$\frac{dl_e}{dt} = r + \frac{2A_0\Gamma}{3\eta}E^{\frac{1}{\varsigma}}l_e - \frac{A_0\Gamma}{3\eta}E^{\frac{1}{\varsigma}-1}\left[A\left(l_e^3 + 2l_e\right) + B\left(l_e^2 + 1\right)\right] \tag{137}$$

in which A, B are the same as referred to in Eq. 136. After normalizing the time with characteristic relaxation time, we can get the evolution equation of λ_e with reduced time

$$\frac{dl_e}{d\tilde{t}} = \xi r + 2E^{\frac{1}{\varsigma}}l_e - E^{\frac{1}{\varsigma}-1}\left[A\left(l_e^3 + 2l_e\right) + B\left(l_e^2 + 1\right)\right] \tag{138}$$

The interfacial orientation degree with relaxation effects considered can be expressed with

$$\phi = \mathrm{B}_{e11} + \mathrm{B}_{e22} + \mathrm{B}_{e33} - 3 = l_e^2 \tag{139}$$

Combining Eq. 138 and 139 gives the information of the change of ϕ with reduced time for viscoelastic polymer blends subjected to simple shear deformation field. The result is shown in Figure 3-4.

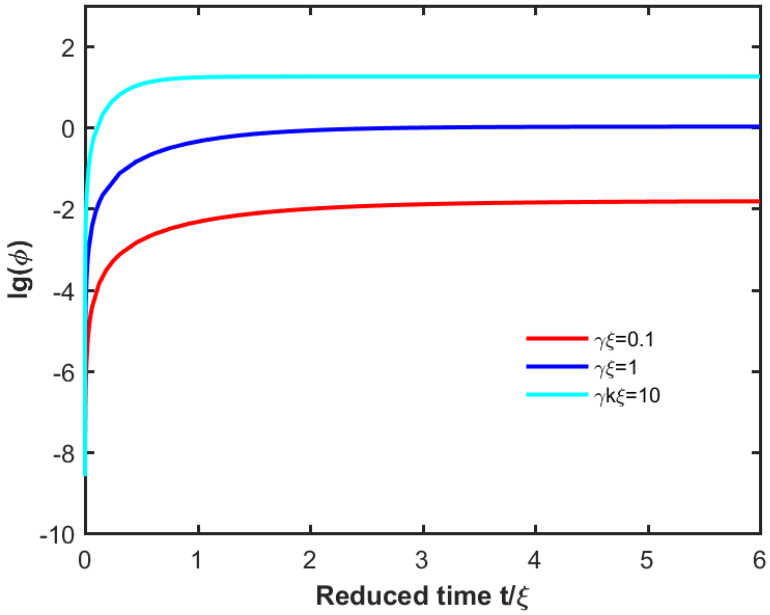

Figure 3-4 Interfacial orientation degree as a function of reduced time for simple shear flow with relaxation effects considered. A base-10 logarithmic scale is used for the Y axis.

The change of interfacial orientation degree of polymer blends in simple shear field has a similar trend of first increasing and then stabilizing. However, the magnitude of interfacial orientation degree in simple shear is not as large as it is in other elongational flow fields.

3.2.5 Comparison of the Prediction Results of Interfacial Orientation Degree with Considering Relaxation Effects and without the Relaxation Effects

In Chapter 2, the interfacial orientation degree of interfaces in affine deformation has been investigated. After obtaining the evolution equation of $\mathbf{B}_e$, interfacial orientation degree with relaxation effects considered can be acquired. Here the results for the interfacial orientation degree with and without the relaxation effects will be compared.

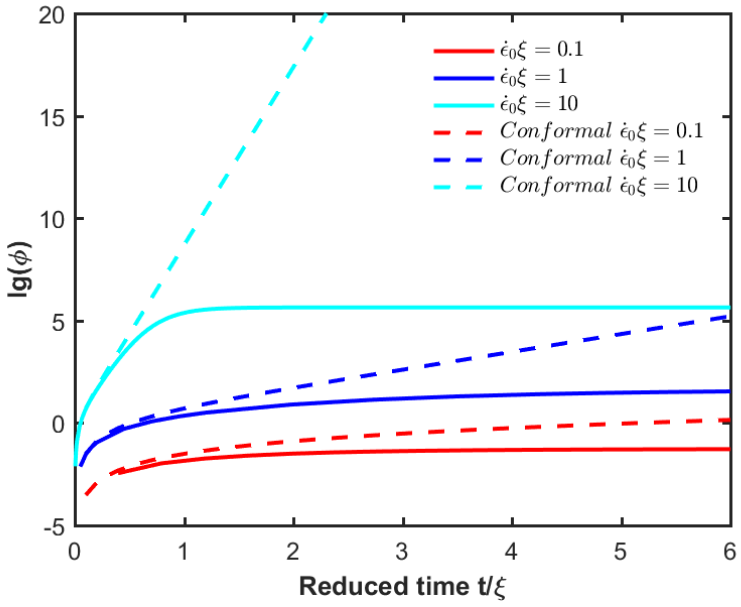

Figure 3-5 Comparison of interfacial orientation degree as a function of reduced time for uniaxial elongational flow with and without relaxation effects considered. A base-10 logarithmic scale is used for the Y axis.

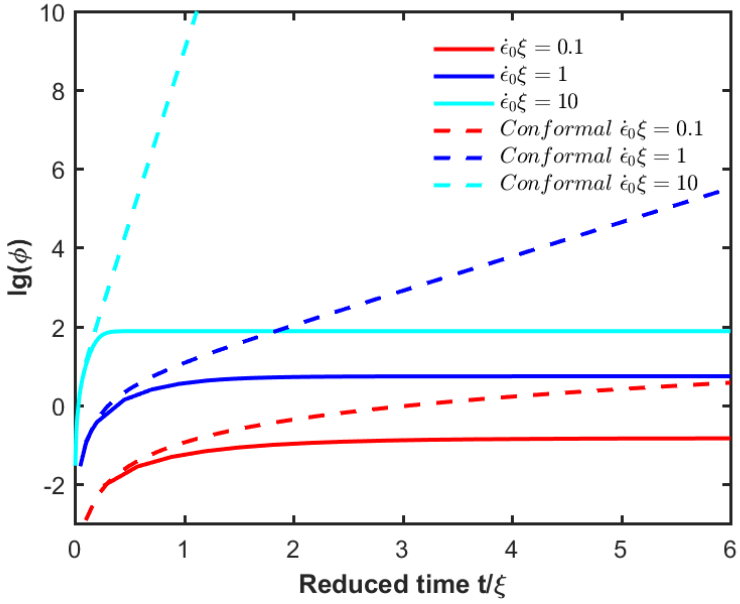

Figure 3-6 Comparison of interfacial orientation degree as a function of reduced time for biaxial extensional flow with and without relaxation effects considered. A base-10 logarithmic scale is used for the Y axis.

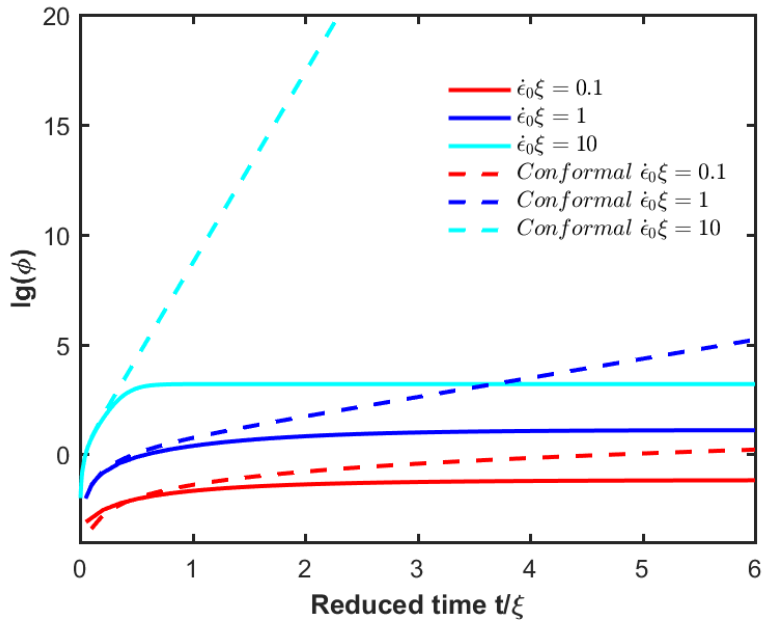

Figure 3-7 Comparison of interfacial orientation degree as a function of reduced time for planar elongational flow with and without relaxation effects considered. A base-10 logarithmic scale is used for the Y axis.

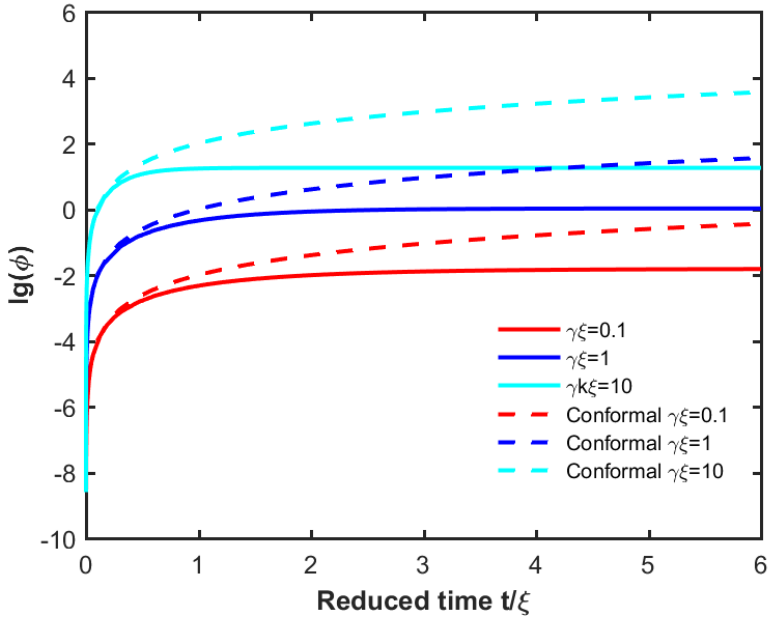

Figure 3-8 Comparison of interfacial orientation degree as a function of reduced time for simple shear flow with and without relaxation effects considered. A base-10 logarithmic scale is used for the Y axis.

Figure 3-5 to Figure 3-8 show the comparison of the results of interfacial orientation degree with relaxation effects and without relaxation effects in respectively uniaxial elongation flow field, biaxial extension flow field, planar elongation flow field and simple shear flow field. When the relaxation effects are not considered, i.e. when the complex interfaces are subject to affine deformation, the interfacial orientation degree will keep increasing with time. However, when the relaxation effects are considered, the interfacial orientation degree will stabilize at a time of orders of characteristic relaxation time. Therefore, when viscoelastic fluids such as polymers are encountered, we need to consider the relaxation effects for the interfacial orientation degree otherwise the predicted result would deviate from the actual situation.

3.2.6 Interfacial Orientation Degree in the Relaxation Process of A Blend Subjected to A Step Strain

The change of interfacial orientation degree in different deformation fields has been described in the previous part. With the same method we can also predict the interfacial orientation degree of polymer blends during relaxing after being applied a step strain.

Since the deformation field has gone, the velocity gradient is

$$\mathbf{L}(t) = \begin{pmatrix} \dot{\varepsilon}_0 & 0 & 0 \\ 0 & 0 & 0 \\ 0 & 0 & -\dot{\varepsilon}_0 \end{pmatrix} \tag{140}$$

The initial Finger strain tensor is

$$\mathbf{B}_0 = \begin{pmatrix} {\lambda_0}^2 & 0 & 0 \\ 0 & {\lambda_0}^{-1} & 0 \\ 0 & 0 & {\lambda_0}^{-1} \end{pmatrix} \tag{141}$$

The memorized strain tensor is

$$\mathbf{B}_e = \begin{pmatrix} {\lambda_e}^2 & 0 & 0 \\ 0 & {\lambda_e}^{-1} & 0 \\ 0 & 0 & {\lambda_e}^{-1} \end{pmatrix} \tag{142}$$

$$\frac{\partial g_e}{\partial \mathbf{B}_e} \cdot \mathbf{B}_e = \frac{2\pi}{3} \left(\frac{g_e}{4\pi}\right)^{1-\varsigma} \sum_{i=1}^{3} \sum_{j=1}^{3} (1-\delta_{ij})(k_i k_j)^{\varsigma/2} \mathbf{b}^i \otimes \mathbf{b}^i \tag{143}$$

Substituting the above equations into Eq. 105, we can get the evolution equation of λ_e,

$$\frac{d\lambda_e}{dt} = -\frac{2A_0\Gamma}{3\eta}\left(\frac{2\lambda_e^{\frac{\varsigma}{2}} + \lambda_e^{-\varsigma}}{3}\right)^{\frac{1}{\varsigma}} + \frac{A_0\Gamma}{3\eta}\left(\frac{2\lambda_e^{\frac{\varsigma}{2}} + \lambda_e^{-\varsigma}}{3}\right)^{\frac{1-\varsigma}{\varsigma}} \left(\lambda_e^{\frac{\varsigma}{2}-1} + \lambda_e^{-\varsigma-1}\right) \tag{144}$$

Normalizing it with the characteristic relaxation time, we can get the evolution equation of λ_e with reduced time,

$$\frac{d\lambda_e}{d\tilde{t}} = -2\left(\frac{2\lambda_e^{\frac{\varsigma}{2}} + \lambda_e^{-\varsigma}}{3}\right)^{\frac{1}{\varsigma}} + \left(\frac{2\lambda_e^{\frac{\varsigma}{2}} + \lambda_e^{-\varsigma}}{3}\right)^{\frac{1-\varsigma}{\varsigma}} \left(\lambda_e^{\frac{\varsigma}{2}-1} + \lambda_e^{-\varsigma-1}\right) \tag{145}$$

The interfacial orientation degree during the relaxation process can be written as

$$\phi = B_{e11} + B_{e22} + B_{e33} - 3 = {\lambda_e}^2 + 2{\lambda_e}^{-1} - 3 \quad (146)$$

With Eq. 145 and 146, we can know how the interfacial orientation degree changes during the relaxation process of polymer blends subjected to a simple step strain. With λ_0 set to 3, the change of interfacial orientation degree with reduced time is shown in Figure 3-9.

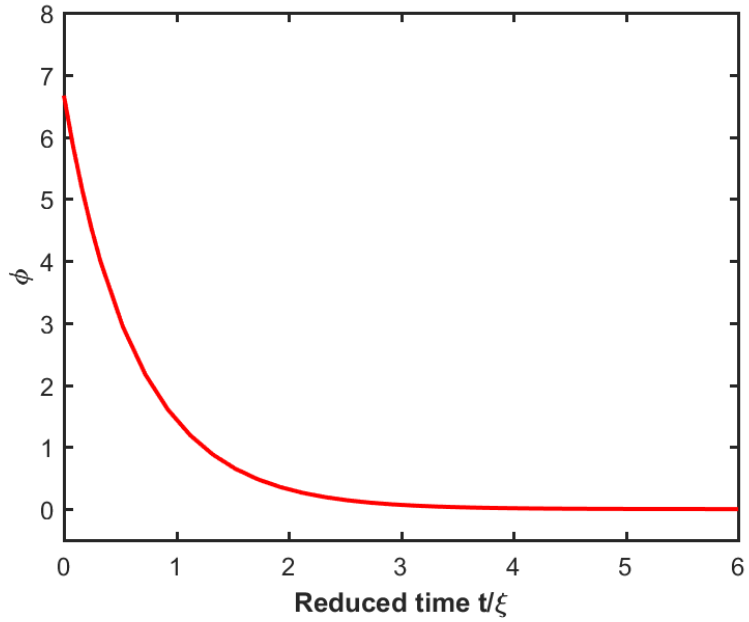

Figure 3-9 Interfacial orientation degree as a function of reduced time during relaxing of a blend subjected to a step strain.

As shown in Figure 3-9, the interfacial orientation degree decreases gradually during the relaxation process and reach almost zero at a time magnitude of orders of relaxation time.

Interfacial tension and viscosity both change when the temperature changes. Therefore, we can use Eq. 144 to predict the relaxation behavior of blends at different temperature and compare the predicted results with experimental results of stress relaxation of the blends. Here polypropylene (PP) and polystyrene (PS) blends with 50% weight

percent of PP will be used as a model system for the comparison. The PP/PS blend holds a nearly co-continuous structure. The stress relaxation experiment was conducted on a rotational rheometer (AR2000, TA Instruments) equipped with 25-mm parallel plate geometry. PP/PS blends were molded into disks with a diameter of 25 mm and a thickness of 1.5 mm. The stress relaxation experiment of PP/PS blend was performed at different temperatures from 200 to 230 ^{o}C to study how the temperature will influence the relaxation rate. The experimental result is shown in Figure 3-10. The result is plotted in a semi-log scale, and therefore the rate of relaxation can be represented with the absolute value of the slope. The increased slope with increased temperature as shown in the inset of Figure 3-10 indicates higher rates of relaxation at higher temperatures. When the temperature increases, the interfacial tension will decrease, which tends to decrease the relaxation rate [65]. In contrast, increasing temperature will lower the viscosity, which has an effect of increasing the relaxation rate. The experimental results of faster relaxation rate at higher temperature indicates that as temperature increases, the effect of the viscosity on relaxation rate is larger than that of the interfacial tension.

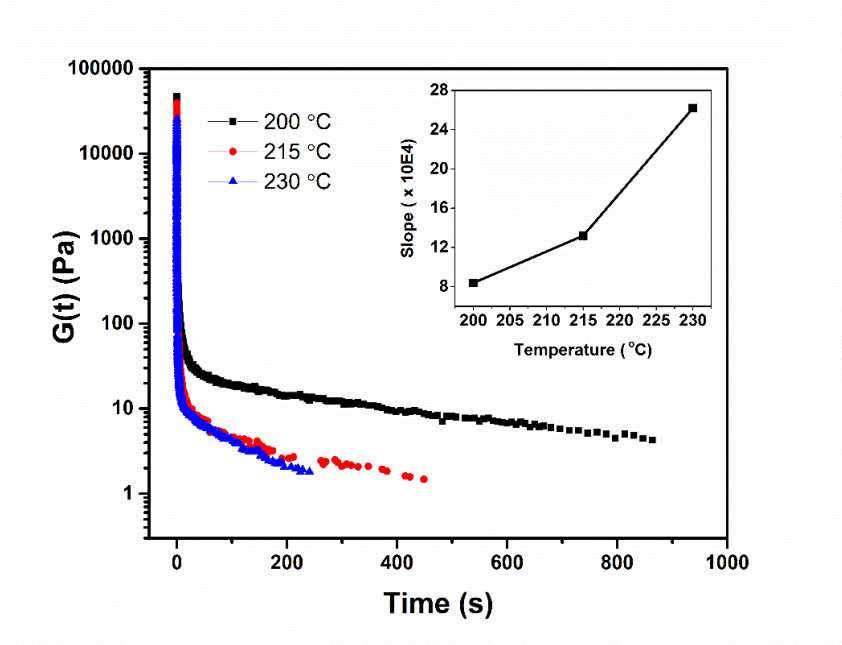

Figure 3-10 Stress relaxation of PP/PS 50/50 blend at different temperatures in semi-log coordinate. The Y axix of the inset represents the absolute value of the slope of the interface relaxation process and indicates rate of relaxation.

For PP/PS blend, the relationship of interfacial tension with temperature can be modeled using Eq. 147 [66].

$$\Gamma = 7.515 - 0.0128\,(T - 273)\,(\frac{mN}{m}) \tag{147}$$

The relationship of the blend viscosity can be expressed with Arrhenius equation. Here an activation energy of 49.93 KJ/mol is adopted [67]. The values of viscosity at different temperatures can be determined from

$$\eta = Ae^{\frac{E}{RT}} \tag{148}$$

in which A is a constant related with the materials, T is the absolute temperature with the unit of K, R is the ideal gas constant (8.314 J/mol·K) and E is the flow activation energy.

We choose the same temperatures as those used in the experiment (200 °C, 215 °C and 230 °C). From Eq. 147 and 148, we can get corresponding Γ, η. Substituting them into the evolution equation of λ_e, we can obtain how interfacial orientation degrees change with reduced time at different temperatures, as shown in Figure 3-11. It indicates that the relaxation rate increases when the temperature increases, which is consistent with the experimental results.

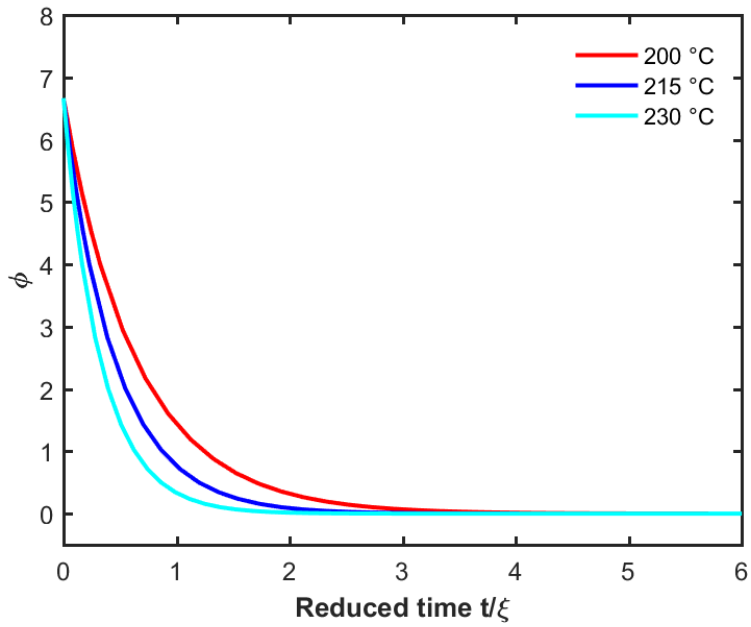

Figure 3-11 Interfacial orientation degree as a function of reduced time during relaxing of a blend subjected to a step strain at different temperatures.

3.3 Conclusions

Interfacial morphology of polymer blends has been studied a lot using interface tensor or area tensor which makes the computation complex. Therefore, those methods

might not be ideal for dealing with the interfacial morphology and rheology problems of the viscoelastic polymer blends with relaxation effects. The use of the Finger strain tensor for the calculation of the interface dynamics serves as one alternative method for understanding the morphology evolution. As already introduced in Chapter 2, the interfacial orientation degree in affine deformation can be easily accessed with the Finger strain tensor. For viscoelastic polymer blends with relaxation effects, the actual retained strain is not the one which is applied to the blend. Actually, the retained strain $\mathbf{B}_e$ is smaller because the relaxation effects generate a dissipated strain $\mathbf{B}_d$. The interfacial orientation degree is then related with the actual retained strain, $\mathbf{B}_e$. Using an energy balance approach, we can get the evolution equation of $\mathbf{B}_e$ for viscoelastic polymer blends with relaxation effects and thereby know how the interfacial orientation degree changes with time. The change of interfacial orientation degree with time is shown in uniaxial elongation deformation field, biaxial elongation deformation field, planar elongation deformation field and simple shear deformation field. Moreover, the change of interfacial orientation degree with reduced time in a relaxation process of polymer blends subject to a step strain is plotted. To validate the model, the interfacial orientation degree as a function of reduced time is plotted at three different temperatures and compared with experimental results of stress relaxation of polymer blends at the same series of temperatures. We hope this work may provide potential instructions for situations like polymer blends processing that need to consider relaxation effects.

4. PROCESS DESIGN FOR PREPARING USABLE PRODUCTS FROM IMMISCIBLE POLYMER BLENDS

4.1 Introduction

Despite extensive research on interface dynamics, there are currently no adequate studies about how to use interface dynamics to guide the process design of immiscible polymer blends processing. With respect to processing of immiscible polymer blends, a wide processing window is needed to robustly process the blends into usable products. The robustness of the process is especially important for improving its potential of being used in plastics waste recycling because recycled materials are less pure and many parameters are less well-controlled. To prepare usable products, the process should be able to enhance the mechanical properties of the blend products and therefore a proper design of different processing parameters is required. In this chapter, the interface dynamics, as described in Chapter 2 and Chapter 3, and relevant rheological studies will be used as a guidance for the process design of preparing usable products from immiscible polymer blends. Specifically, this chapter will introduce multiple constituent elements that are important for the process design, followed by a detailed description on how these constituent elements are combined and used for developing a robust and cost-effective process to prepare immiscible polymer blends products.

4.2 Constituent Elements

4.2.1 Nearly Co-continuous Morphology

The process design for the proposed methodology involves a concept called ‘nearly co-continuous morphology’, as shown in Figure 4-1. Traditionally, a fully co-continuous structure refers to the case where both of the two phases are continuously connected throughout the blend. As we know, the reason for the low mechanical properties of immiscible polymer blends is the poor interfacial adhesion. In the blend with a fully co-continuous structure, both phases share the load, which reduces the need of transferring stress across the phase boundary. In such a way, the need for sufficient interfacial adhesion as required to achieve desired mechanical properties is weakened and the blend with fully co-continuous structure shows higher mechanical properties than that with one-phase-being-dispersed structure [54]. The phase morphology control in preparing co-continuous blend has been investigated in different studies and multiple models were proposed to predict the phase inversion point, around which co-continuous morphologies are most likely to form [55]. In fully co-continuous structure, the continuity of both phases is 100%, which leads to increased difficulty of preparing the fully co-continuous structure. In contrast, a nearly co-continuous structure is relatively easier to be prepared, in which one phase is fully continuous while the other phase’s continuity is smaller than 100% (i.e., partly continuous). Therefore, a nearly co-continuous structure may be considered as the combination of fully co-continuous morphology and droplets structure. In nearly co-continuous morphology, at least one phase is continuous, which can act as the load-transfer phase and enhance the mechanical performance. A nearly co-continuous morphology may not be as effective in enhancing the properties as a fully co-continuous structure, but it should be adequate for achieving usable mechanical properties. Moreover, it is more economically viable and easier to process than a fully co-continuous structure.

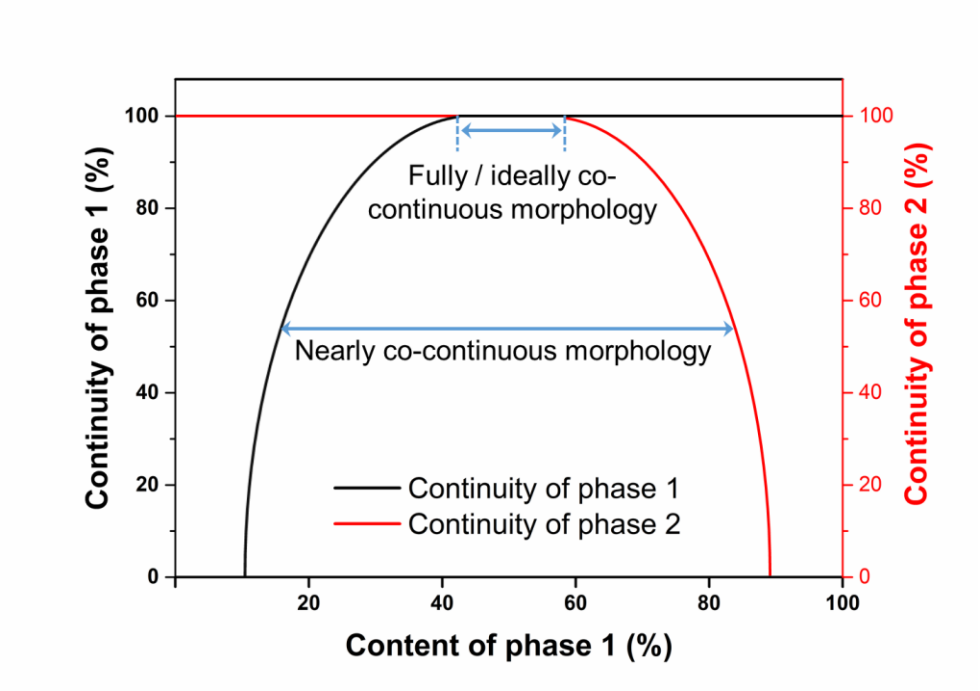

Figure 4-1 Nearly co-continuous morphology and fully co-continuous morphology of polymer blends.

4.2.2 Interfacial Orientation during the Processing of Immiscible Polymer Blends

Different from processing of single categories of polymers, processing of polymer blends using flow or stretch involves deformation and orientation of the interface. For blends with matrix-droplet structure, polymer interfaces refer to the boundaries of the droplets. Therefore, the orientation of the interfaces means the elongation of the boundaries, which is essentially the elongation / stretching of the droplets. For blends with co-continuous structure, interfacial orientation means the stretching and orientation of the network-shaped interface, which will stretch and elongate two polymer phases. Interfacial orientation acts as defects and deteriorates mechanical properties. Just like the stretching of the droplets will make the droplets break up, if phases in the co-continuous network are oriented and elongated too much, they will tend to break during later-stage processing.

Besides, large orientation of the interface may also lead to phase separation. From the results of Fu et al. [64], the large interfacial orientation from the strong force field of injection molding caused formation of layered structures and decreased the mechanical properties.

Since the interfacial orientation can significantly affect the mechanical properties of polymer blends, investigation of interfacial orientation degree in different deformation fields during polymer processing is important for the process design. The evolution of interfacial orientation with the consideration of relaxation effects has been introduced in Chapter 3， which indicates that there will be a persistent interfacial orientation when polymer blends are subject to a deformation field. Besides, by comparing the magnitudes of the interfacial orientation degree in different deformation fields as shown from Figure 3-1 to Figure 3-4, it can be seen that elongational flows generate a much larger interfacial orientation than shear flow. Among the three elongational flows, uniaxial elongation introduces the largest elongation degree. With Figure 3-1 and Figure 3-4, we can calculate how much larger the interfacial orientation generated in uniaxial elongation is than that in simple shear. When the deformation is small (less than 1), the interfacial orientation in uniaxial elongation is more than tenfold of that in simple shear. However, when the deformation is large (more than 10), uniaxial elongation may generate an interfacial orientation which is more than ten thousand times of the interfacial orientation developed in simple shear.

4.2.3 Relaxation Time of Interfacial Orientation and Molecular Orientation

In addition to the interfacial orientation discussed above, molecular orientation also has a large effect on the mechanical properties. The relaxation time of the interfacial orientation and molecular orientation should be considered when different processing parameters are determined. Therefore, the interfacial relaxation time and molecular relaxation time were investigated by rheological studies where nearly co-continuous polypropylene/polystyrene blends were used as a model system.

First, the stress relaxation behavior of the pure components and the blends at melt state in the linear viscoelastic region was tested with stress relaxation experiments with a step strain. As shown in Figure 4-2, both pure components (PP and PS) exhibit a rapid one-step relaxation within 20 s. However, the PP/PS 50/50 and PP/PS 70/30 blends show a two-step relaxation: first a fast relaxation due to the relaxation of the pure components; then a second slower relaxation, as indicated by the plateau and terminal relaxation at longer times. The second-step relaxation is contributed by the slower interface relaxation in the nearly co-continuous structure. In co-continuous structure, the two phases form interpenetrating networks and confine each other from moving fast, which leads to the slow interface relaxation [68]. Normally the stress relaxation behavior of immiscible blends can be treated with a linear mixing rule, i.e., the total relaxation modulus is equal to the sum of the contributions of the interface and the two polymer phases. With this consideration, the Maxwell model with two relaxation times, which respectively represent the relaxation of the polymer molecules and the interface, is used to fit the experimental data of stress relaxation experiment of PP/PS 50/50 blend. The result for the fitting is shown in Figure 4-3. A relaxation time of 0.035 s turns out to fit the stress relaxation behavior of polymer molecules while a relaxation time of 165 s indicates a good fitting to the stress relaxation

of the interface at longer time scale. Although the model fits well for the short time scale and long time scale, it does not give a good fitting to the in-between time scale, indicating that one relaxation time might not be enough to model the relaxation of the interface.

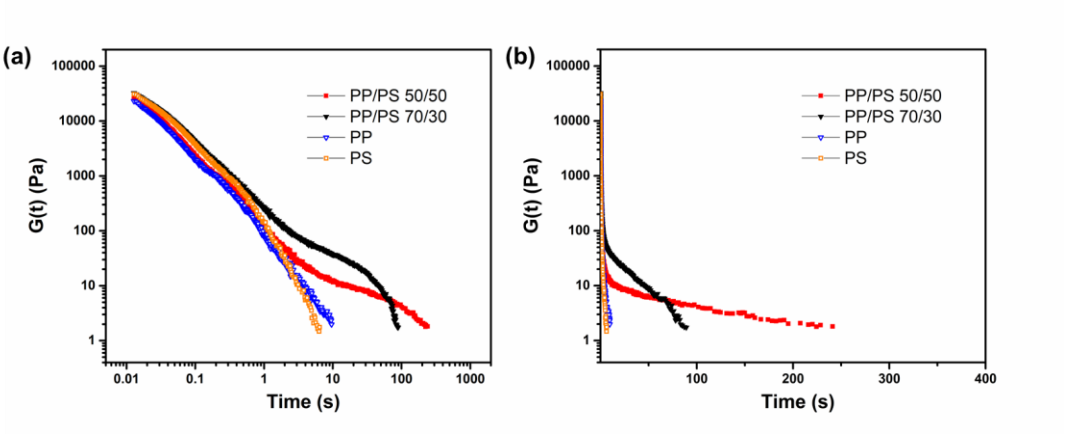

Figure 4-2 Stress relaxation behavior of the component polymers and the blends (a) Log-Log scale (b) Semi-Log scale.

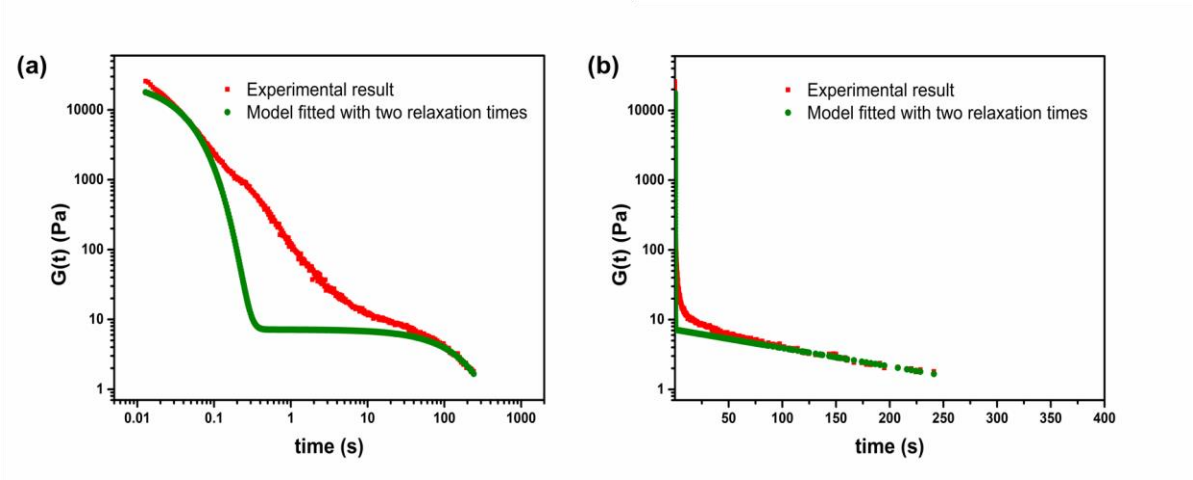

Figure 4-3 A relaxation model fitted with two relaxation times simulating the stress relaxation behavior of PP/PS 50/50 blend (a) Log-Log scale (b) Semi-Log scale.

The stress relaxation plot suggests different relaxation mechanisms for the pure components and the polymer blends. The relaxation spectra of the blends was examined for the understanding of their relaxation behavior from a more quantitative perspective.

Figure 4-4 (a) shows the relaxation spectra, H(τ), of the PP/PS 70/30 blend, PP/PS 50/50 blend and component polymers PP and PS. The relaxation spectra were calculated using a second order approximation proposed by Tschoegl [69],

$$H(\tau) = G'\left[\frac{d\ logG'}{d\ log\omega} - \frac{1}{2}\left(\frac{d\ logG'}{d\ logw}\right)^2 - \frac{1}{4.606}\frac{d^2 logG'}{d(logw)^2}\right]_{\tau=\sqrt{2}/\omega} \quad (149)$$

In Figure 4-4 (a), the relaxation of the components is reflected in the left hand side of the spectra while the relaxation of the interface is contained in the right hand side. The difference between the blend and their components are not distinguished from each other. Therefore, a method of plotting the weighted relaxation spectrum τ·H(τ) versus τ proposed by Gramespacher and Meissner [70] was used to separate the relaxation times of the interface from the contribution of the components. In the weighted spectra, the slower interfacial relaxations become more evident as the contribution of slow processes is magnified by the use of the first moment. Figure 4-4 (b) shows the normalized weighted spectra of the two blends and their components, in which the peaks in the left hand side depicts the contribution of the component polymers and the peak and the tail in the right hand side represent the slower relaxation processes. The PP/PS 70/30 blend contains a certain amount of PS droplets, which brought about the peak appearing in the right-hand side. The 50/50 blend is more co-continuous, therefore, its weighted spectra shows a tail observed in the high τ region which corresponds to the relaxation of the co-continuous interface. Li et al. [71] observed a similar behavior in the co-continuous PMMA/SMA blend. It was believed that the slow relaxations of interpenetrating networks of the co-continuous structure led to the appearance of the tail.

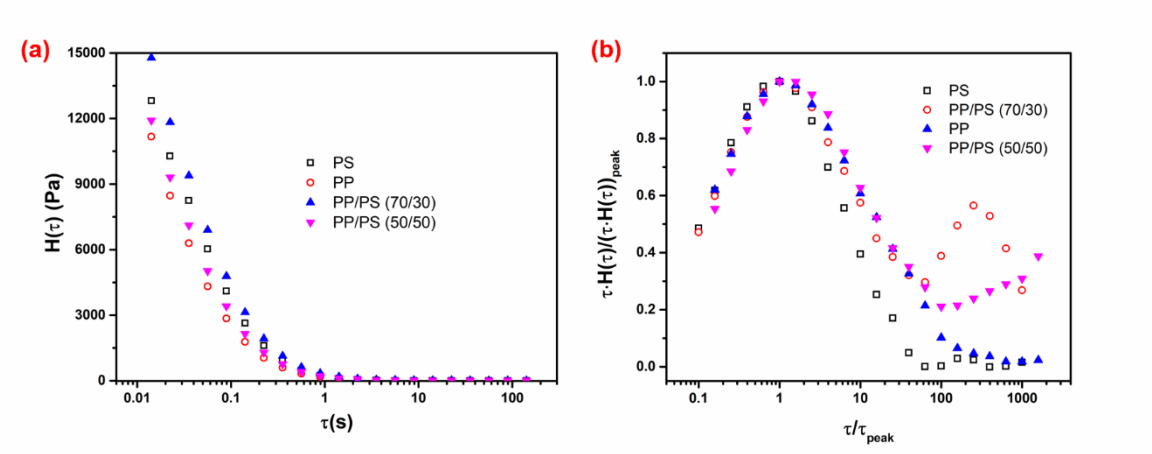

Figure 4-4 (a) Relaxation spectra (b) weighted relaxation spectra for PP/PS 70/30 and PP/PS 50/50 blends and their component polymers at 230 ºC.

The result of stress relaxation experiments with model fitting and the weighted relaxation spectrum indicate that the relaxation time of the interface orientation is much longer (more than a thousand times) than that of the pure components/polymer molecules orientation at high temperature. This phenomenon of slower relaxation of the interface than the molecules has also been reported by other researchers [71, 72]. Since these two relaxations are so different, the process should be specially designed in order to achieve usable properties.

4.3 Process Design

After the constituent elements are introduced, this section focuses on how they are combined and used for the process design. We have already demonstrated that a nearly co-continuous phase should be adopted for enhancing mechanical properties and reducing processing cost. A large interfacial orientation tends to damage the co-continuity and decrease mechanical properties while a large molecular orientation is essential for enhancing the mechanical properties. The general purpose of the designed process is to

minimize interfacial orientation and create at least one continuous phase with large molecular orientation. The results of interface dynamics indicate that the interfacial orientation will be persistent when polymer blends are subjected to a deformation field during polymer processing. On the other hand, the rheological studies show that the interfacial orientation relaxes much slower than the molecular orientation at high temperature. Therefore, if a deformation field is applied to polymer blends at a relatively high temperature, the interfacial orientation will be large while the molecular orientation is small; in other words, a large interfacial orientation will be generated way earlier than the molecular orientation. This is unfavorable for the mechanical properties from two aspects. First, the large interfacial orientation decreases the co-continuity of the blends, which is not desired for enhancing mechanical properties. Second, because of the large difference in the two relaxation times, the molecular orientation is still small while the interfacial orientation is already large. The large interfacial orientation brings problem of easier breaking and hinders the later-stage processing. As a result, the small molecular orientation has little chance to be increased later with subsequent steps of processing. Therefore, the interfacial effects should be mitigated while we try to increase the molecular orientation of the blend with a nearly co-continuous structure. One potentially capable process for achieving this objective is fiber spinning, with which stage-by-stage operations can be used to test variable processing conditions and obtain an optimized process for achieving usable properties. Additional steps can be added for generating large degree of deformation and enhancing the molecular orientation and mechanical properties. To decide upon specific processing parameters, we turned to the interface dynamics and rheological properties again. The evolution of interfacial orientation degree in different deformation

fields indicates that elongational flows, especially uniaxial elongation, generate a much larger interfacial orientation degree than shear flow. Combining this point with the observation that molecular orientation relaxes much faster than interfacial orientation at high temperature, we infer that elongational flow needs to be avoided at the liquid state of polymer blends. Therefore, we proposed to minimize jet stretch because it is mainly uniaxial elongation and polymer blends are not solidified yet at the beginning of jet stretch. In such a way, interfacial orientation can be mitigated. A separate hot drawing step at a relatively low temperature will then be applied to increase the molecular orientation. Since the temperature is relatively low during hot drawing, the relaxation time of molecular orientation is increased and the difference between the relaxation time of molecules and interfaces is not that large. As a result, a relatively large degree of molecular orientation can be generated and retained.

Although the theoretical study regarding interface dynamics and rheological properties has some limitations, it can serve as an adequate tool for determining a general processing window. This processing methodology is designed for uses with different combinations of materials. It should be mentioned that material properties such as molecular weight or viscosity may vary for different blend compositions. However, the same strategy can be used as long as the basic guidelines are followed; i.e., the nearly co-continuous morphology which ensures at least one continuous phase is employed, and the interfacial effects are mitigated before the desired level of molecular orientation is achieved. In contrast, a processing methodology employing a fully co-continuous morphology will not be as robust as the current one. In that case, the fully co-continuous morphology can be easily destroyed due to the changes of material properties (e.g.

viscosity). In our processing design, fully co-continuous morphology is not necessary and a nearly co-continuous phase is employed instead. The latter is not that fragile and can survive the large deformation fields more easily, which increases the robustness of the process. Besides, the step of increasing molecular orientation while mitigating interfacial orientation is still feasible even if material properties such as viscosity change. According to the rheological studies, the relaxation time of interfacial orientation is more than a thousand times longer than that of molecular orientation. Therefore, even if the interfacial relaxation time changes because of the change of materials or material parameters, its order of magnitude is still much larger than that of molecular relaxation time, indicating that the general guideline is still suitable.

4.4 Conclusions

Interface dynamics and rheological studies have been used in guiding the process design of preparing usable products from immiscible polymer blends. Basically, a processing methodology of mitigating the interfacial effects during processing and then generating stronger materials by creating a continuous phase with high molecular orientation has been proposed. When polymer blends are deformed during processing, there are two kinds of orientations being generated: interfacial orientation and molecular orientation; the former represents a defect and deteriorates mechanical properties, while the latter is desired for improving mechanical performances. Since interfacial orientation will decrease mechanical properties and hinder the later-stage processing, one may want to reduce interfacial orientation during processing, especially before the desired level of molecular orientation is generated. From the study of interface dynamics, it can be seen that the interfacial orientation generated in elongational flow fields is much larger than that

in shear flow fields. The rheological results show that at high temperatures the relaxation time of the interface is considerably larger than that of polymer molecules. This indicates that in melt processing at high temperatures, interfacial orientation should dominate over molecular orientation if the blend is subjected to an elongational flow such as jet stretching, which is unfavorable for obtaining desired mechanical properties. Accordingly, we propose the following processing strategy for mitigating interfacial orientation and promoting molecular orientation in melt spinning of immiscible blends: applying no jet stretch during melt extrusion and subsequently hot drawing the blend fiber at a relatively low temperature. Although the constitutive modeling is a coarse grain model which just gives a high-level prediction and cannot give exact modeling results of rheological behaviors, they are adequate for us to design a general processing strategy. The effectiveness of this strategy for enhancing mechanical properties of immiscible blends product is evaluated using the PP/PS system that forms a nearly co-continuous phase structure where PP is the continuous phase, which will be demonstrated later. In addition to enhancing mechanical properties, this process may also be used for achieving additional properties by using suitable combinations of different materials and open up new blend products innovation.

5. PREPARATION OF STRONG FIBER FROM IMMISCIBLE POLYMER BLENDS

5.1 Introduction

Millions of tons of plastics are produced and consumed every year but only a small part of them are recycled. Many plastics end up in landfills or become pollutants in natural environment. Recycling helps reduce cost and environmental impacts [73]. Generally, the postconsumer plastic waste contains multiple polymers. Therefore, the recycling of such waste requires a pre-step of separation. Otherwise, immiscibility of polymers will lead to products with poor mechanical performances. However, the separation process is expensive and time-consuming, which makes the recycling not economically viable. In addition, not all the wastes can be separated, such as polymer blends. Therefore, a recycling method without the pre-separation process, which is economical and technically feasible, is needed for efficient and effective recycling. Since most polymers are immiscible from each other [74], the principal technical challenge is to overcome the immiscibility and transform the mixed polymers into value-added products. The aim of the current work is to develop a melt-processing method where mixing and extrusion can be used to produce articles with good mechanical properties from mixed polymers containing immiscible components. Since the reason for the low mechanical properties originates from the poor adhesion at the interface of the polymer blends caused by the immiscibility, some researchers attempted to improve the mechanical properties of the obtained products by adding a compatibilizer to enhance the interface adhesion. The effects of concentration and type of compatibilizers on mechanical properties have been extensively studied [8-10].

Although compatibilizers provide the potential of giving the overlooked waste mixture new values, use of compatibilizers has limitations in validity, availability, economic feasibility or processibility. Therefore, a method without using the compatibilizers for direct processing of mixed polymers is desired for more efficient and economic plastics recycling.

In the current study, methods for the direct melt-processing of immiscible polymers into fiber with good mechanical properties were investigated. The reasons for choosing fiber as the product form is given as follows. First, fiber spinning is a unique processing method that has different characteristics from other processing methods. It has the potential to endow improved properties to polymer blends by molecular orientation. Second, fibers from polymer blends may have new properties compared with that from pure polymers. In particular, combination of different polymers in a single fiber can render mechanical properties and surface properties in a large extent [57, 75]. Recently, immiscible polymer blends have also been used in fabrication of nanofibers, accomplished by dissolution or mechanical removal of a sacrificial phase after fiber spinning [76]. However, in small diameters, fiber properties are sensitive to defects and inhomogeneity. The reported mechanical properties of fibers from immiscible polymer blends are usually not good, and previous research has been largely focusing on a droplet-in-sea morphology (that is, a minor phase dispersed in a major phase) [77, 78]. Therefore, a meaningful challenge to overcome when processing fiber from immiscible polymers is to spin strong fibers at high polymer mixing ratios using commercially viable processes such as melt spinning. Hot drawing is a widely-used method in melt spinning. Researchers have studied the hot drawing process of both single-polymer fibers [79, 80] and fibers made from polymer blends [81]. The influence of hot drawing on the morphological structures and mechanical

properties of hot drawn fibers/films from immiscible polymer blends have also been studied. For example, Xing [77] studied the morphological changes of hot drawn PP/PS composite fibers in which PS phase had a content of 4 to 8 percent and existed as droplet or fibrils. They found that the hot drawing process only slightly reduced the size of PS phases in cross-section and inferred that the deformation was not that effective because the stress was difficult to be transferred from the PP phase to the PS phase. Erkoc [82] studied the effects of hot drawing ratio on PP/PET blends and found that the PET droplets changed from spherical to rod-like shape and finally to fibrils. The drawing also increased the mechanical properties when the PET was low in content. When the weight percentage of PET increased, the mechanical properties decreased, which they thought might be due to the lack of interfacial adhesion between the two polymers and the agglomeration of PET droplets.

We particularly investigated how to melt spin a blend containing immiscible components at high mixing ratios and improve the strength of the resultant fiber. In principle, a co-continuous morphology (CCM) is desired when spinning a blend of large polymer mixing ratios since such a morphology enables load transfer; however, a genuine CCM may be difficult to obtain in practice. Accordingly, we introduce a concept of "nearly co-continuous morphology" (NCCM) for materials processing and products realization when immiscible polymer blends especially in a form of waste are encountered. In contrast to the CCM, a NCCM only requires one fully continuous phase presented in the structure for load transferring purposes while the remaining phase can be left partially continuous or slightly disconnected. Such a NCCM is easier to obtain than the genuine CCM, and yet it provides an engineering solution to the production of stronger fiber from immiscible

polymer blends. The key part of this processing strategy is to identify a process window for creation of an NCCM based on the understanding of the rheological properties of immiscible polymer blends. An immiscible blend containing polypropylene (PP) and polystyrene (PS) at different mixing ratios was chosen as a model system to demonstrate the applicability of the new processing methodology.

5.2 Experimental

5.2.1 Materials

The PP used in this study is polypropylene homopolymer supplied by Braskem America with a melt flow index of 0.5 g/10 min (230 ^{o}C, 2.16 Kg). The PS used was obtained from Sigma-Aldrich with an average M_w of 350,000 and an average M_n of 170,000.

5.2.2 Melt Blending and Fiber Processing

PP/PS blends were prepared using a batch mixer (C.W. Brabender Prep-Center fitted with twin roller blades). Blends with three weight fraction ratios were prepared, respectively at PP/PS 70/30, PP/PS 50/50, PP/PS 30/70. The mixing time, mixing temperature and rotating speed are 15 minutes, 230 °C and 80 RPM, respectively. The obtained blend was quenched in cold tap water and cut into small pieces for uses in capillary rheology and fiber spinning.

The obtained PP/PS blends were melt-spun at 230 ^{o}C using a Malvern RH7 Advanced Capillary Rheometer. The throughput rate was set at 1 mm/min to avoid apparent shark skin phenomenon. The diameter of the capillary die is 0.25 mm. Nearly zero

jet stretch was applied to the as-spun fiber (neglecting the stretch caused by gravity). Because of the existence of extrusion swell, the obtained as-spun fiber has a diameter between 0.3 mm to 0.35 mm. After the as-spun fiber was cooled, it was hot drawn at temperatures from 80 ^{o}C to 110 ^{o}C to obtain a hot-drawn blend fiber. The fiber extrusion and hot drawing process are shown in Figure 5-1. The drawing ratio was between 6 and 13. In a nutshell, this process prepares fiber by first obtaining an as-spun fiber with no jet stretch and then simply hot drawing the as-spun fiber at a temperature near the T_g of PS.

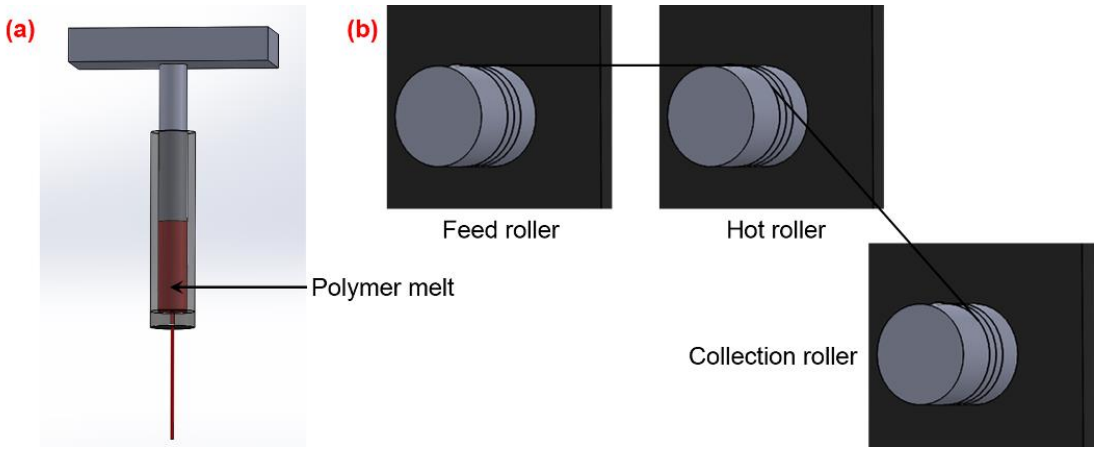

Figure 5-1 (a) Fiber extrusion process (b) Hot drawing process.

For comparison purposes, fibers were also prepared using the conventional melt spinning method in which the fiber is taken up at high speed with large jet stretch introduced. Specifically, when the fiber is being extruded, it was collected by a roller with a take up speed of 150 - 250 m/min, producing a jet stretch of more than 200. The resulting fiber was drawn completely via jet stretch and no subsequent hot drawing was applied.

5.2.3 Characterization

The microstructure of the PP/PS blends was observed with an LEO 1530 Scanning Electron Microscopy (SEM). The blends were immersed in magnetically stirring

cyclohexane for 12 hours to etch away the PS and treated by a 45 second gold sputtering before the SEM observation.

Melt shear viscosities of PP, PS and their blends were measured using a Malvern RH7 capillary rheometer. Other rheology tests (strain sweep, frequency sweep and stress relaxation) were performed on a rotational rheometer (AR2000, TA Instruments) equipped with 25-mm parallel plate geometry. Polymer blends were molded into disks with a diameter of 25 mm and a thickness of 1.5 mm. Strain sweep tests were performed from an initial strain of 0.1% to a final strain of 100% at 10 rad/s to determine the linear viscoelastic region of the polymers. Dynamic frequency sweep was carried out at 230 ^{o}C over a frequency range of 0.01-100 rad/s within the linear viscoelastic regime. PP, PS and the blend samples were subjected to a shear strain within the linear viscoelastic regime to investigate their different stress relaxation behavior. Stress relaxation tests were also performed at different temperatures from 200 to 230 ^{o}C to study how the temperature will influence the relaxation rate.

An Instron 5566 universal testing machine was used to perform the uniaxial tensile testing. Test samples were randomly selected and clamped between the Instron fixtures. Crosshead speed was set at 25 mm/min with a gauge length of approximately 10 cm. All tensile tests were conducted under ambient conditions (40 – 60% relative humidity at 20 – 22 ^{o}C). Fiber diameters were measured using a microscope.

Differential scanning calorimetry (DSC) was performed on a TA Q200 DSC unit (TA Instruments). The as received PP pellets were subjected to a heat-cool-heat cycle from 40 to 200 ^{o}C to remove thermal history. Data from the second heating cycle was used for

analysis. The blends and the blend fiber were heated from 25 to 200 ºC and data from the heating cycle was collected. The apparent crystallinity of PP pellets was determined with the following equation:

$$Degree\ of\ crystallinity\ (\%) = \frac{\Delta H_{\mathrm{f}}}{\Delta H_{\mathrm{f}}^{0}} \times 100 \tag{150}$$

in which ΔH_{f} is the measured enthalpy of PP and $\Delta H_{\mathrm{f}}^{0}$ is the melting enthalpy of 100% crystalline PP which is 190 J/g [83]. For the blend fiber, the crystallinity of PP is calculated using the same equation and based on the portion of PP in the blends. Hermetic pans were used for all DSC analysis. Nitrogen atmosphere and a ramping speed of 10 ºC /min were used.

5.3 Results and Discussion

5.3.1 Morphology of PP/PS Blends

SEM images (Figure 5-2) show that both the PP/PS 70/30 blend and the PP/PS 50/50 blend hold a nearly co-continuous morphology. In the PP/PS 70/30 blend, the phase size of the PS phase is about 20 micrometers, smaller than the phase size in the PP/PS 50/50 blend. In the PP/PS 50/50 blend, the continuity of the PS phase is higher than that in the PP/PS 70/30 blend. SEM images for the PP/PS 30/70 blend were not able to be obtained because the blend dissolved and was not able to support itself after 12 hours in cyclohexane. It suggests that PS is the continuous phase in the PP/PS 30/70 blend.

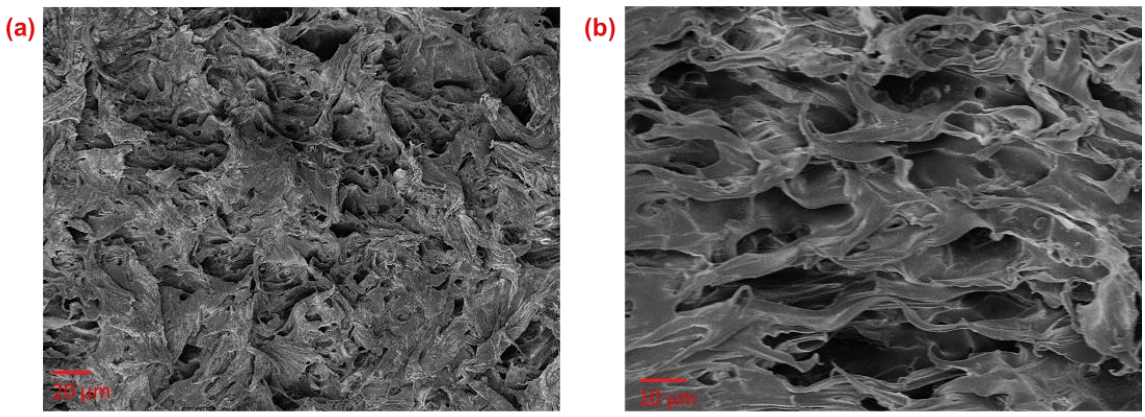

Figure 5-2 (a) SEM of 70/30 wt% PP/PS blend (b) SEM of 50/50 wt% PP/PS blend.

5.3.2 Rheological Characterization

The shear viscosity-shear rate relations of pure PP, pure PS and the three PP/PS blends were tested across a shear range of 10 - 3000 s^{-1} at 230 ^{o}C. The results are shown in Figure 5-3, which manifests that the PP/PS blend has a similar shear thinning behavior with the pure polymers and a slightly lower viscosity than PP. This indicates that the PP/PS blend may be easier to be extruded than pure PP. In fact, we found that the extrusion of PP generated shark skin problem before the blend did when they were extruded with the same speed using the capillary rheometer. Han and Yu [84] suggested that the reduced viscosity might be caused by the easier slippage of the matrix phase along the interface of the immiscible PP/PS blend system.

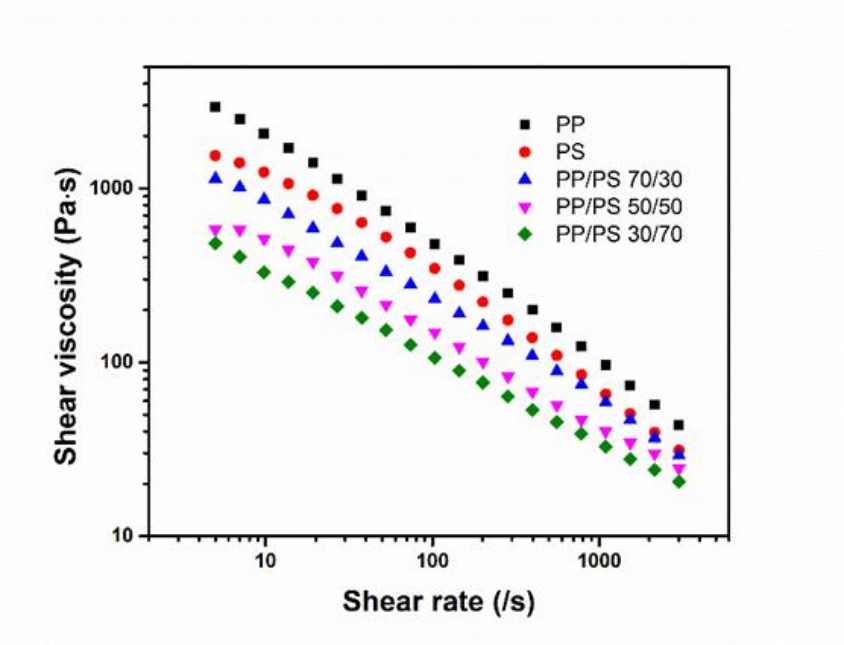

Figure 5-3 Shear viscosity of the component polymers and the blends.

Figure 5-4 (a) and (b) respectively show the dynamic moduli for the two components and for the blends (PP/PS 70/30 and PP/PS 50/50) measured at 230 °C. We calculated the average moduli of the component properties as the component moduli for comparison with the moduli of the blend. Different mixing rules have been introduced in literature [85]. Here geometrical means, given by G'_{comp} (Avg 50/50) = $G'_{PP}{}^{0.5}G'_{PS}{}^{0.5}$ and G''_{comp} (Avg 50/50) = $G''_{PP}{}^{0.5}G''_{PS}{}^{0.5}$ are used for comparison with the PP/PS 50/50 blend while G'_{comp} (Avg 70/30) = $G'_{PP}{}^{0.7}G'_{PS}{}^{0.3}$ and G''_{comp} (Avg 70/30) = $G''_{PP}{}^{0.7}G''_{PS}{}^{0.3}$ are used for comparison with the PP/PS 70/30 blend. We can see that the average moduli of the component properties with the two ratios are close to each other. Figure 5-4 (b) shows that the blend interface does not influence G'', while G' of both blends deviated from the average value of the compositions. Although 70/30 blend and the 50/50 blend both have nearly co-continuous phase structures, the continuities are different, which leads to their different G' at low frequencies. In the PP/PS 70/30 blend, although the content of PS is as

high as 30%, the phase continuity of PS is smaller than unity and PS droplets exist. Therefore, the G′ curve of 70/30 has a shoulder, which is a characteristic of the matrix-droplet morphology. According to Vinckier and Laun [86], the shoulder structure in the G′ curve in matrix-droplet morphology is generated because the development of the disperse droplet phase leads to an increase in the elasticity of the blend at low frequencies. They also managed to obtain the droplet diameter distribution at a particular stage in the phase separation and growth process by fitting the G′ curves with the emulsion model of Palierne [33]. However, its shoulder is not as obvious as a typical matrix-droplet morphology; this difference may be explained since the PS phase in this blend is expected to be partly continuous and partly droplet like. The G′ of the 50/50 blend shows a power law-like relation at low frequencies, a behavior that is seen in fully co-continuous structure. Vinckier and Laun [86] thinks that the power law-like behavior at low frequencies in fully co-continuous structure can be explained by its similarity with network structures. Just like the number of crosslinks per unit volume in network structures, the number of "interconnections" per unit volume in a molten blend is expected to be important in affecting the elastic behavior. Another explanation on the power-law behavior is the presence of domains with different characteristic lengths, which leads to relaxation processes with different characteristic times [87]. It is also believed that the extra elastic stress is due to the extra free energy stored at the interface, which is influenced by the interfacial area and interfacial curvature [40, 88].

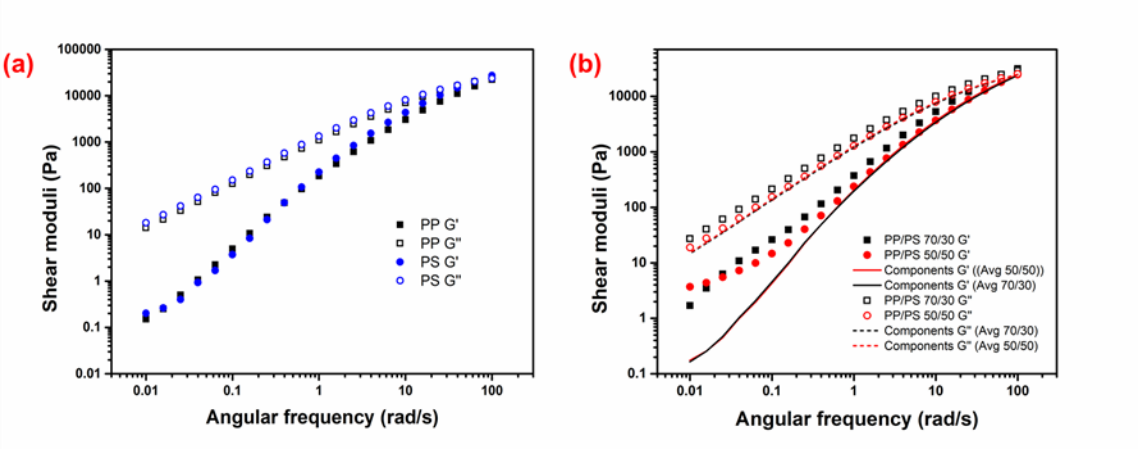

Figure 5-4 Dynamic moduli with frequency over 0.01 – 100 s^{-1} for (a) the component polymers PP and PS (b) Dynamic moduli as a function of frequency for the blends 70/30 PP/PS and 50/50 PP/PS and the average of their components.

5.3.3 Mechanical Properties

5.3.3.1 Fiber Prepared with the Proposed Methodology

Jet stretch ratio, which is the on-line draw ratio during fiber extrusion, is an important parameter for fiber spinning process. In many cases of fiber spinning, a high drawing speed introduces high jet stretch ratio, which brings about large molecular orientation and increases the mechanical properties of the obtained fiber [89]. However, this high speed spinning method does not work in some situations. Instead, one would use low speed on-line drawing to make sure just a small jet stretch is introduced while the major drawing was imparted by separate drawing process. In our process, we removed the on-line drawing and the jet stretch was almost zero. Basically, fiber from PP/PS 70/30 blend was prepared with the proposed methodology: no jet stretch and separate hot drawing applied later at a relatively low temperature. The biggest challenge of processing PP/PS blend into strong products comes from the immiscibility, which will weaken the mechanical properties of the final products and may even hinder the processing by making the product break during

the processing. Considering the fact that PP and PS have different thermal behaviors, figuring out a processing window is also an important step. Different hot drawing temperatures were tested to determine the best hot drawing temperature. The purpose is to decrease the bad influence that PS phase brings and make sure that the PS phase will not interrupt the drawing process or disturb the orientation of the PP molecules. A constant low drawing speed was used to adequately soften the PS phase and properly draw the fiber. The results are presented in Table 5-1.

Table 5-1 Mechanical properties of PP/PS 70/30 blend fibers hot drawn at different temperatures.

Hot-draw temperature (^{o}C)	Draw ratio (times)	Tensile strength (MPa)	Standard Deviation (MPa)	Young's modulus (GPa)	Standard Deviation (GPa)
80	6 - 8	240	89	2.50	0.68
100	10 - 13	330	31	9.37	2.17
110	10 - 13	330	45	8.66	1.96

Compared with the as-spun fiber with no hot drawing, which has a tensile strength of 18 MPa and a Young's modulus of 1.43 GPa, fiber prepared with the proposed methodology has much higher tensile strength and Young's modulus. Suitable hot drawing temperatures are 100 – 110 ^{o}C. At this temperature, the fiber can be drawn 10 to 13 times and the tensile properties of the fiber are comparable to PP fiber reported in previous literature which had 6 – 15.5 times in draw ratio, 400 – 600 MPa in tensile strength and 6

– 15.5 GPa in Young's Modulus [90]. When the temperature is too low, e.g. 80 ^{o}C, the PS phase is rigid, which will cause a misfit between the PP phase and the PS phase and hinder the drawing and orientation of the PP phase. When the temperature is near the Tg of PS phase, the PS phase is softened and will not resist the drawing process; the PP molecules have enough mobility to be drawn and oriented. The hot drawing temperature cannot be too high; otherwise, the PS phase will melt and the dimensional stability of the blend will deteriorate.

5.3.3.2 Fiber Prepared with Traditional Melt Spinning – Applying Large Jet Stretch

Fibers were prepared using the conventional melt spinning method, in which nearly all the drawing is completed by jet stretch. Three take-up speeds were implemented to apply different jet stretch ratios, and the mechanical properties of the resulting fiber were measured (see Table 5-2).

Table 5-2 Mechanical properties of the PP/PS 70/30 fiber prepared via large jet stretch.

Take-up speed (m/min)	Jet stretch ratio (times)	Tensile strength (MPa)	Standard Deviation (MPa)	Young's modulus (GPa)	Standard Deviation (GPa)
150	210	38	4.5	0.17	0.07
200	280	43	4.6	0.25	0.22
250	350	47	7.2	0.25	0.09

Although the draw ratio of these fibers are large, their mechanical properties are much weaker than the fiber prepared with the proposed methodology. Increasing the take-up speed (jet stretch ratio) increases the tensile strength slightly, however all the samples are too weak to be utilizable. These results show that the traditional spinning method with large jet stretch produces blend fiber with relatively low mechanical strength.

5.3.3.3 Fiber Prepared by Combined Jet Stretching and Hot Drawing

To further understand the effect of jet stretch, we used a series of relatively small take-up speed to introduce a certain degree of jet stretch and then hot drew the fiber. The fibers from PP/PS 70/30 blend were hot drawn to the maximum level before breakage. The high jet stretch made the fiber less stretchable and the hot drawing ratio was between 1 and 2 times, much smaller than that of the fiber without jet stretch. The mechanical properties of the obtained fibers were measured and shown in Figure 5-5. The data indicates that both the tensile strength and the tensile modulus reduce with increasing jet stretch. This unfavorable effect may be attributed to interfacial orientation generated during jet stretch, hindering the hot drawing process and deteriorating the mechanical properties.

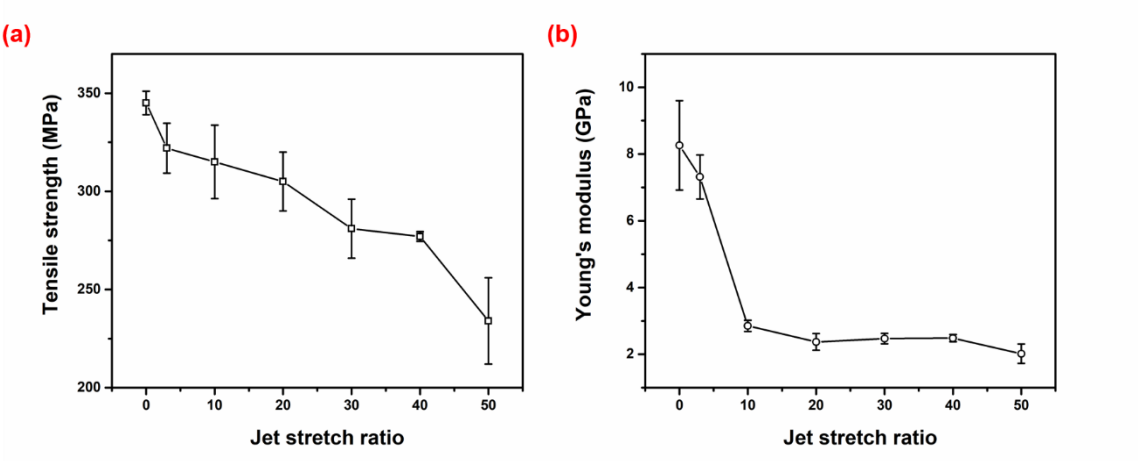

Figure 5-5 Tensile strength and (b) Young' modulus of hot drawn PP/PS 70/30 fiber with different jet stretch ratio.

5.3.3.4 Blend Fiber with Different Composition Ratios

In addition to PP/PS 70/30 blend, we also prepared fiber using the proposed methodology from the blends PP/PS 50/50 and PP/PS 30/70 and compared their properties with those of PP fiber and PS fiber. As shown in Figure 5-6, we are able to obtain relatively strong fiber using PP/PS 70/30 and PP/PS 50/50 blends which both have nearly co-continuous structure. Even though the blend is not fully co-continuous, the obtained products are strong. These results indicate that a nearly co-continuous phase structure may be adequate for generating a fiber product of good mechanical performance, and yet more economically obtainable than a true co-continuous phase structure. However, we cannot produce strong fiber from the PP/PS 30/70 blends. In this PP-minor blend, PS is the continuous phase so that the path for hot-drawing the PP phase becomes discontinuous. Note that PP is the strong phase in the blend fiber especially after orientation, so a continuous PP phase is desired for load transferring. On the other hand, hot drawing does not significantly alter the mechanical properties of the PS phase since PS is amorphous and hot drawing occurs at a temperature close to the T_g of PS where relaxation is relatively fast.

Therefore, a blend fiber with a continuous PP phase is desired for improved mechanical performance.

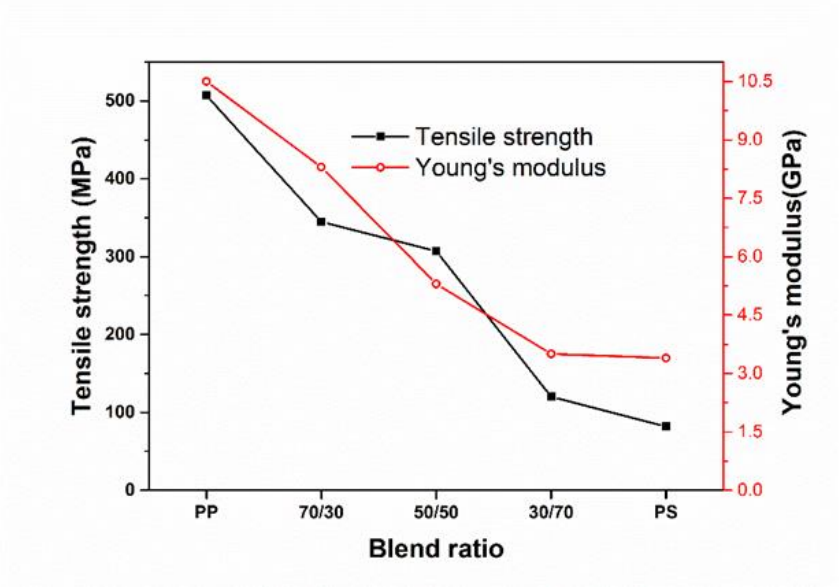

Figure 5-6 Tensile strength and Young's modulus of the hot drawn fiber with different composition ratio.

5.3.3.5 Summary for Mechanical Properties

In a nutshell, we have proposed the following methodology for preparing fiber from immiscible polymer blends involving two sequential steps: (1) producing a precursor blend fiber with nearly zero jet stretch; (2) hot drawing the blend fiber at a suitable temperature to substantially orientate the load transferring phase. Using this methodology, we have successfully prepared PP/PS 70/30 blend fibers with tensile strength above 300 MPa. In contrast, the traditional melt spinning method, in which the drawing is mostly achieved via large jet stretch, cannot produce fiber with comparable tensile strength. As already shown with stress relaxation behavior and relaxation spectra, the interfacial relaxation time is much longer than the molecular relaxation time at the extrusion temperature. If the fiber is

largely stretched when it is being extruded in the melt state, the interfacial orientation will be large while the molecular orientation is low. The large interfacial orientation developed during flow serves as a defect, hindering the subsequent hot drawing process. Therefore, the traditional melt spinning process involving large jet stretch is not suitable for processing strong fibers from immiscible polymer blends. In contrast, the method explored in this study advocates the use of small jet stretch (or nearly zero jet stretch if technically possible) for preparing a fiber precursor. This means the interfacial orientation in the as-spun fiber is small. We can then apply a separate hot drawing step at a relatively lower temperature than the extrusion temperature. At this lower temperature, the relaxation time of molecules is large, so the molecules can be extensively oriented during the drawing. Although the interfacial orientation will be introduced at the same time, the molecular orientation is large and can be retained in the continuous, load-bearing phase so that a strong blend fiber can be obtained.

5.3.4 Thermal Properties

The melting temperature and crystallinities of the PP/PS 70/30 blend fiber prepared using the proposed methodology were studied and compared with those of the as received pellets, as-spun fiber and large-jet-stretch fiber. As shown in Figure 5-7, the melting temperature and crystallinity of the hot-drawn fiber are respectively 168.3 ^{o}C and 62.5% (calculated with the enthalpy), which are both higher than those of the pellets and as-spun fiber. Compared with the large-jet-stretch fiber, the hot-drawn fiber's melting temperature and crystallinities are 5 ^{o}C and 22.3% higher, respectively. Although the crystallinity of large-jet-stretch fiber increases compared with the as received pellets and as-spun fiber, its melting temperature is lower, which indicates the existence of imperfect crystalline

structure that might be caused by the low temperature during the fiber's fast cooling down after extrusion.

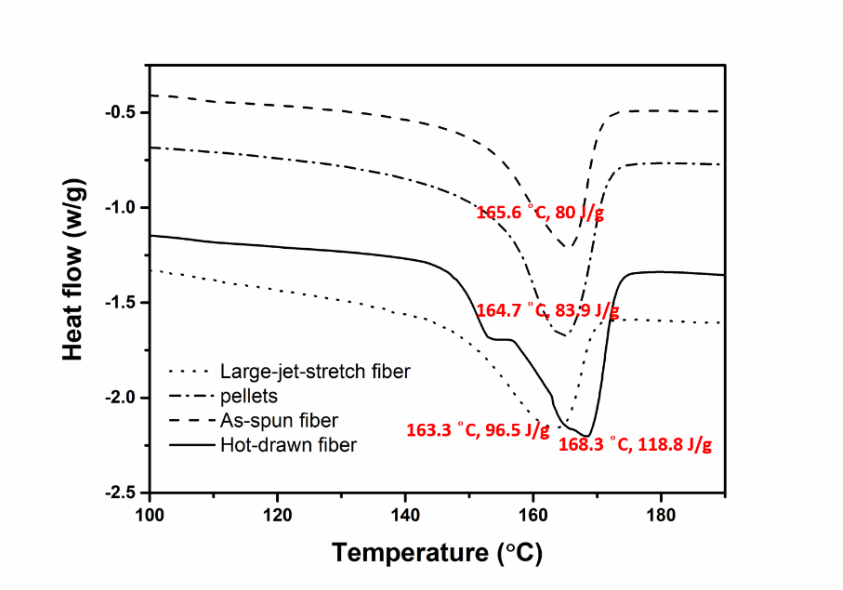

Figure 5-7 DSC thermograms of PP pellets, as-spun blend fiber, large-jet-stretch blend fiber and hot-drawn blend fiber (prepared from PP/PS 70/30).

To understand the influence of hot drawing temperature on crystalline structure, we measured the thermal properties of fiber that were hot drawn under different temperatures and the results are shown in Table 5-3. Compared with the as-spun fiber (T_m = 165.6 ^oC and crystallinity 42.1%), the fiber hot drawn at all the three temperatures has higher melting temperatures and crystallinities. When the hot drawing temperature increases, the melting temperature and crystallinity increase, which indicates the crystalline structure formed in the hot drawing process is relatively perfect compared with that formed in the jet stretch.

Table 5-3 Thermal properties of the blend fiber that were hot drawn at different temperatures.

Hot drawing temperature (^oC)	Draw ratio (times)	Melting temperature (^oC)	Enthalpy ΔH (J/g)	Crystallinity (%)
80	6 - 8	165.7	97.3	51.2
100	10 - 13	167	108	56.8
110	10 - 13	168.3	118.8	62.5

5.4 Conclusions

A simple and cost-effective method for preparing strong fiber from immiscible blends was proposed and demonstrated using PP/PS blends as a model system. Since immiscible polymers are subjected to weak interfacial adhesion and the interfacial orientation generated during melt processing is considered harmful, the products obtained from immiscible polymers usually have poor mechanical properties. We proposed a methodology employing a "nearly co-continuous structure" and a "no-jet-stretch but separate hot-drawing" process for achieving improved mechanical strength. For the PP/PS blend, a suitable hot drawing temperature was identified near the T_g of PS. The constitutive modeling and rheological tests helped identify proper conditions for orientating the molecules and inspired the process design. Easy and cost-effective processing methods were used to generate a "nearly co-continuous structure", as observed in the SEM images. Results from mechanical tests show that this methodology can produce much stronger fiber

than the traditional melt spinning method. One reason for the improved mechanical properties is that the unfavorable jet stretch is minimized in this approach. DSC results demonstrate that the obtained fiber has higher melting temperature and crystallinity than the fiber from the traditional method. This further explains the improved mechanical performance of the resultant fiber. One major challenge for directly recycling mixed polymers without steps of pre-separation or compatibilizers is poor mechanical properties caused by immiscibility. The proposed methodology may therefore mitigate this disadvantage and produce strong fiber from immiscible polymer blends in a cost-effective way.

6. PREPARATION OF SUPERCONTRACTION FIBER FROM POLYCAPROLACTONE/ELASTOMER BLENDS

6.1 Introduction

After employing the nearly co-continuous structure to improve the mechanical properties of the blend fiber, we want to explore making use of the nearly co-continuous structure to get polymer blend products with other novel properties. In this study, polymer blends of polycaprolactone (PCL) and ethylene-octene block copolymer (OBC) are prepared and then made into fibers with a two-step process of melt extrusion and drawing. Supercontraction is well-known in some natural fibers. It describes the phenomenon of a much larger shrinkage in the longitudinal dimension of the fiber than that occurs in the normal textile fibers [91]. The shrinkage may be induced by elevated temperature, swelling agents, wettability, etc. Whewell and Woods [92] introduced the concept of "supercontraction" of natural fibers in 1946, and since then, there have been more research on the mechanisms and applications of supercontraction phenomenon. For example, Singha et al. [93] indicated that the reason of supercontraction of spider silk is the destruction of hydrogen bond by water molecules resulting in molecular chain motion and disorientation . Pérez-Riguejro et al. [94] proposed a method of obtaining predictably tailored spider silk fibers by combining forced silking and controlled supercontraction. With its capability of large deformation and fast actuation, supercontraction fiber has the potential of being applied in biomedical areas such as self-tightening sutures, sensors and

actuators. Another advantage of supercontraction fiber is that, compared with other forms of heat shrinking products like shrinking film, supercontraction fiber can construct complex structures via conventional textile techniques, such as knitting, weaving or braiding. When knitted with other functional fibers together, other properties can be combined to make a supercontraction fabric with improved structural, mechanical and functional properties. In fields where complex micro-sized objects need to be largely deformed and then supercontract to original size, supercontraction fiber will be an ideal candidate for constructing the complex object. Besides, fiber can be embedded into a matrix to make fiber composites with value-added properties.

Supercontraction phenomenon is not limited to natural fibers. Synthetic polymers also have this capability. For example, heat shrinkable polymers have wide applications in packaging, heat shrinkable tubing, electronic engineering and cable insulation [95]. Different techniques have been used for making heat shrinkable products. Kumar et al. [96] used crosslinking to prepare thermally recoverable materials. Khonakdar et al. [97] studied the heat shrinkability of crosslinked low-density polyethylene/poly(ethylene vinyl acetate) blends. Highly shrinkable polyester fiber was made in the 1980s, achieving a boiling water shrinkage of at least 40% [98]. 3D printing technique was also used to endow polymer heat-shrinkable property [99]. The printed PLA can shrink up to 22.7% and the shrinkage is caused by the uniform internal stress stored in printed material. However, those methods may have limitations. For example, the shrinkage ratio of the material is not high enough and therefore is not suitable for use in various fields such as intelligent medical devices and smart textiles where extremely large shrinkage is desired. In addition, some products used chemical crosslinking which makes the product hard to be recycled or degraded.

Furthermore, although there are commercial heat-shrinkable films in the market, they do not have high shrinkage ratio and they cannot replace fiber in many fields, especially when complex fabricated structures are needed. With the market demand for supercontraction fiber and the fact that natural supercontraction fibers have a limited availability and high cost, supercontraction fiber made from synthetic polymer is a field worth investigation.

In this work, we aim at designing a simple method for preparing a relatively environmentally-friendly supercontraction fiber with an extremely high shrinkage ratio. Polymer blends from polycaprolactone (PCL) and ethylene-octene block copolymer (OBC) with different blend ratios are prepared and then fibers were spun from these blends. Experimental results of heat shrinking test shows that the fiber prepared from the 50/50 PCL/OBC blend can shrink by up to 8 times upon heating. To understand the mechanism of the large shrinkage ratio, we performed a series of characterization and testing to obtain morphological properties, rheological properties, thermal properties, and mechanical properties. We found that one important factor for shrinkage ratio is the morphology of the blend. As already introduced, immiscible polymer blends have different morphologies, among which dispersed phase-matrix structure and co-continuous structure are two common ones and are widely studied. In our work, the co-continuity of PCL/OBC blend is important for the supercontraction ability of the fiber. We will not introduce the phase morphology control in detail here as how to prepare co-continuous blend has been studied by different researchers and different models were proposed to predict the phase inversion point, around which co-continuous morphologies are most likely to form [60]. Instead, we will focus on the preparation and properties of the supercontraction fiber.

6.2 Experimental

6.2.1 Materials

The OBC used here is INFUSETM 9007 olefin block copolymer (melt index 0.5 g/10 min, 190 ^{o}C /2.16 Kg), provided by Dow Chemical. The PCL used is Capa^{TM} 6800 (approximate molecular weight 80,000), provided by Perstorp Polyols, Inc.

6.2.2 Melt Blending and Fiber Processing

Component ratio is an important parameter for the blend morphology, which will then influence other properties. Therefore, PCL/OBC blends with three weight fraction ratios (respectively at PCL/OBC 80/20, PCL/OBC 50/50, PCL/OBC 20/80) were prepared using a batch mixer (C.W. Brabender Prep-Center fitted with twin roller blades). Pure PCL pellets and pure OBC pellets were also processed with this batch mixer. In this way, we have five samples in which the percentages of PCL decrease from 100 to 0 and the percentages of OBC decrease from 100 to 0, with which we can study the influence of the content of the two components. Different mixing time, mixing temperature and rotating speed were tried for melt blending and finally 10 minutes, 135 ^{o}C and 50 RPM were chosen for ensuring good mixing while not causing too much degradation. The obtained blends were quenched in cold tap water, dried and cut into small pieces for uses in rheology tests and fiber spinning.

Melt extrusion was conducted using a Malvern RH7 Advanced Capillary Rheometer to produce the fiber precursor. The extrusion was conducted at 150 ^{o}C with a 0.5 mm capillary die and a 1 mm/min flow rate. Nearly zero jet stretch was applied when producing the fiber precursor (neglecting the stretch caused by gravity). After the fiber precursor was cooled, it was drawn at room temperature to obtain the supercontraction fiber. It was found

that the drawing ratio is positively related with the shrinkage ratio of the obtained fiber. Therefore, we drew the fiber precursor to the maximum drawing ratio, which is around 8. In a nutshell, this process prepares fiber by first obtaining a fiber precursor with no jet stretch and then simply drawing the as-spun fiber at room temperature. The drawing is performed under room temperature based on the following considerations. Charuchinda et al.'s research work [100] about melt spinning PCL indicates that off-line room temperature drawing introduces the molecular orientation and improves the tensile strength of PCL fibers. Although the on-line drawing (jet stretch) is widely used for spinning high melting point polymers to induce molecular orientation, this method does not work for the case of spinning PCL or its blends. Charuchinda explained that that is because the fiber can only cool to a temperature just below the PCL's Tm and therefore is not able to generate enough molecular orientation. Based on their finding, our work also used the room temperature drawing instead of on-line drawing.

Inspired by previous research about the effects of hot drawing in polymer fiber /polymer composite fiber [101, 102], we applied hot drawing to the fiber and checked how it would influence the mechanical properties and the shrinking ability of the fiber. The hot drawing of the fiber was conducted in a 50 ^{o}C glycerol bath and the draw ratio was around 1.3.

6.2.3 Characterization

A Hitachi SU8010 Scanning Electron Microscopy (SEM) was used to observe the microstructure of the PCL/OBC blends and the PCL/OBC 50/50 fiber precursor and fiber.

Before the SEM observation, some samples were immersed in magnetically stirring acrylic acid for 12 hours to etch away the PCL phase and treated by 60 seconds of gold sputtering.

A Malvern RH7 capillary rheometer was used to measure the melt shear viscosities of PCL, OBC and their blends. A rotational rheometer (AR2000, TA Instruments) equipped with 25-mm parallel plate geometry was used to conduct tests including strain sweep and frequency sweep. Polymer blends were molded into disks with a diameter of 25 mm and a thickness of 1.5 mm. From the strain sweep test results performed from an initial strain of 0.1% to a final strain of 100% at 10 rad/s, we were able to get the linear viscoelastic region of the polymers. Dynamic frequency sweep was carried out at 150 ^{o}C over a frequency range of 0.01-100 rad/s within the linear viscoelastic regime.

An Instron 5566 universal testing machine with a 100 N tension-compression load cell was used to perform the uniaxial tensile testing and tensile testing with loading and unloading cycles. Crosshead speed was set at 25 mm/min for uniaxial tensile testing and 50 mm/min for loading and unloading tensile testing. All tensile tests were conducted under ambient conditions. The Instron Blue Hill 3 software was used to analyze the results.

Differential scanning calorimetry (DSC) was performed on a TA Q200 DSC unit (TA Instruments). The PCL pellets were subjected to a heat-cool-heat cycle from 40 to 150 ^{o}C to remove thermal history. Data from the second heating cycle was used for analysis. The blends and the blend fiber were heated from 40 ^{o}C to 200 ^{o}C and then cooled down to 40 ^{o}C. The tests were conducted in nitrogen atmosphere with a ramping speed of 10 ^{o}C /min. Hermetic aluminum pans were used for all DSC tests. The apparent crystallinity of OBC and PCL was determined with the following equation:

$$\text{Degree of crystallinity (\%)} = \frac{\Delta H_f}{\Delta H_f^0} \times 100 \quad (151)$$

in which ΔH_f is the measured enthalpy of the polymer and ΔH_f^0 is the melting enthalpy of 100% crystalline polymer. The enthalpy for 100% crystalline PCL and OBC are respectively 135 J/g and 290 J/g [103, 104]. The crystallinity of PCL in the blend fiber is calculated using the same equation and based on the portion of PCL in the blends.

When the fiber is exposed to higher temperature of 100 ^oC, they will shrink. The heat shrinking ability of fibers was measured using the following equation:

$$\text{Shrinkage ratio R} = \frac{\text{initial length} - \text{final length}}{\text{final length}} \quad (152)$$

6.3 Results and Discussion

6.3.1 Morphology of Blends and the Fiber from 50/50 PCL/OBC Blend

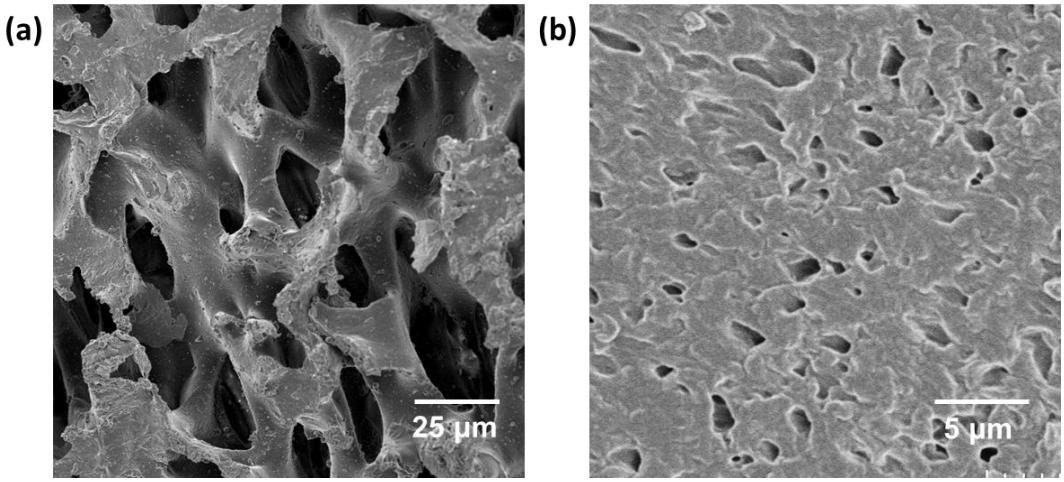

Figure 6-1 SEM images of (a) 50/50 wt% PCL/OBC blend (b) 20/80 wt% PCL/OBC blend.

The morphologies of PCL/OBC 20/80 blend and PCL/OBC 50/50 blend were observed using SEM and shown in Figure 6-1. Before observation, the samples were immersed in acetic acid to dissolve the PCL phase. We cannot get the SEM image of the blend PCL/OBC 80/20 because after the PCL phase was etched away, the blend was not able to self-stand. The SEM image of PCL/OBC 20/80 indicates that it holds a matrix-droplet structure in which the OBC phase forms the matrix. In contrast, the PCL/OBC 50/50 blend forms a co-continuous structure in which both the two phases are interconnected. The different structures of these two blends may be responsible for the different heat shrinking behavior of the corresponding fibers, which will be presented in the later parts of this chapter.

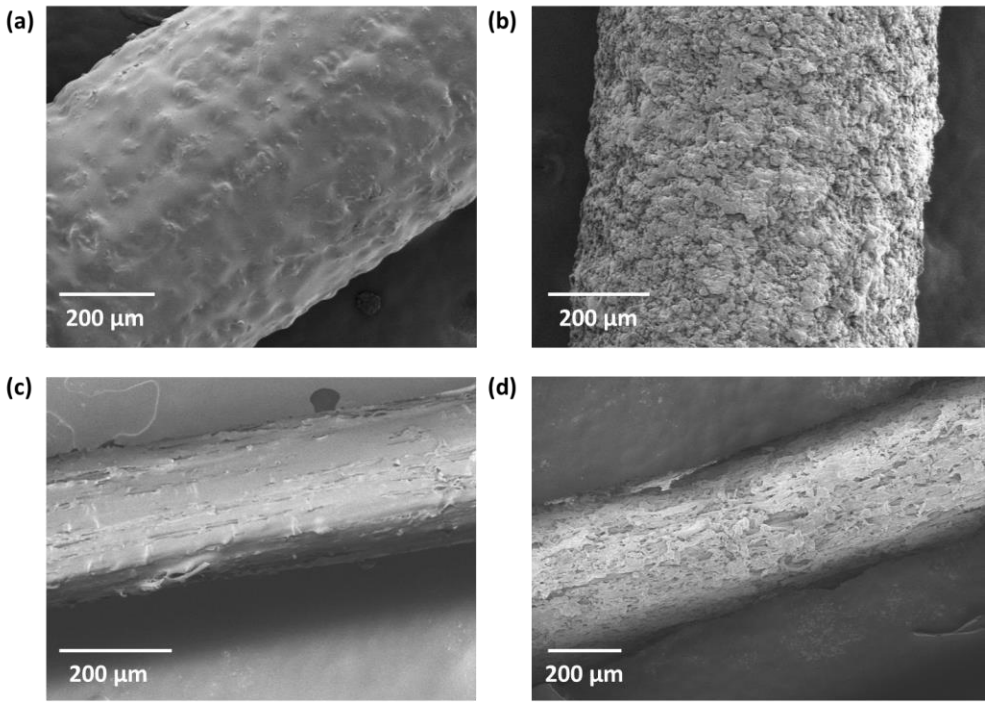

Figure 6-2 SEM images of longitudinal (a) fiber precursor (b) fiber precursor with PCL etched away (c) fiber (d) fiber with PCL etched away. All the fiber precursor and fiber were prepared from 50/50 PCL/OBC blend.

The SEM images of as prepared fiber precursor and fiber (prepared from 50/50 OBC/PCL blend) in longitudinal direction were shown in Figure 6-2 (a) and (c). The surface of the fiber precursor has some bumps which might be caused by the large difference in melting temperatures between OCL and OBC. The drawing process of preparing the fiber introduced cracks on the surface of the fiber, as shown in Figure 6-2(c). This might be due to the large difference in the Young's modulus of the two polymer phases. We also observed how the fiber precursor and the fiber look when the PCL phase was etched away, as shown respectively in Figure 6-2(b) and Fig. 3(d). After etching of PCL, the surface of the fiber precursor is rough and uneven, while the surface of the drawn fiber is relatively smoother but contains pores at the surface. The etched fiber behaves more like a typical elastomeric fiber since part of the PCL phase was removed and the OBC phase is no longer locked.

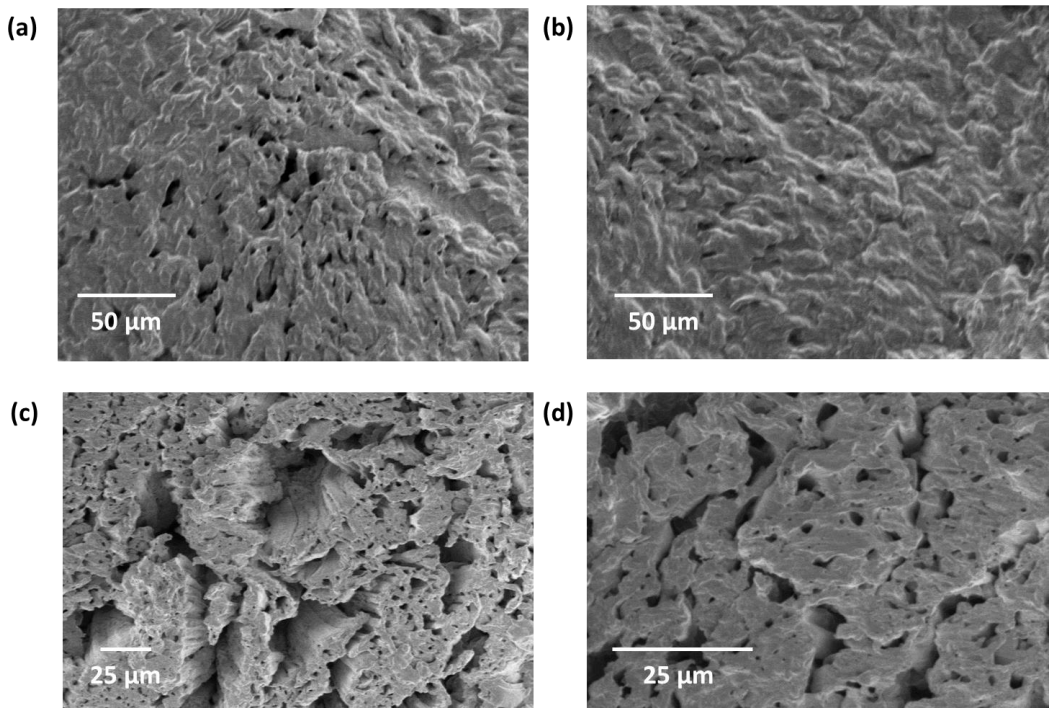

Figure 6-3 SEM images of cross-sectional (a) center area of fiber precursor (b) edge area of fiber precursor (c) center area of fiber (d) edge area of fiber. All the fiber precursor and fiber were prepared from 50/50 PCL/OBC blend.

The cross-sectional morphologies of the fiber precursor and the fiber (both with PCL etched away) were also examined. Figure 6-3(a) and (b) are the SEM images of the fiber precursor's cross-section respectively in the center area and in the edge area. Some holes are observed in the center but they are not as many in the edge area. Similar trend can be seen in the SEM images of the fiber cross section – the center area (Figure 6-3 (c)) shows large holes while the edge area (Figure 6-3 (d)) has more concentrated solid phases. Since the holes correspond to the etched PCL phase, these results indicate that the phase structure in the fiber cross-section is not uniform. This is anticipated in a typical fiber cross-sectional morphology since the flow field varied in the radial direction during fiber formation.

6.3.2 Rheological Properties

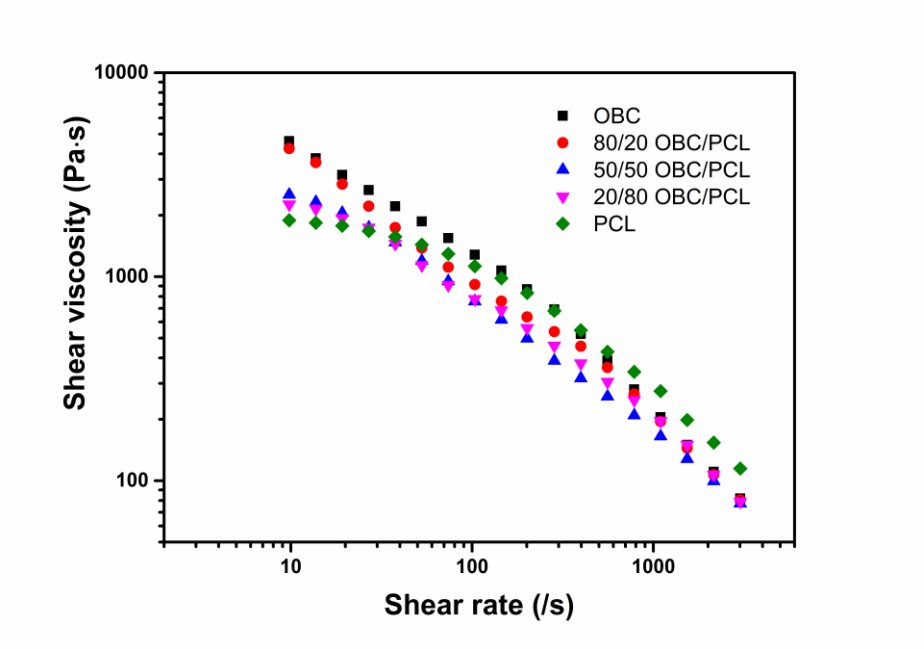

Figure 6-4 Shear viscosity of the component polymers and the blends.

Capillary rheometer was used to measure the shear viscosity-shear rate relations of pure PCL, pure OBC and the three PCL/OBC blends across a shear range of 10 - 3000 s^{-1} at 150 ^{o}C. The results shown in Figure 6-4 indicate that the PCL/OBC blend has a similar shear thinning behavior with the pure polymers. In certain shear rates, the blends have a slightly lower viscosity than pure polymers. This phenomenon also occurs in other polymer blends system. For example, Han and Yu [84] reported a reduced viscosity of the blend in the PP/PS blend system. They thought that this phenomenon might be caused by the easier slippage of the matrix phase along the interface of the immiscible polymer blends.

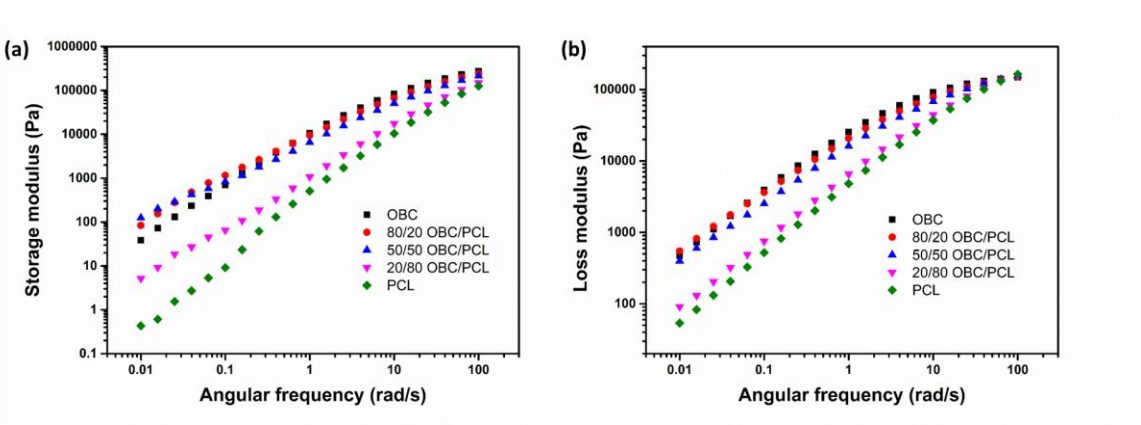

Figure 6-5 Storage modulus and (b) Loss modulus as a function of frequency for the three blends and the component polymers.

We used a rotational rheometer to measure the dynamic moduli for the two components and the blends at 150 ^{o}C, as shown in Figure 6-5. The measurements were performed at a strain amplitude of 1%, which is in the linear regime of 0.1 % - 10 % indicated by the strain sweep. Since OBC is more elastomeric, it has a higher storage modulus than PCL. The small shoulder in the low-frequency regimes of the storage modulus of 80/20 OBC/PCL indicates a droplet-matrix structure, attributed to shape relaxation of the droplets driven by interfacial tension [71]. This result is consistent with the SEM image of the 80/20 OBC/PCL, which shows the existence of the matrix-droplet structure. We cannot obtain the SEM image of the 20/80 OBC/PCL because of the disintegration of the OBC phase after dissolution of PCL. However, based on its storage modulus which also has a shoulder in the low-frequency regimes, we can infer it holds a matrix-droplet structure too. Different from the storage modulus behaviors of 80/20 OBC/PCL and 20/80 OBC/PCL, the 50/50 OBC/PCL displays a power law behavior at low frequencies, attributed to the network relaxation of double interpenetrating phases. This is corresponding with the SEM observation that the 50/50 OBC/PCL holds a co-continuous structure. The loss modulus does not show any terminal response.

6.3.3 Shrinkage Ratio

Table 6-1. The shrinkage ratios of 50/50 OBC/PCL fiber at 100 ºC and 120 ºC.

	Shrinkage ratio at 100 ºC (Times)	Shrinkage ratio at 120 ºC (Times)
50/50 OBC/PCL fiber	3.75	7.50
50/50 OBC/PCL fiber with hot drawing	4.69	8.33

Although we prepared three blends: 80/20 OBC/PCL, 50/50 OBC/PCL and 20/80 OBC/PCL, only the fiber prepared from the 50/50 OBC/PCL have the supercontraction ability while the fiber from the other two blends cannot shrink much. This might be related with their different microstructure: 50/50 OBC/PCL has a co-continuous structure while the other two hold a matrix-droplet structure. When the fiber precursor made from 50/50 OBC/PCL is drawn into a fiber, both the PCL phase and the OBC phase will be drawn and oriented. The PCL phase will crystallize and the oriented structure of the PCL molecules will be locked. Because of the co-continuous structure in which the two phases are interconnected, when the PCL phase crystallize, it will lock the orientation of the OBC phase too. Later when the fiber encounters heat, the PCL phase melts and the locked OBC phase and PCL phase will be unlocked and disorient, which, macroscopically, is the phenomenon of supercontraction. For the fiber made from 80/20 OBC/PCL, although the PCL phase will crystallize and orient too during the fiber preparation, it cannot lock the

orientation of the OBC phase since the PCL phase exists as droplets and is not continuous. Therefore, the orientation of OBC phase in the obtained fiber is not high enough and the fiber does not have the property of supercontraction. For the fiber made from 20/80 OBC/PCL, the PCL phase is continuous and the OBC phase exists as droplets. Since a large portion of the high shrinkage comes from the elastomeric OBC phase, the amount of OBC phase in the 20/80 OBC/PCL fiber is not high enough to provide large shrinkage.

We measured the shrinkage ratio of the fiber prepared from the 50/50 OBC/PCL under two temperatures (100 ^{o}C and 120 ^{o}C). Besides, we measured the shrinkage ratio of the fiber that is hot drawn at 50 ^{o}C. The hot draw ratio is about 1.3 times. The shrinkage ratios are given in Table 6-1. All the fibers have a higher shrinkage ratio at 120 ^{o}C than they are at 100 ^{o}C. Hot drawing at 50 ^{o}C will increase the shrinkage ratio, which indicates that the orientation degree of the PCL phase and the OBC phase is positively correlated with the shrinkage ratio.

6.3.4 Shrinking Stress

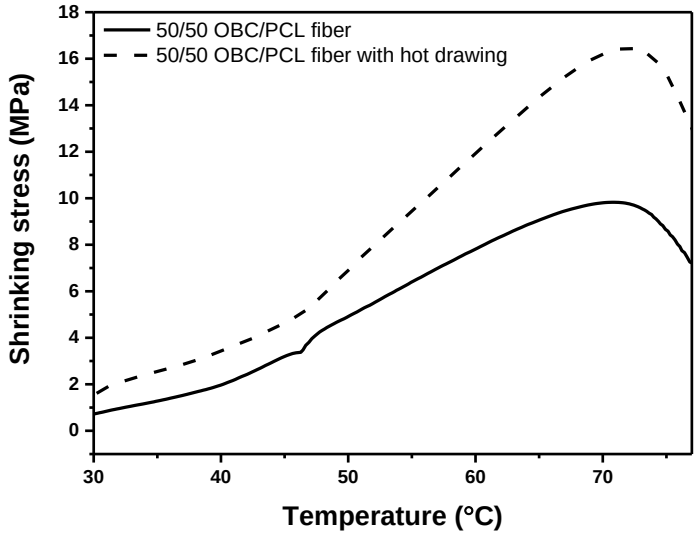

Figure 6-6 The shrinking stress of 50/50 OBC/PCL fiber and 50/50 OBC/PCL fiber with hot drawing.

The shrinking stress of the two types of fibers are measured and shown in Figure 6-6. Basically, the contraction stress - temperature curve has two stages: first, the stress increases when the temperature increases and reaches a maximum stress; second, the stress decreases with the increase of temperature. These trends may be explained using basic polymer science. In the first stage, it is anticipated that more and more PCL chains are softened with increasing temperature and more and more OBC chains are unlocked. The softened PCL chains and unlocked OBC chains contributes to the increasing contraction stress. In the second stage, the stress decreases as the PCL phase at this temperature range is melted and the chains are mostly disoriented. The 50/50 PCL/OBC blend fiber has a maximum stress of around 9.8 MPa. In contrast, the 50/50 PCL/OBC blend fiber with hot drawing has the highest maximum stress of 16.4 MPa. The different contraction stress of these two types of fibers indicates the influence of the orientation degree on the contraction stress.

6.3.5 Thermal Properties

Table 6-2. Thermal properties of component polymers, blends, fiber, fiber with hot drawing.

	OBC	50/50 OBC/PCL blend	50/50 OBC/PCL fiber	50/50 OBC/PCL fiber with hot drawing	PCL
T_m of PCL (°C)	/	56.7	60.6	61.5	55.2
Enthalpy of PCL (J/g)	/	62.6	79.5	94.9	60.0
Crystallinity of PCL (%)	/	46.4%	58.9%	70.3%	44.4%
Tm of OBC (°C)	120.9	120.7	121.4	121.6	/
Enthalpy of OBC (J/g)	23.4	35.7	37.8	35.2	/
Crystallinity of OBC (%)	8.1%	12.3%	13.0%	12.1%	/

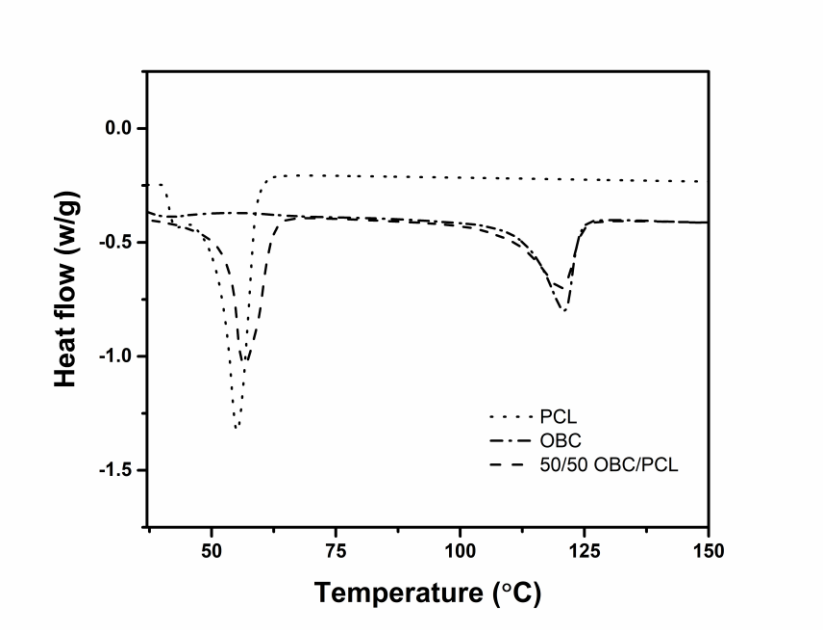

Figure 6-7 DSC thermograms of component polymers and the 50/50 OBC/PCL blend.

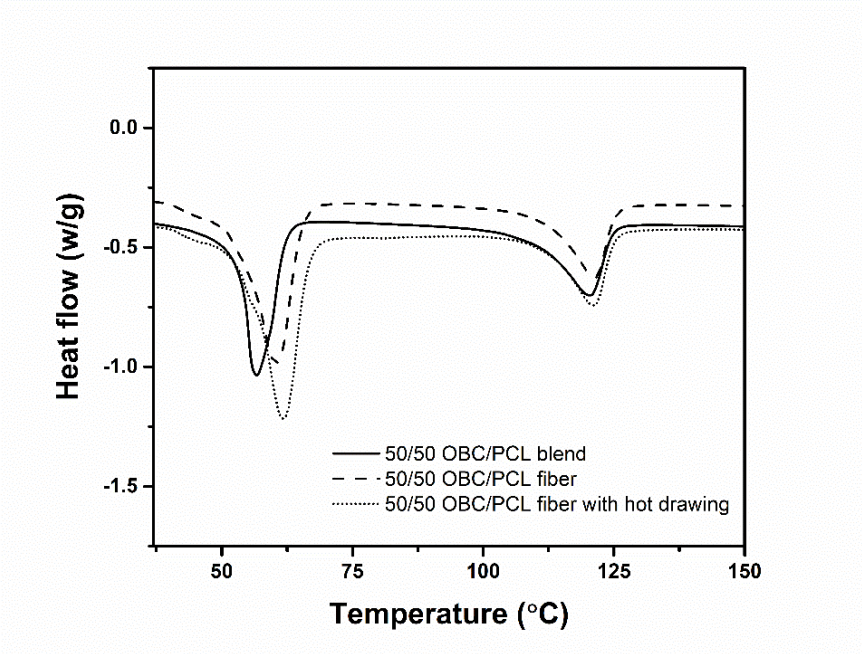

Figure 6-8 DSC thermograms of the 50/50 OBC/PCL blend, fiber prepared from 50/50 OBC/PCL and fiber prepared from 50/50 OBC/PCL with hot drawing.

The thermal properties of the PCL, OBC, 50/50 OBC/PCL blend and two types of fibers (50/50 OBC/PCL blend fiber and 50/50 OBC/PCL blend fiber with hot drawing) were measured with DSC and the results are shown in Figure 6-7, Figure 6-8, and Table 6-2. Research has shown that PCL's crystallinity may be reduced when it is blended with polyurethane [105]. But from Figure 6-8 and Table 6-2, we can see that the crystallinity of PCL phase in 50/50 OBC/PCL blend is similar with that in pure PCL, which means blending with OBC does not hinder its crystallization. Whether PCL's crystallinity is influenced or not might be related with the miscibility of the blended polymers. The thermal properties of 50/50 OBC/PCL blend and 50/50 OBC/PCL blend fiber indicate that the drawing process in the preparation of fiber increases both the melting temperature and crystallinity of PCL phase. The melting temperature and crystallinity of OBC phase are also increased, but not as much as those of the PCL phase. This is because the drawing process took place at room temperature, which is close to the crystalline temperature of PCL but far from the crystalline temperature of OBC. The hot drawing process increases the crystallinity and the melting temperature of the PCL phase, which might be why hot drawing increased the fiber's mechanical properties and the shrinking ability.

6.3.6 Mechanical Properties

Table 6-3. Mechanical properties of the fibers prepared from component polymers and three polymer blends.

	OBC fiber	80/20 OBC/PCL fiber	50/50 OBC/PCL fiber	20/80 OBC/PCL fiber	PCL fiber
Tensile strength (MPa)	23.4	36.9	82.6	110.2	132.4
Young's modulus (MPa)	2.8	7.6	190.0	466.9	584.0
Tensile strain (%)	868	748	73.4	37.2	34.3

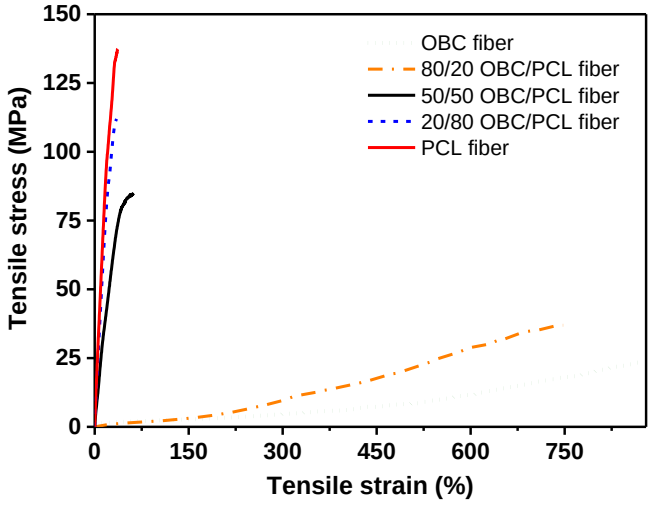

Figure 6-9 Representative stress-strain curves of the fibers prepared from component polymers and three polymer blends.

Table 6-4. Mechanical properties of the fiber prepared from 50/50 OBC/PCL and the fiber prepared from 50/50 OBC/PCL with hot drawing.

	50/50 OBC/PCL fiber	50/50 OBC/PCL fiber with hot drawing
Tensile strength (MPa)	82.6	130.1
Young's modulus (MPa)	190.0	792.1
Tensile strain (%)	73.4	28.9

The tensile properties of fibers from pure polymers and three polymer blends (Table 6-3, with their representative stress-strain curves given in Figure 6-9) and the 50/50 PCL/OBC blend fiber with hot drawing (Table 6-4) are measured. From Figure 6-9, we can see that pure OBC fiber and 80/20 OBC/PCL fiber both have a large tensile strain because OBC is an elastomer. Pure PCL fiber have a small tensile strain and high tensile strength and Young's modulus. 50/50 OBC/PCL fiber has a tensile strength around 80 MPa, which is relatively strong. From Table 6-4, we can see that hot drawing the fiber increases the tensile strength and Young's modulus, which may be related with the higher orientation degree and higher crystallinity. Therefore, hot drawing may be a potential method for further improving the fiber's mechanical properties, and this makes it suitable for scenarios where higher mechanical properties are needed.

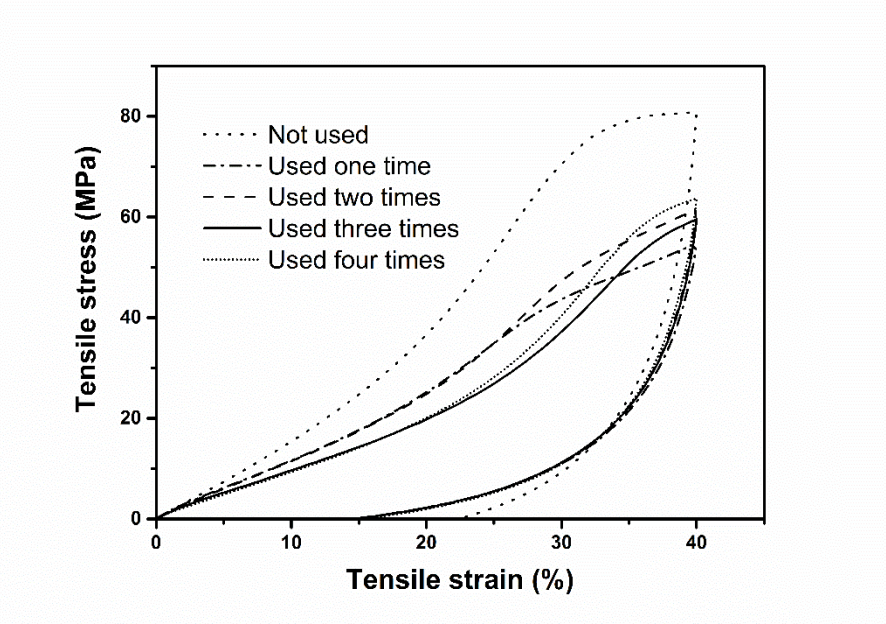

Figure 6-10. Representative stress-strain curves of 50/50 PCL/OBC fiber that are used repeatedly for multiple times under cyclic loading–unloading tensile tests.

To investigate the repeatability of the supercontraction property, we performed loading and unloading tensile tests for 50/50 PCL/OBC fiber that are used for different number of cycles. After a fiber was prepared, we performed a loading and unloading tensile test and the result is labeled as "not used" since the fiber did not shrink even once. Then we heat shrank the fiber and drew it and then performed the same experiment, which is labeled as "used one time" as the fiber has undergone the shrinking and drawing cycle once. Then we heat shrank the fiber and drew it again and performed the same experiment, which is labeled as "used two times". The same procedure was repeated for two more times and that's how we got the data of "used three times" and "used four times". The results are shown in Figure 6-10. We can see that the hysteresis of the "not used" fiber and the rest fibers are different – the former has a higher tensile stress and a larger hysteresis. The difference might be partly attributed to the Mullins effect [106] and partly due to the polymer molecules' rearrangement, such as weak point broken and phase separation. When

the fiber undergoes at least one shrinking – drawing cycle, the measured amounts of hysteresis are similar, which indicates our fiber might be used for multiple times. Since the drawing step in the fiber preparation process is conducted at room temperature (hot drawing at 50 ^{o}C is not a must-to-do although it's helpful for improving the mechanical properties and the shrinking stress), our fiber can be easily reset for another use after one use/heat shrinking, which brings great convenience for repeated use of the fiber.

6.4 Conclusions

A simple method of melt blending, extrusion and drawing is used to prepare PCL/OBC supercontraction fiber. Combining the morphological properties of the blends and the shrinking ability of the corresponding fibers, we infer that the blend needs to be co-continuous to make the obtained fiber have a supercontraction ability. Besides, the amount of the elastomeric phase needs to be high enough to generate enough contraction forces and make the fiber shrink. If scenarios where higher mechanical strength are encountered, the fiber can be hot drawn to enhance the mechanical properties. Hot drawing also helps increase the shrinking stress and the shrinkage ratio, possibly due to the higher molecular orientation induced by the hot drawing. Since the drawing step is conducted in room temperature, one can easily reset the used fiber by drawing the fiber by hand for another use. Results from cyclic loading and unloading tests indicates the fiber has the potential of being used repeatedly for multiple times. With its high shrinkage ratio, this supercontracion fiber can be potentially used in emerging areas of textiles such as intelligent biomedical textiles or smart garments.

7. CONCLUSIONS AND RECOMMENDATIONS

7.1 Conclusions

Briefly summarizing, this thesis work establishes a logical connection between the interface dynamics and process design, which allows us to develop processing methodologies suitable for enhancing mechanical properties of immiscible polymer blends and at the same time, developing new applications for polymer blends. Basically, this processing methodology employs a nearly co-continuous morphology for enhancing properties while reducing processing cost. In addition, for the purpose of generating a large molecular orientation while mitigating the interfacial orientation, interface dynamics and rheological behaviors are used for guiding the process design and lead to a process of melt spinning with almost no jet stretch and separate hot drawing at a relatively low temperature.

Specifically, in the part of interface dynamics, a method different from the interface tensor theory or area tensor theory is used for investigating the interface dynamics. Chapter 2 deals with the case of affine deformation. Three equivalent solutions to the Cauchy stress tensor are derived based on the Finger strain tensor. This approach is less complex than the Doi-Ohta method because it only involves elementary algebraic and matrix operations and avoids the complex calculation introduced by the involvement of a fourth-order tensor. The use of the Finger strain tensor also provides a convenient way of representing the complex interface using the ellipsoidal surface approximation, which can help resolve the tensor derivative $\partial g/\partial \mathbf{B}$ into elementary functions for some complex interfaces. Two case studies

are used to validate the effectiveness of the Finger strain tensor approach combined with the approximations to the ellipsoidal surface area. Interfacial orientation is an important parameter during the processing of immiscible polymer blends. Therefore, a variable ϕ was defined to represent the interfacial orientation degree based on the Finger strain tensor and the evolution of interfacial orientation degree in affine deformation was calculated and plotted in uniaxial elongation deformation field, biaxial elongation deformation field, planar elongation deformation field and simple shear deformation field.

Chapter 2 assumed affine deformation and neglected the relaxation effects, making it unsuitable for the viscoelastic polymer blends which have relaxation effects. Therefore, the evolution of interfacial orientation degree with the consideration of relaxation effects is studied and introduced in Chapter 3. A memorized strain $\mathbf{B}_e$ is used to represent the actual deformation while a dissipated strain $\mathbf{B}_d$ is used to represent the lost strain during the relaxation. The evolution equation for $\mathbf{B}_e$ can be obtained by an energy balance approach. Interfacial orientation degree now depends on $\mathbf{B}_e$ instead of $\mathbf{B}$. Therefore, the time evolution of interfacial orientation degree with time can be obtained via $\mathbf{B}_e$, which is shown in different deformation fields including uniaxial elongation deformation field, biaxial elongation deformation field, planar elongation deformation field and simple shear deformation field. In addition, we obtained the evolution of interfacial orientation degree as a function of reduced time for the relaxation of polymer blends subject to a step strain. The influence of temperature on relaxation rate was investigated and the calculation results of relaxation of polymer blends at different temperatures were consistent with the experimental results of stress relaxation at the same series.

Chapter 4 introduces how the interface dynamics and rheological studies are used for guiding the process design of preparing usable products from immiscible polymer blends. The general guidelines of the designed process include the use of a nearly co-continuous morphology, the increase of molecular orientation and the mitigation of interfacial effects. Interface dynamics indicates that the interfacial orientation generated in elongational flow fields is much larger than that in shear flow fields. Rheological studies show that at high temperatures the relaxation time of the interface is considerably larger than that of polymer molecules. Combining these two findings together inspires us to avoid elongational flow at the liquid state of polymer blends. Accordingly, we propose the following processing strategy for promoting molecular orientation in melt spinning of immiscible blends with at least one continuous phase: applying no jet stretch during melt extrusion and subsequently hot drawing the blend fiber at a relatively low temperature.

To demonstrate the effectiveness of this strategy for enhancing mechanical properties of immiscible blends product, a case study using PP/PS blends was performed and described in Chapter 4, where the blends form a nearly co-continuous phase structure with PP as the continuous phase. In this case study, the PP/PS blends were spun with the proposed processing methodology: almost no jet stretch was applied and after solidification the fiber underwent a hot drawing step at a temperature close to the glass transition temperature of PS. The hot drawing temperature should be within the optimum range in order to achieve proper drawing without damaging the fiber. This process sequence imparts a large degree of molecular orientation to the PP phase and produces a strong fiber. For comparison, traditional melt spinning which involves a large jet stretch was used for preparing fiber and the strength of the obtained fiber was less than 50 MPa. In contrast, the

fiber prepared with our processing methodology is as strong as more than 300 MPa, indicating the effectiveness of the proposed strategy in enhancing the mechanical properties of the immiscible blends.

This processing methodology may also be used for achieving additional properties by using suitable combinations of different materials and open up new blend products innovation. As a case study, Chapter 5 introduces the supercontraction fiber with shrinkage ratio as high as 8 times. The fiber was prepared from simple polymer blending and melt spinning. Specifically, polycaprolactone (PCL) and ethylene-octene block copolymer (OBC) blends are prepared and then made into fibers with a two-step process of melt extrusion and drawing. The SEM images of the blends indicate two types of structure: co-continuous structure and matrix-droplet structure. Fiber made from co-continuous blend has a supercontraction ability while fiber from the blends with matrix-droplet structure does not. A cyclic tensile testing experiment shows that the supercontraction fiber may be used repeatedly for multiple times.

In summary, under the guidance of interface dynamics and rheological study, a processing methodology is proposed for preparing usable products from immiscible polymer blends. The recycling of mixed plastics also deals with immiscible polymers with complex interfaces. Therefore, if combined with additional efforts, the proposed methodology may be used in plastics recycling with multiple polymers.

7.2 Recommendations

As shown above, the proposed methodology is able to effectively enhance the mechanical properties of products made of immiscible polymer blends. To extend its

applicability, further research should be performed to better understand the process dynamics and address potential limitations of this methodology. As such, recommendations for future studies are presented here for the purpose of further defining the processing scope and understanding the fundamental knowledge.

The processing methodology uses a nearly co-continuous morphology for achieving usable properties and reducing processing cost. However, an appropriate range of co-continuity has not been quantitatively specified and validated. In the future studies, this issue is worthy to be investigated both theoretically and experimentally. A convenient method for characterizing the co-continuity should be developed and used to experimentally validate the appropriate range of co-continuity.

In the study of interface dynamics, the evolution of interfacial orientation in different deformation fields was investigated. At present, however, there is limited research on quantitative characterization of the interfacial orientation of polymer blends during processing. Investigation of potential characterization tools and methods for quantifying the interfacial orientation is highly suggested, which can help verify the prediction accuracy of theoretical modeling and further understand the fundamental issues of interface dynamics.

The theoretical study assumes that the components in the blends have roughly equal viscosity. Besides, it only considers continuous relaxation processes. However, these assumptions may not always be valid in practical applications. For example, the co-continuity may not be high enough or the deformation may be considerably large; in either case the discrete relaxation processes such as droplet breakup and coalescence cannot be

neglected. Such behavior can eventually result in decreased predication accuracy in constitutive modeling of interfacial orientation, and therefore, corresponding adjustments in the modeling process will be required to reflect the considerations of additional effects in these cases.

The fiber preparation in the proposed methodology includes three separate steps - melt blending, melt extrusion and hot drawing, which limits the efficiency of this process. Further study about how to make the process continuous will be of great benefit for the successful scale-up of this process. A potential method is suggested below in Figure 7-1. After the fiber is extruded, quench air can be applied to make sure its temperature is cooled to below the hot drawing temperature. Some parameters need to be optimized for continuous and efficient production. For example, some additives may be added to act as surfactant so that the extrusion speed can be increased. The diameter of the extruded fiber may be decreased by using a die with reduced size so that a larger drawing speed in the hot drawing step can be used.

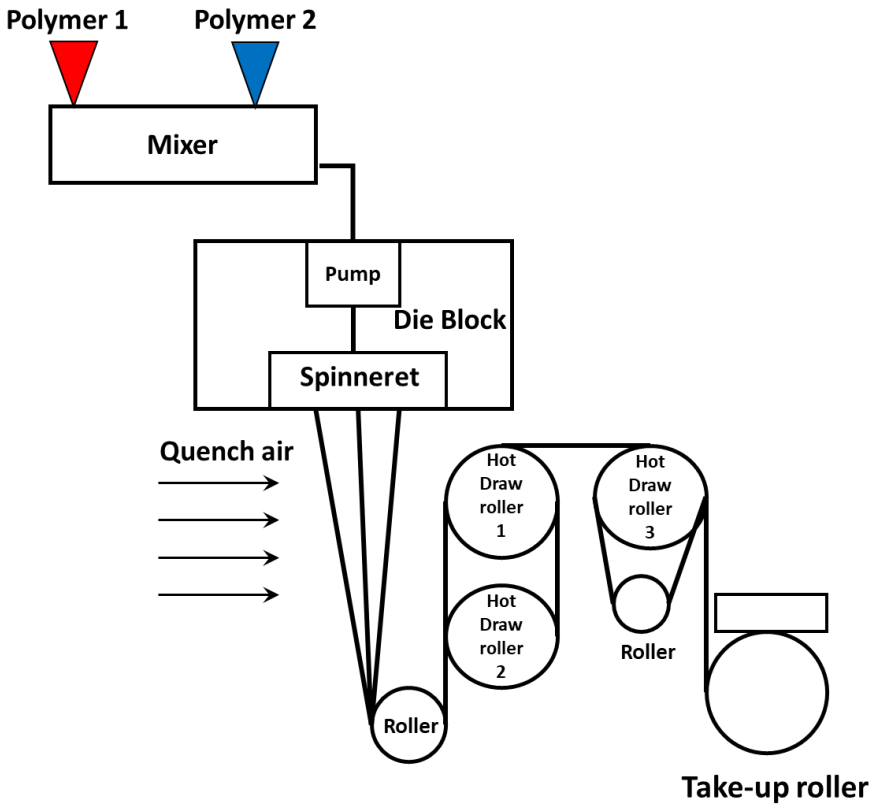

Figure 7-1 Proposed potential set-up for continuous production of blend fiber

The two case studies used a model system with two types of polymers, in which the complex interfaces are constituted between two polymers. However, in the real cases of waste plastic recycling, usually more than two types of polymers are mixed together. Therefore, a model system which consists of three or more types of immiscible polymers can be studied to investigate the processing conditions for preparing strong products from such a system. Besides, currently only polymers without a significant hydrogen bonding are involved. To further define the processing scope, case studies can be performed with polymers which have strong hydrogen bonding interactions.

REFERENCES

1. *Global plastic production from 1950 to 2016 (in million metric tons)**. Available from: https://www.statista.com/statistics/282732/global-production-of-plastics-since-1950/.
2. Utracki, L.A. and C.A. Wilkie, *Polymer blends handbook*. Vol. 1. 2002: Springer.
3. Smyers, W.H. and D.W. Young, *Styrene copolymer mixtures*. 1952, Google Patents.
4. *Engineering Resins, Polymer Alloys and Blends: Global Markets*. Available from: https://www.bccresearch.com/market-research/plastics/engineering-resins-polymer-markets-report-pls020e.html.
5. Paul, D.R., *Polymer blends*. Vol. 1. 1978, New York: Academic Press.
6. Fainleib, A. and O. Grigoryeva, *Recent Developments in Polymer Recycling.* Transworld Research Network: Kerala, India, 2011.
7. Liu, X. and H. Bertilsson, *Recycling of ABS and ABS/PC blends.* Journal of applied polymer science, 1999. **74**(3): p. 510-515.
8. Santana, R.M.C. and S. Manrich, *Morphology and mechanical properties of polypropylene/high-impact polystyrene blends from postconsumer plastic waste.* Journal of applied polymer science, 2003. **88**(13): p. 2861-2867.
9. Halimatudahliana, A., H. Ismail, and M. Nasir, *Morphological studies of uncompatibilized and compatibilized polystyrene/polypropylene blend.* Polymer Testing, 2002. **21**(3): p. 263-267.

10. Equiza, N., W. Yave, R. Quijada, and M. Yazdani-Pedram, *Use of SEBS/EPR and SBR/EPR as binary compatibilizers for PE/PP/PS/HIPS blends: A work oriented to the recycling of thermoplastic wastes.* Macromolecular Materials and Engineering, 2007. **292**(9): p. 1001-1011.

11. Wang, Y., Y. Zhang, M. Polk, S. Kumar, and J. Muzzy, *Recycling of carpet and textile fibers.* Plastics and the Environment, 2003: p. 697-725.

12. Elmaghor, F., L. Zhang, and H. Li, *Recycling of high density polyethylene/poly (vinyl chloride)/polystyrene ternary mixture with the aid of high energy radiation and compatibilizers.* Journal of applied polymer science, 2003. **88**(12): p. 2756-2762.

13. Suarez, J.C.M., E.B. Mano, and C.M.C. Bonelli, *Effects of gamma-irradiation on mechanical characteristics of recycled polyethylene blends.* Polymer Engineering & Science, 1999. **39**(8): p. 1398-1403.

14. Gupta, S., M. Pallavi, A. Som, R. Krishnamurthy, and A.K. Bhowmick, *Anomalous mechanical behavior upon recycling of poly (phenylene-ether)-based thermoplastic elastomer.* Polymer Engineering & Science, 2008. **48**(3): p. 496-504.

15. Bertin, S. and J.-J. Robin, *Study and characterization of virgin and recycled LDPE/PP blends.* European Polymer Journal, 2002. **38**(11): p. 2255-2264.

16. Bartlett, D., J. Barlow, and D. Paul, *Mechanical properties of blends containing HDPE and PP.* Journal of Applied Polymer Science, 1982. **27**(7): p. 2351-2360.

17. White, J.L. and M. Cakmak, *Orientation development and crystallization in melt spinning of fibers.* Advances in polymer technology, 1986. **6**(3): p. 295-337.

18. Medeiros, E.S., G.M. Glenn, A.P. Klamczynski, W.J. Orts, and L.H. Mattoso, *Solution blow spinning: A new method to produce micro-and nanofibers from polymer solutions.* Journal of applied polymer science, 2009. **113**(4): p. 2322-2330.

19. Doshi, J. and D.H. Reneker, *Electrospinning process and applications of electrospun fibers.* Journal of electrostatics, 1995. **35**(2-3): p. 151-160.

20. *Introduction and melt spinning line*. Available from: https://nptel.ac.in/courses/116102010/6.

21. Li, Y., C. Zou, J. Shao, X. Zhang, and Y.n. Li, *Preparation of SiO 2/PS superhydrophobic fibers with bionic controllable micro–nano structure via centrifugal spinning.* RSC Advances, 2017. **7**(18): p. 11041-11048.

22. Taylor, G.I., *The viscosity of a fluid containing small drops of another fluid.* Proceedings of the Royal Society of London. Series A, Containing Papers of a Mathematical and Physical Character, 1932. **138**(834): p. 41-48.

23. Taylor, G.I., *The formation of emulsions in definable fields of flow.* Proceedings of the Royal Society of London. Series A, containing papers of a mathematical and physical character, 1934. **146**(858): p. 501-523.

24. Einstein, A., *A new determination of molecular dimensions.* Ann. Phys., 1906. **19**: p. 289-306.

25. Cox, R., *The deformation of a drop in a general time-dependent fluid flow.* Journal of fluid mechanics, 1969. **37**(3): p. 601-623.

26. Chaffey, C.E. and H. Brenner, *A second-order theory for shear deformation of drops.* Journal of Colloid and Interface Science, 1967. **24**(2): p. 258-269.

27. Frankel, N. and A. Acrivos, *The constitutive equation for a dilute emulsion.* Journal of Fluid Mechanics, 1970. **44**(1): p. 65-78.

28. Tavgac, T., *Drop deformation and breakup in simple shear fields*. 1973.

29. Fröhlich, A. and R. Sack, *Theory of the rheological properties of dispersions.* Proceedings of the Royal Society of London. Series A. Mathematical and Physical Sciences, 1946. **185**(1003): p. 415-430.

30. Wu, S., *Formation of dispersed phase in incompatible polymer blends: Interfacial and rheological effects.* Polymer Engineering & Science, 1987. **27**(5): p. 335-343.

31. Favis, B.D., *The effect of processing parameters on the morphology of an immiscible binary blend.* Journal of applied polymer science, 1990. **39**(2): p. 285-300.

32. Choi, S.J. and W. Schowalter, *Rheological properties of nondilute suspensions of deformable particles.* The Physics of Fluids, 1975. **18**(4): p. 420-427.

33. Palierne, J., *Linear rheology of viscoelastic emulsions with interfacial tension.* Rheologica acta, 1990. **29**(3): p. 204-214.

34. Karam, H. and J. Bellinger, *Deformation and breakup of liquid droplets in a simple shear field.* Industrial & Engineering Chemistry Fundamentals, 1968. **7**(4): p. 576-581.

35. Torza, S., R. Cox, and S. Mason, *Particle motions in sheared suspensions XXVII. Transient and steady deformation and burst of liquid drops.* Journal of colloid and interface science, 1972. **38**(2): p. 395-411.

36. Huneault, M., Z. Shi, and L. Utracki, *Development of polymer blend morphology during compounding in a twin-screw extruder. Part IV: A new computational model with coalescence.* Polymer Engineering & Science, 1995. **35**(1): p. 115-127.

37. Bruijn, d., R. A., *Deformation and breakup of drops in simple shear flows*. 1989.

38. Flumerfelt, R.W., *Drop Breakup in Simple Shear Fields of Viscoleastic Fluids.* Industrial & Engineering Chemistry Fundamentals, 1972. **11**(3): p. 312-318.

39. Macosko, C., P. Guegan, A.K. Khandpur, A. Nakayama, P. Marechal, and T. Inoue, *Compatibilizers for melt blending: Premade block copolymers.* Macromolecules, 1996. **29**(17): p. 5590-5598.

40. Doi, M. and T. Ohta, *Dynamics and rheology of complex interfaces. I.* The Journal of chemical physics, 1991. **95**(2): p. 1242-1248.

41. Takahashi, Y., N. Kurashima, I. Noda, and M. Doi, *Experimental tests of the scaling relation for textured materials in mixtures of two immiscible fluids.* Journal of Rheology, 1994. **38**(3): p. 699-712.

42. Takahashi, Y., S. Kitade, N. Kurashima, and I. Noda, *Viscoelastic properties of immiscible polymer blends under steady and transient shear flows.* Polymer journal, 1994. **26**(11): p. 1206.

43. Vinckier, I., P. Moldenaers, and J. Mewis, *Relationship between rheology and morphology of model blends in steady shear flow.* Journal of Rheology, 1996. **40**(4): p. 613-631.

44. Lee, H.M. and O.O. Park, *Rheology and dynamics of immiscible polymer blends.* Journal of Rheology, 1994. **38**(5): p. 1405-1425.

45. El Afif, A., D. De Kee, R. Cortez, and D. Gaver III, *Dynamics of complex interfaces. I. Rheology, morphology, and diffusion.* The Journal of chemical physics, 2003. **118**(22): p. 10227-10243.

46. Gu, J.F. and M. Grmela, *Flow properties of immiscible blends: Doi-Ohta model with active advection.* Physical Review E, 2008. **78**(5): p. 056302.

47. Wetzel, E.D. and C.L. Tucker III, *Area tensors for modeling microstructure during laminar liquid-liquid mixing.* International journal of multiphase flow, 1999. **25**(1): p. 35-61.

48. Chella, R. and J. Ottino, *Stretching in some classes of fluid motions and asymptotic mixing efficiencies as a measure of flow classification.* Archive for rational mechanics and analysis, 1985. **90**(1): p. 15-42.

49. David, C., M. Trojan, R. Jacobs, and M. Piens, *Morphology of polyethylene blends: 1. From spheres to fibrils and extended co-continuous phases in blends of polyethylene with styrene-isoprene-styrene triblock copolymers.* Polymer, 1991. **32**(3): p. 510-515.

50. Tsebrenko, M., N. Rezanova, and G. Vinogradov, *Rheology of molten blends of polyoxymethylene and ethylene-vinyl acetate copolymer and the microstructure of extrudates as a function of their melt viscosities.* Polymer Engineering & Science, 1980. **20**(15): p. 1023-1028.

51. Varma, D. and V. Dhar, *Studies of nylon 6/PET polymer blends: structure and some physical properties.* Journal of applied polymer science, 1987. **33**(4): p. 1103-1124.

52. Zuo, F., D.H. Tan, Z. Wang, S. Jeung, C.W. Macosko, and F.S. Bates, *Nanofibers from melt blown fiber-in-fiber polymer blends.* ACS Macro Letters, 2013. **2**(4): p. 301-305.

53. Paul, D.R., *Polymer blends*. Vol. 1. 2012: Elsevier.

54. Paul, D.R. and J. Barlow, *Polymer blends.* Journal of Macromolecular Science—Reviews in Macromolecular Chemistry, 1980. **18**(1): p. 109-168.

55. Miles, I.S. and A. Zurek, *Preparation, structure, and properties of two-phase co-continuous polymer blends.* Polymer Engineering & Science, 1988. **28**(12): p. 796-805.

56. Tang, C., P. Chen, and H. Liu, *Cocontinuous cellulose acetate/polyurethane composite nanofiber fabricated through electrospinning.* Polymer Engineering & Science, 2008. **48**(7): p. 1296-1303.

57. Liang, B.R., J.L. White, J.E. Spruiell, and B.C. Goswami, *Polypropylene/nylon 6 blends: Phase distribution morphology, rheological measurements, and structure development in melt spinning.* Journal of Applied Polymer Science, 1983. **28**(6): p. 2011-2032.

58. Min, K., J.L. White, and J.F. Fellers, *High density polyethylene/polystyrene blends: Phase distribution morphology, rheological measurements, extrusion, and melt spinning behavior.* Journal of applied polymer science, 1984. **29**(6): p. 2117-2142.

59. Mukhopadhyay, S., *Bi-component and bi-constituent spinning of synthetic polymer fibres*, in *Advances in Filament Yarn Spinning of Textiles and Polymers*. 2014, Elsevier. p. 113-127.

60. Paul, D. and J. Barlow, *Polymer blends.* Journal of Macromolecular Science—Reviews in Macromolecular Chemistry, 1980. **18**(1): p. 109-168.

61. Yao, D., *Constitutive modeling of complex interfaces based on a differential interfacial energy function.* Rheologica acta, 2011. **50**(3): p. 199-206.

62. Yao, D., *A visco-hyperelastic formulation for the rheology of immiscible blends.* Journal of Rheology, 2012. **56**(4): p. 767-795.

63. Xu, D., J. Cui, R. Bansal, X. Hao, J. Liu, W. Chen, and B.S. Peterson, *The ellipsoidal area ratio: an alternative anisotropy index for diffusion tensor imaging.* Magnetic resonance imaging, 2009. **27**(3): p. 311-323.

64. Zhou, Y., F. Yu, H. Deng, Y. Huang, G. Li, and Q. Fu, *Morphology Evolution of Polymer Blends under Intense Shear During High Speed Thin-Wall Injection Molding.* The Journal of Physical Chemistry B, 2017. **121**(25): p. 6257-6270.

65. Wu, S., *Polymer interface and adhesion*. 1982, New York: Marcel Dekker.

66. Palmer, G. and N.R. Demarquette, *Evaluation of imbedded fiber retraction phenomenological models for determining interfacial tension between molten polymers.* Polymer, 2005. **46**(19): p. 8169-8177.

67. Raghu, P., C. Nere, and R. Jagtap, *Effect of styrene–isoprene–styrene, styrene–butadiene–styrene, and styrene–butadiene–rubber on the mechanical, thermal, rheological, and morphological properties of polypropylene/polystyrene blends.* Journal of applied polymer science, 2003. **88**(2): p. 266-277.

68. Martin, G., C. Barrès, P. Sonntag, N. Garois, and P. Cassagnau, *Co-continuous morphology and stress relaxation behaviour of unfilled and silica filled PP/EPDM blends.* Materials Chemistry and Physics, 2009. **113**(2-3): p. 889-898.

69. Tschoegl, N., *A general method for the determination of approximations to the spectral distributions from the transient response functions.* Rheologica Acta, 1971. **10**(4): p. 595-600.

70. Gramespacher, H. and J. Meissner, *Interfacial tension between polymer melts measured by shear oscillations of their blends.* Journal of Rheology, 1998. **36**(6): p. 1127.

71. Li, R., W. Yu, and C. Zhou, *Rheological characterization of droplet-matrix versus co-continuous morphology.* Journal of Macromolecular Science, Part B, 2006. **45**(5): p. 889-898.

72. Lv, Y., Y. Huang, M. Kong, H. Zhu, Q. Yang, and G. Li, *Stress relaxation behavior of co-continuous PS/PMMA blends after step shear strain.* Rheologica Acta, 2013. **52**(4): p. 355-367.

73. Thompson, R.C., C.J. Moore, F.S. Vom Saal, and S.H. Swan, *Plastics, the environment and human health: current consensus and future trends.* Philosophical Transactions of the Royal Society B: Biological Sciences, 2009. **364**(1526): p. 2153-2166.

74. Fainleib, A., *Recent Developments in Polymer Recycling*. 2011, Kerala: Transworld Research Network.

75. Brody, H., *Orientation suppression in fibers spun from polymer melt blends.* Journal of applied polymer science, 1986. **31**(8): p. 2753-2768.

76. Zander, N.E., D. Sweetser, D.P. Cole, and M. Gillan, *Formation of nanofibers from pure and mixed waste streams using electrospinning.* Industrial & Engineering Chemistry Research, 2015. **54**(37): p. 9057-9063.

77. Xing, Q., M. Zhu, Y. Wang, Y. Chen, Y. Zhang, J. Pionteck, and H. Adler, *In situ gradient nano-scale fibril formation during polypropylene (PP)/polystyrene (PS) composite fine fiber processing.* Polymer, 2005. **46**(14): p. 5406-5416.

78. Zander, N.E., M. Gillan, and D. Sweetser, *Composite fibers from recycled plastics using melt centrifugal spinning.* Materials, 2017. **10**(9): p. 1044.

79. Ito, M., K. Takahashi, and T. Kanamoto, *Preparation of high-modulus and high-strength fibers from high molecualar weight poly (ethylene terephthalate).* Journal of Applied Polymer Science, 1990. **40**(7-8): p. 1257-1263.

80. Schaller, R., K. Feldman, P. Smith, and T.A. Tervoort, *High-performance polyethylene fibers "al dente": improved gel-spinning of ultrahigh molecular weight polyethylene using vegetable oils.* Macromolecules, 2015. **48**(24): p. 8877-8884.

81. Song, C. and A. Isayev, *LCP droplet deformation in fiber spinning of self-reinforced composites.* Polymer, 2001. **42**(6): p. 2611-2619.

82. Erkoc, I.G., T. Guven, F. Yildirim, M. Sözer, and F. Güner, *Effect of Screw Speed, Drawing Ratio and PET Concentration on the Properties of PET/PP Blends.* Acta Physica Polonica, A., 2018. **134**(1).

83. Amash, A. and P. Zugenmaier, *Morphology and properties of isotropic and oriented samples of cellulose fibre–polypropylene composites.* Polymer, 2000. **41**(4): p. 1589-1596.

84. Han, C.D. and T.C. Yu, *Rheological properties of molten polymers. II. Two-phase systems.* Journal of Applied Polymer Science, 1971. **15**(5): p. 1163-1180.

85. Lacroix, C., M. Bousmina, P. Carreau, B. Favis, and A. Michel, *Properties of PETG/EVA blends: 1. Viscoelastic, morphological and interfacial properties.* Polymer, 1996. **37**(14): p. 2939-2947.

86. Vinckier, I. and H.M. Laun, *Manifestation of phase separation processes in oscillatory shear: droplet-matrix systems versus co-continuous morphologies.* Rheologica acta, 1999. **38**(4): p. 274-286.

87. Weis, C., J. Leukel, K. Borkenstein, D. Maier, W. Gronski, C. Friedrich, and J. Honerkamp, *Morphological and rheological detection of the phase inversion of PMMA/PS polymer blends.* Polymer Bulletin, 1998. **40**(2-3): p. 235-241.

88. López-Barrón, C.R. and C.W. Macosko, *A new model for the coarsening of cocontinuous morphologies.* Soft Matter, 2010. **6**(12): p. 2637-2647.

89. George, H., A. Holt, and A. Buckley, *A study of structural development in the high speed spinning of poly (ethylene terephthalate).* Polymer Engineering & Science, 1983. **23**(2): p. 95-99.

90. Uehara, H., Y. Yamazaki, and T. Kanamoto, *Tensile properties of highly syndiotactic polypropylene.* Polymer, 1996. **37**(1): p. 57-64.

91. Liu, Y., Z. Shao, and F. Vollrath, *Relationships between supercontraction and mechanical properties of spider silk.* Nature Materials, 2005. **4**(12): p. 901.

92. Whewell, C. and H. Woods, *The supercontraction of animal fibres.* Soc. Dyers Colonrists, Sym. on Fibrous Proteins, 1946: p. 50-57.

93. Singha, K., S. Maity, and M. Singha, *Spinning and applications of spider silk.* Frontiers in Science, 2012. **2**(5): p. 92-100.

94. Pérez-Rigueiro, J., M. Elices, and G. Guinea, *Controlled supercontraction tailors the tensile behaviour of spider silk.* Polymer, 2003. **44**(13): p. 3733-3736.

95. Mishra, J.K., I. Kim, and C.S. Ha, *Heat Shrinkable Behavior and Mechanical Response of a Low-Density Polyethylene/Millable Polyurethane/Organoclay Ternary Nanocomposite.* Macromolecular rapid communications, 2004. **25**(21): p. 1851-1855.

96. Kumar, S. and M. Pandya, *Thermally recoverable crosslinked polyethylene.* Journal of applied polymer science, 1997. **64**(5): p. 823-829.

97. Khonakdar, H.A., J. Morshedian, H. Eslami, and F. Shokrollahi, *Study of heat shrinkability of crosslinked low-density polyethylene/poly (ethylene vinyl acetate) blends.* Journal of applied polymer science, 2004. **91**(3): p. 1389-1395.

98. Stanko., W.S., *U. S. Patent*. 1989.

99. Zhang, Q., D. Yan, K. Zhang, and G. Hu, *Pattern transformation of heat-shrinkable polymer by three-dimensional (3D) printing technique.* Scientific reports, 2015. **5**: p. 8936.

100. Charuchinda, A., R. Molloy, J. Siripitayananon, N. Molloy, and M. Sriyai, *Factors influencing the small-scale melt spinning of poly (ε-caprolactone) monofilament fibres.* Polymer international, 2003. **52**(7): p. 1175-1181.

101. Kim, J.W. and J.S. Lee, *Effect of Heat Drawing Process on Mechanical Properties of Dry-Jet Wet Spun Fiber of Linear Low Density Polyethylene/Carbon Nanotube Composites.* International Journal of Polymer Science, 2017. **2017**.

102. Wang, Y., W. Zhao, X. Wang, and D. Wu, *Preparation, mechanical properties and microstructure of polyoxymethylene fiber through melt spinning and hot drawing*

by using injection-molding grade resins. Fibers and Polymers, 2016. **17**(9): p. 1464-1474.

103. Rui, J., M. Dadsetan, M.B. Runge, R.J. Spinner, M.J. Yaszemski, A.J. Windebank, and H. Wang, *Controlled release of vascular endothelial growth factor using poly-lactic-co-glycolic acid microspheres: in vitro characterization and application in polycaprolactone fumarate nerve conduits.* Acta biomaterialia, 2012. **8**(2): p. 511-518.

104. Park, H.E., J.M. Dealy, G.R. Marchand, J. Wang, S. Li, and R.A. Register, *Rheology and structure of molten, olefin multiblock copolymers.* Macromolecules, 2010. **43**(16): p. 6789-6799.

105. Ajili, S.H. and N.G. Ebrahimi, *Miscibility of TPU (PCL diol)/PCL blend and its effect on PCL crystallinity.* Macromolecular symposia, 2007. **249**(1): p. 623-627.

106. Diani, J., B. Fayolle, and P. Gilormini, *A review on the Mullins effect.* European Polymer Journal, 2009. **45**(3): p. 601-612.